University of Padova

Department of Physics "Galileo Galilei"

Master Thesis in Physics of Data

Bayesian Inference for Molecular Quantum Logic Spectroscopy

Supervisors

Prof. Ilaria Siloi

University of Padova

Master Candidate

Andrea Turci

Student ID

2106724

Co-supervisors

Prof. Philipp Schindler

University of Innsbruck

Dott. Brandon Furey

University of Innsbruck

Academic Year

2025-2026

Abstract

Gli ioni molecolari si stanno affermando come piattaforme potenti per la spettroscopia di precisione, l'elaborazione quantistica dell'informazione e la ricerca di fisica oltre il Modello Standard. Tuttavia, la loro ricca struttura interna — che comprende gradi di libertà elettronici, vibrazionali, rotazionali, fini e iperfini — insieme all'assenza di transizioni ottiche chiuse, rende estremamente difficili la lettura diretta dello stato e il controllo quantistico coerente, in particolare per le specie poliatomiche. In questa tesi, sviluppiamo un framework teorico e computazionale completo per la spettroscopia e il controllo quantistico degli ioni molecolari $^{40}CaH^+$ e $^{40}CaOH^+$ co-intrappolati con uno ione logico $^{40}Ca^+$ in una trappola lineare di Paul, utilizzando la spettroscopia a logica quantistica (QLS) come strumento primario di lettura.

Sviluppiamo un simulatore fisico probabilistico classico che modella in modo efficiente gli spettri Raman iperfini di entrambi gli ioni molecolari in condizioni sperimentali realistiche. Il simulatore, validato rispetto allo spettro misurato sperimentalmente di $^{40}CaH^+$, riproduce quantitativamente la struttura iperfina a due picchi e le transizioni firma J-dipendenti. Il $^{40}CaOH^+$ presenta uno spettro qualitativamente diverso, in cui i picchi iperfini si trovano vicino alla frequenza zero e sono in gran parte oscurati dalla forza dipolare ottica (ODF) generata da componenti di polarizzazione spurie nei fasci Raman. Per aggirare questo problema, introduciamo una strategia di chiusura dei loop che sopprime l'eccitazione motionale indotta dall'ODF scegliendo una durata del impulso dipendente dalla detuning, rendendo i picchi iperfini del $^{40}CaOH^+$ sperimentalmente accessibili.

Per consentire l'identificazione dello stato attraverso le transizioni firma J-dipendenti, progettiamo un protocollo di preparazione dello stato in due fasi. La prima fase consiste in uno schema di pompaggio ottico a sei stadi, che include una nuova configurazione a tre rami che sfrutta le transizioni Raman a $\Delta m = -2$ per rimuovere la popolazione intrappolata negli stati centrali — una limitazione fondamentale dell'approccio standard a due rami. La seconda fase impiega impulsi Raman di passaggio adiabatico rapido sul sideband per trasferire la popolazione residua allo stato bersaglio in modo robusto su più manifold simultaneamente. Gli spettri pompati risultanti mostrano picchi di transizione firma chiaramente risolti con un rapporto segnale-rumore significativamente migliorato per entrambe le molecole.

Infine, sviluppiamo un framework di stima bayesiana dello stato per inferire il manifold rotazionale dello ione molecolare da sequenze di misure QLS binarie. Il framework incorpora le imperfezioni sperimentali tramite correzioni dei tassi di falso positivo e negativo, sequenze di misura strutturate a blocchi e marginalizzazione della verosimiglianza rispetto alle incertezze di frequenza Raman. Per $^{40}CaH^+$, si raggiungono tassi di successo dell'88–90%. Per $^{40}CaOH^+$, dove la sovrapposizione delle transizioni firma e la

sensibilità ai parametri rendono l'inferenza considerevolmente più difficile, il tasso di successo migliora dal 12.5% senza strategie di mitigazione al 45–58% con l'insieme completo di strategie; tra le esecuzioni convergenti, il tasso di successo raggiunge l'84–90%. Questo framework costituisce una solida base computazionale per la realizzazione sperimentale, e la sua architettura generale — applicabile a qualsiasi ione molecolare lineare con spin nucleare $1/2$ — apre la strada alla manipolazione coerente degli stati e al controllo quantistico di un'ampia classe di ioni molecolari poliatomici.

Abstract

Molecular ions are emerging as powerful platforms for precision spectroscopy, quantum information processing, and the search for physics beyond the Standard Model. However, their rich internal structure — comprising electronic, vibrational, rotational, fine, and hyperfine, degrees of freedom — together with the absence of closed optical cycling transitions, makes direct state readout and coherent quantum control extremely challenging, particularly for polyatomic species. In this thesis, we develop a comprehensive theoretical and computational framework for the spectroscopy and quantum control of $^{40}CaH^+$ and $^{40}CaOH^+$ molecular ions co-trapped with a $^{40}Ca^+$ logic ion in a linear Paul trap, using quantum logic spectroscopy (QLS) as the primary readout tool. We develop a classical probabilistic physics simulator that efficiently models the hyperfine Raman spectra of both molecular ions under realistic experimental conditions. The simulator, validated against the experimentally measured spectrum of $^{40}CaH^+$, quantitatively reproduces the two-peak hyperfine structure and the J-dependent signature transitions. $^{40}CaOH^+$ exhibits a qualitatively different spectrum where the hyperfine peaks are located near zero frequency and largely obscured by the optical dipole force (ODF) arising from spurious polarization components in the Raman beams. To circumvent this problem, we introduce a loop closing strategy that suppresses ODF-induced motional excitation by choosing a detuning-dependent pulse duration, making the $^{40}CaOH^+$ hyperfine peaks experimentally accessible. To enable state identification through J-dependent signature transitions, we design a two-stage state preparation protocol. The first stage consists of a six-step optical pumping scheme, which includes a novel three-branch configuration exploiting $\Delta m = -2$ Raman transitions to remove population trapped in central dark states — a fundamental limitation of the standard two-branch approach. The second stage employs Raman-driven rapid adiabatic passage sideband pulses to transfer residual population to the target state robustly across multiple manifolds simultaneously. The resulting pumped spectra show clearly resolved signature transition peaks with significantly improved signal-to-noise ratio for both molecules.

Finally, we develop a Bayesian state estimation framework to infer the rotational manifold of the molecular ion from sequential binary QLS measurement outcomes. The framework incorporates experimental imperfections through false-rate corrections, block-structured measurement sequences, and likelihood marginalization over Raman frequency uncertainties. For $^{40}CaH^+$, success rates of 88–90% are achieved. For $^{40}CaOH^+$, where overlapping signature transitions and parameter sensitivity make the inference considerably harder, the success rate improves from 12.5% without mitigation strategies to 45–58% with the full set of strategies; among converging runs, the success rate reaches 84–90%. This framework constitutes a solid computational foundation for experimental realization, and its general architecture — applicable to any nuclear spin-1/2 linear

molecular ion — opens the door to coherent state manipulation and quantum control of a broad class of polyatomic molecular ions.

Contents

List of Figures

List of Tables

List of acronyms

QLS . . . . . Quantum logic spectroscopy

BSB . . . . . Blue sideband

RBS . . . . . Red sideband

ODF . . . . . Optical dipole force

RAP . . . . . Rapid adiabatic passage

CW . . . . . Continuous wave

BE . . . . . Bayesian estimator

BS . . . . . Bayesian simulator

LM . . . . . Leftmost (state)

PU . . . . . Penultimate upper (state)

PL . . . . . Penultimate lower (state)

FOM . . . . . Figure-of-merit

ST . . . . . Signature transition

1

Introduction

Precision spectroscopy of molecular ions represents one of the most powerful tools available for measuring fundamental constants with ever-increasing accuracy or searching for physics beyond the Standard Model. Beyond their utility in probing for eEDM or parity violation, molecular ions offer a compelling platform for quantum information processing and quantum simulation owing to their rich internal structure and long-lived quantum states. In this context, the ability to perform spectroscopy and exert coherent quantum control over trapped molecular ions is a central challenge and a key enabling step toward a wide range of quantum applications. Unlike atomic ions, molecular ions do not possess closed optical cycling transitions, which makes direct laser cooling and state-selective fluorescence detection essentially impossible. Their internal state structure is far richer - comprising electronic, vibrational, rotational, and hyperfine degrees of freedom - and population can rapidly distribute across a large number of nearly-degenerate states. This complexity, while potentially a resource, makes direct state readout and controlled manipulation extremely challenging, particularly for polyatomic species. For the molecules considered in this work, $^{40}CaH^+$ and $^{40}CaOH^+$, the situation is further complicated by the presence of numerous overlapping hyperfine transitions and, in the case of $^{40}CaOH^+$, by Hamiltonian parameters that have not yet been experimentally determined. Quantum logic spectroscopy (QLS), originally developed for the spectroscopy of atomic ions, provides an elegant solution to this readout problem by transferring information about the spectroscopy ion's internal state to a co-trapped logic ion, for which efficient detection is available. This technique, combined with sympathetic laser cooling through the shared motional mode, enables non-destructive interrogation of the molecular state and opens the door to sequential quantum control. In this thesis, we develop and apply a comprehensive framework for the spectroscopy and quantum control of $^{40}CaH^+$ and $^{40}CaOH^+$ molecular ions co-trapped with a $^{40}Ca^+$ logic ion in a linear Paul trap. A prerequisite for both high-fidelity spectroscopy and quantum control is the ability to prepare the molecular ion in a well-defined initial

state. At room temperature, the molecule is distributed across a thermal mixture of rotational states, each manifold further consists of a large number of Zeeman states. To concentrate this population and enable the identification of the rotational manifold through unique signature transitions, we design a two-stage state preparation protocol. In the first stage, optical pumping — including a novel three-branch scheme exploiting $\Delta m = -2$ Raman transitions to remove population trapped in central dark states — transfers the population of each manifold toward the anti-aligned states. In the second stage, Raman-driven rapid adiabatic passage (RAP) pulses complete the transfer to the target state robustly across multiple manifolds simultaneously. The resulting pumped spectrum, with its enhanced signal-to-noise ratio on the signature transitions, serves both as a direct observable to validate the state preparation and as the starting point for the Bayesian inference stage.

Once the molecule has been prepared, the central challenge becomes inferring in which rotational state it resides. This is the task of Bayesian state estimation: given a sequence of binary QLS measurement outcomes, each corresponding to the presence or absence of fluorescence on the logic ion, one can update a probability distribution over the molecular states using Bayes' theorem, incorporating prior knowledge from the state preparation stage. This approach is particularly powerful for $^{40}CaOH^+$, where the overlapping signature transition frequencies and the sensitivity to experimental imperfections make direct state identification unreliable. The Bayesian framework naturally handles false positive and negative rates, Raman difference frequency miscalibration, and shot-to-shot fluctuations through likelihood marginalization and block-structured measurement sequences. Crucially, once the molecular state has been identified, the same QLS toolbox enables coherent manipulation and control of that state — opening the door to implementing quantum logic operations, preparing non-classical states of molecular rotation, and extending high-fidelity quantum control to a broad class of polyatomic molecular ions.

Thesis outline: Chapter 2 develops the theoretical foundations, from the laser-ion interaction and the molecular hyperfine Hamiltonian to the QLS protocol, the optical dipole force, and the RAP formalism. Chapter 3 applies this framework to simulate the hyperfine Raman spectra of $^{40}CaH^+$ and $^{40}CaOH^+$, validates the physics simulator against experimental $^{40}CaH^+$ data, and addresses the ODF problem for $^{40}CaOH^+$. Chapter 4 develops the state preparation protocol, combining optical pumping with Raman-driven RAP pulses. Chapter 5 presents the Bayesian state estimation framework and Monte Carlo simulation results for both molecular ions. Chapter 6 concludes with a summary and outlook.

2

Theory

This chapter introduces the theoretical foundations underlying the experimental and computational work presented in the subsequent chapters. The treatment proceeds from the simplest quantum system interacting with a laser field to the full description of a trapped molecular ion and the tools needed to manipulate and read out its internal state. We begin with the interaction between light and matter, reviewing the two-level system driven by a laser field and extending the framework to the laser-ion interaction in a harmonic trap, introducing the Lamb-Dicke regime and the carrier, red-sideband, and blue-sideband coupling cases. We then present the molecular Hamiltonian for a nuclear spin 1/2 linear molecular ion in its $^1\Sigma$ vibronic ground state in the presence of an external magnetic field, deriving the hyperfine structure and discussing the different magnetic field regimes and the rotational state thermal distribution. This is followed by the Raman coupling coefficients governing stimulated Raman transitions between molecular hyperfine states. Finally, we describe the quantum logic spectroscopy protocol, the optical dipole force arising from spurious polarization components in the Raman beams, and the rapid adiabatic passage technique used for robust state preparation.

2.1 Light-matter interaction

2.1.1 Two level system interacting with a laser beam

Let us consider a two-level quantum system, a qubit, composed of two eigenstates $\{|0\rangle, |1\rangle\}$ with energy eigenvalues $\{\epsilon_0 = \hbar\omega_0, \epsilon_1 = \hbar\omega_1\}$. The system is interacting with a laser field $\vec{E} = \hbar\Omega\cos(\omega_l t + \phi_l)$, where ω_l is the frequency of the laser, ϕ_l the phase, and Ω the Rabi frequency that represents the coupling strength between the qubit and the field. The Hamiltonian describing both the qubit system and the interaction with the laser is [1, 2]:

$$\begin{aligned}\hat{H} = \hat{H}_0 + \hat{V}(t) &= \sum_i \epsilon_i |i\rangle\langle i| + \sum_{ij} \Omega \left(|i\rangle\langle j| + |j\rangle\langle i|\right) \cos(\omega_l t + \phi_l) \\ &= \begin{pmatrix} \epsilon_0 & 0 \\ 0 & \epsilon_1 \end{pmatrix} + \begin{pmatrix} 0 & \Omega \\ \Omega & 0 \end{pmatrix} \cos(\omega_l t + \phi_l).\end{aligned} \tag{2.1}$$

Moving the reference frame to the interaction picture, we consider the following unitary operator [1]:

$$R(t) = e^{iKt}, \quad \text{where} \quad K = -\omega_l |0\rangle\langle 0|. \tag{2.2}$$

In order to change the reference frame we apply the following transformation of the Hamiltonian:

$$\hat{H}_{\text{int}} = R\hat{H}R^\dagger + i\dot{R}R^\dagger, \tag{2.3}$$

and using the rotating wave approximation that neglects terms oscillating with a frequency higher than the system timescale [2, 1], the interaction Hamiltonian becomes:

$$\hat{H}_{\text{int}} = \hbar \begin{pmatrix} \frac{\delta}{2} & \frac{\Omega}{2} e^{i\phi_l} \\ \frac{\Omega}{2} e^{-i\phi_l} & -\frac{\delta}{2} \end{pmatrix} = \frac{\hbar}{2}\Omega(\cos\phi_l \cdot \hat{\sigma}_x - \sin\phi_l \cdot \hat{\sigma}_y) + \frac{\hbar\delta}{2}\hat{\sigma}_z, \tag{2.4}$$

where $\hat{\sigma}_x, \hat{\sigma}_y$, and $\hat{\sigma}_z$ are the Pauli matrices, and $\delta = \omega_l - (\epsilon_1 - \epsilon_0)$ the frequency detuning between the qubit transition and the laser.
We write the interaction Hamiltonian as $\hat{H}_{\text{int}} = \frac{1}{2}\tilde{\Omega}(\hat{n} \cdot \vec{\sigma})$, where $\vec{\hat{\sigma}}$ is the Pauli matrices vector, $\hat{n}$ a unit vector, and $\tilde{\Omega} = \sqrt{\Omega^2 + \delta^2}$ the effective Rabi frequency. Thus, we can compute the time evolution operator as $U(t) = \exp\left(-i\hat{H}_{\text{int}}t\right)$, which describes the rotation of the qubit vector on the Bloch sphere [3] by an angle $\theta = \tilde{\Omega}t$ (the pulse area). At resonance ($\delta = 0$), it becomes:

$$U(\theta, \phi_l) = \begin{pmatrix} \cos\frac{\theta}{2} & -i\frac{\Omega}{\tilde{\Omega}} e^{i\phi_l} \sin\frac{\theta}{2} \\ i\frac{\Omega}{\tilde{\Omega}} e^{i\phi_l} \sin\frac{\theta}{2} & \cos\frac{\theta}{2} \end{pmatrix}. \tag{2.5}$$

This rotation describes a *Rabi oscillation.* Preparing the system in state $|0\rangle$, the probability to find the system in state $|1\rangle$ at time t is:

$$p_1 = |\langle 1 | U(\theta, \phi_l) | 0\rangle|^2 = \frac{\Omega^2}{\tilde{\Omega}^2} \sin\left(\tilde{\Omega}\frac{t}{2}\right). \tag{2.6}$$

The frequency of the Rabi flops is the effective Rabi frequency [3], and the amplitude of the oscillations depends on the ratio Ω/δ: with $\delta \gg \Omega$ the population transfer is negligible.

2.1.2 Laser-ion interaction

A single mode of the electromagnetic field is described by a harmonic oscillator Hamiltonian

$$\hat{H} = \frac{\hat{p}}{2m} + \frac{1}{2}m\omega^2\hat{x}^2 \tag{2.7}$$

where $\hat{x}$ and $\hat{p}$ are the position and momentum quantum operators. Defining the creation and annihilation operators as:

$$\hat{a}^\dagger = \sqrt{\frac{m\omega}{2\hbar}}\left(\hat{x} - \frac{i}{m\omega}\hat{p}\right) \quad \text{and} \quad \hat{a} = \sqrt{\frac{m\omega}{2\hbar}}\left(\hat{x} + \frac{i}{m\omega}\hat{p}\right), \tag{2.8}$$

the quantum Hamiltonian becomes [4]:

$$\hat{H} = \hbar\omega\left(\hat{a}^\dagger\hat{a} + \frac{1}{2}\right) = \hbar\omega\left(\hat{N} + \frac{1}{2}\right), \tag{2.9}$$

where $\hat{N}$ is the number operator which counts the number of photons in the field. The Hilbert space is a *Fock space*, which is made of vectors defined from the Fock vacuum state $|0\rangle$:

$$|n\rangle = \frac{(\hat{a}^\dagger)^n}{\sqrt{n!}}|0\rangle . \tag{2.10}$$

The quantization of the electromagnetic field shows that the Hamiltonian describes quanta, each having energy $\hbar\omega$.
Quantum states of the elctronmagnetic field which are eigenstates of hte annihilation operator are called *coherent states*, as their expectation values reduce to those expected for a classical field in the classical limit. Introducing the displacement operator

$$D(\alpha) = e^{\alpha\hat{a}^\dagger - \alpha^*\hat{a}}, \tag{2.11}$$

where α is the size of the displacement in the phase space, we define the *Glauber's coherent state* [5] as the vacuum Fock state displaced in the phase space, creating the following expansion of Fock states:

$$|\alpha\rangle = D(\alpha)|0\rangle = \sum_n e^{-|\alpha|^2/2}\frac{\alpha^n}{\sqrt{n!}}|n\rangle . \tag{2.12}$$

The probability of measuring n photons in a generic coherent state follows a Poisson's distribution with variance $\Delta n = |\alpha|$.
The coherent light field couples with the trapped two-level atom. The unperturbed

Hamiltonian reads as $\hat{H}_0 = \frac{\hbar\omega_0}{2}\hat{\sigma}_z + \hbar\omega_t(\hat{a}^\dagger\hat{a} + \frac{1}{2})$, where ω_0 is the 2-level transition frequency and ω_t the trap harmonic frequency [6]. The first term describes the internal electronic degrees of freedom, while the second one accounts for the motional degrees of freedom of the trapped ion, modeled as a harmonic oscillator. The unperturbed Hamiltonian does not include the electromagnetic field. The interaction between the trapped ion and the laser is described by the following Hamiltonian [6]:

$$\hat{H}_1 = \hbar\frac{\Omega}{2}(\hat{\sigma}_+ + \hat{\sigma}_-)\left(e^{i\eta(\hat{a}+\hat{a}^\dagger)}e^{-i(\omega_l t-\phi_l)} + e^{-i\eta(\hat{a}+\hat{a}^\dagger)}e^{i(\omega_l t-\phi_l)}\right), \tag{2.13}$$

where the electronic raising and lowering operators $\hat{\sigma}_\pm = (\hat{\sigma}_x \pm i\hat{\sigma}_y)/2$ have been used. Here, we define the Lamb-Dicke parameter [7] as the ratio between the atom ground-state wave-packet size and the laser wavelength

$$\eta = k\sqrt{\frac{\hbar}{2m\omega_t}}\cos\theta, \tag{2.14}$$

where k is the laser's wavenumber and θ its angle with respect to the ion's direction of motion. We apply the rotating wave approximation to the unperturbed Hamiltonian and the Lamb-Dicke approximation as long as $\eta^2(2\bar{n}+1) \ll 1$ [8], where $\bar{n}$ is the mean phonon number in the harmonic oscillator. This condition defines the Lamb-Dicke regime, in which the spatial extent of the ion's motional wave packet is much smaller than the laser wavelength. This implies that the recoil energy imparted by the absorption or emission of a photon is much smaller than the harmonic trap energy scale. The interaction Hamiltonian is thus described by:

$$\hat{H}_{\text{int}} = \hbar\frac{\Omega}{2}\left\{e^{-i(\Delta t-\phi_l)}\hat{\sigma}_+\left[\hat{\mathbb{I}} + i\eta\left(\hat{a}e^{-i\omega_t t} + \hat{a}^\dagger e^{i\omega_t t}\right)\right] + h.c.\right\}, \tag{2.15}$$

where $\Delta = \omega_l - \omega_0$ is the laser detuning.
A second rotating wave approximation can be applied to Eq. (2.15), assuming operation in the resolved sideband limit $\Omega \ll \omega_t$. Three coupling sub-regimes can be distinguished depending on the frequency to which the laser is tuned. They are represented in Figure 2.1 and analyzed separately [6]:

- Carrier resonance: $|\Delta| \ll \omega_t$, $\eta\Omega \ll \omega_t$
  The Hamiltonian is

  $$\hat{H}_{\text{car}} = \hbar\frac{\Omega_n}{2}\left(e^{-i\Delta t}e^{i\phi_l}\hat{\sigma}_+ + e^{i\Delta t}e^{-i\phi_l}\hat{\sigma}_-\right), \tag{2.16}$$

  where $\Omega_n = (1-\eta^2 n)\Omega$, and $e^{\pm i\Delta t} \simeq 1$.

The laser is resonant with the carrier transition $|0,n\rangle \leftrightarrow |1,n\rangle$ and sufficiently weak to be far-detuned from the others. Since $|\omega_t \pm \Delta| \simeq \omega_t \gg \eta\Omega$, there is no coupling between $|0,n\rangle$ and $|1,n\pm 1\rangle$.

- Red-sideband resonance: $|\Delta + \omega_t| \ll \omega_t, \Omega \ll \omega_t$
  In this case, the laser is resonant with $\omega_0 - \omega_t$. The carrier coupling is neglected, with the transition driving population transfer between $|0,n\rangle \leftrightarrow |1,n-1\rangle$. The Hamiltonian in this case is

$$\hat{H}_{\mathrm{RSB}} = i\hbar\eta\frac{\Omega}{2}\left(e^{-i\Delta_{\mathrm{RSB}}t}e^{i\phi_l}\hat{a}\hat{\sigma}_+ - e^{+i\Delta_{\mathrm{RSB}}t}e^{-i\phi_l}\hat{a}^\dagger\hat{\sigma}_-\right), \tag{2.17}$$

  where $e^{\pm i\Delta_{\mathrm{RSB}}t}$. $\Delta_{\mathrm{RSB}} = \Delta + \omega_t = \omega_l - \omega_0 + \omega_t$ is the laser detuning with respect to the red-sideband transition frequency.

- Blue-sideband resonance: $|\Delta - \omega_t| \ll \omega_t, \Omega \ll \omega_t$
  In this case the laser is resonant with $\omega_0 + \omega_t$, coupling the transition $|0,n\rangle \leftrightarrow |1,n+1\rangle$, and far-detuned from the others. The blue-sideband Hamiltonian reads as

$$\hat{H}_{\mathrm{BSB}} = i\hbar\eta\frac{\Omega}{2}\left(e^{-i\Delta_{\mathrm{BSB}}t}e^{i\phi_l}\hat{a}^\dagger\hat{\sigma}_+ - e^{+i\Delta_{\mathrm{BSB}}t}e^{-i\phi_l}\hat{a}\hat{\sigma}_-\right), \tag{2.18}$$

  where $e^{\pm i\Delta_{\mathrm{BSB}}t}$. $\Delta_{\mathrm{BSB}} = \Delta - \omega_t = \omega_l - \omega_0 - \omega_t$ is the laser detuning with respect to the blue-sideband transition frequency.

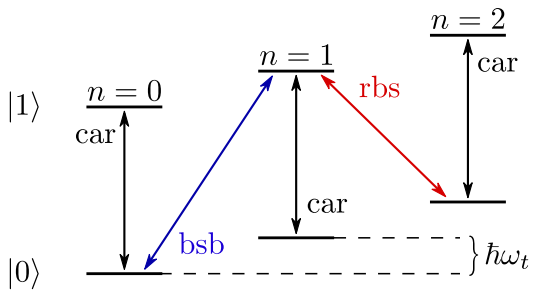

Figure 2.1: Energy-level diagram showing the internal states $|0\rangle$ and $|1\rangle$ coupled to the motional Fock states with carrier, blue-sideband, and red-sideband transitions.

Figure 2.2 illustrates the relation between the detuning of the motional-adding sideband transition, Δ_{BSB}, and the carrier detuning, Δ.

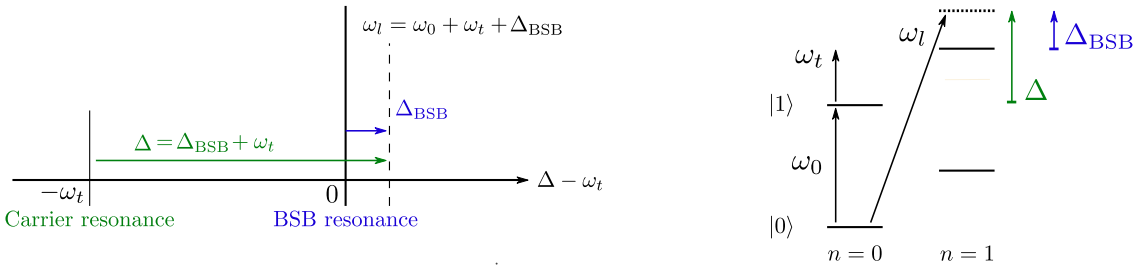

Figure 2.2: Frequency-domain (left) and level-diagram (right) representation of the BSB and carrier detunings with respect to the BSB frequency $\omega_0 + \omega_t$.

2.2 Molecular Hamiltonian

In the presence of an external magnetic field, the Hamiltonian associated to a nuclear spin 1/2 electronic $^1\Sigma$ $v = 0$ vibronic ground state linear molecular ion describes the rotation of the molecule and the hyperfine interaction [9]:

$$\hat{H} = \hat{H}_{\mathrm{rot}} + \hat{H}_{\mathrm{HF}} \tag{2.19}$$

where

$$\hat{H}_{\mathrm{rot}} = \frac{B_R \hat{J}^2}{\hbar^2} \tag{2.20}$$

represents the rotational Hamiltonian of rigid linear molecular rotors with rotational constant B_R. The eigenstates of this Hamiltonian can be identified with the rotational quantum number J, and the eigenvalues associated with these are:

$$E_J = B_R J(J+1). \tag{2.21}$$

Fixing the quantum number J, being a *good* quantum number, the hyperfine Hamiltonian is defined as follows:

$$\hat{H}_{\mathrm{HF}} = -\frac{g_J \mu_N}{\hbar} \hat{J} \cdot \vec{B} - \frac{g_I \mu_N}{\hbar} \hat{I} \cdot \vec{B} - \frac{2\pi c_{IJ}}{\hbar} \hat{I} \cdot \hat{J}, \tag{2.22}$$

where g_J and g_I are the gyromagnetic factors for rotation and nuclear spin of the proton respectively, μ_N the nuclear magneton, c_{IJ} the rotation-nuclear spin coupling parameter, $\vec{B}$ is the external magnetic field, and $\hat{I}$, $\hat{J}$ are the nuclear spin and rotational angular momentum operators, respectively.

In this context, relativistic corrections and contributions from the shielding tensor at excited vibrational states are neglected, as only the ground vibrational state is considered.

The hyperfine Hamiltonian describes the coupling between the magnetic field and the magnetic moments, as well as the coupling between the rotational magnetic moment and the nuclear magnetic moment. It produces the splitting of the Zeeman states, lifting their degeneracy.
In order to compute the Zeeman eigenstates and their corresponding eigenenergies, diagonalization of the Hamiltonian in Eq. (2.22) is required. The analytical derivations and related considerations are reported in Appendix A.
The eigenstates $|J, m, \xi\rangle$ of the molecular ion are defined by the following *good* set of quantum numbers [9]:

- $J \in \mathbb{Z}^{0+}$: the rotational angular momentum,
- $\xi \in \{+, -\}$: the nuclear spin characteristic, introduced to distinguish between the two eigenstates of the block Hamiltonian with different sign in the superposition (see Appendix A),
- m_F: the projection of the total angular momentum $\vec{F} = \vec{I} + \vec{J}$. If $\xi = +$, then $m_F \in [-J + 1/2, J + 1/2]$; if $\xi = -$, then $m_F \in [-J - 1/2, J - 1/2]$.

The quantum number I is also a good quantum number since it commutes with the Hamiltonian, but since $I = 1/2$ always, it is redundant.
As derived in Appendix A [9], the eigenvalues for the non-stretched states (when $|m_F| < J + 1/2$) are:

$$E_{J,m_F,\pm} = \frac{hc_{IJ}}{4} - g_J \mu_N B m_F \mp X_{J,m_F} \tag{2.23}$$

and the non-stretched eigenstates are hybridized product states of rotational and nuclear spin states:

$$
\begin{aligned}
|J, m_F, +\rangle = & \underbrace{\sqrt{\frac{X_{J,m_F} + Y_{J,m_F}}{2X_{J,m_F}}}}_{c^{\uparrow}_{J,m_F,+}} \left|J, m_F - \frac{1}{2}\right\rangle \left|\frac{1}{2}, \frac{1}{2}\right\rangle \\
& + \underbrace{\sqrt{\frac{X_{J,m_F} - Y_{J,m_F}}{2X_{J,m_F}}}}_{c^{\downarrow}_{J,m_F,+}} \left|J, m_F + \frac{1}{2}\right\rangle \left|\frac{1}{2}, -\frac{1}{2}\right\rangle \\
|J, m_F, -\rangle = & \underbrace{\sqrt{\frac{X_{J,m_F} - Y_{J,m_F}}{2X_{J,m_F}}}}_{c^{\uparrow}_{J,m_F,-}} \left|J, m_F - \frac{1}{2}\right\rangle \left|\frac{1}{2}, \frac{1}{2}\right\rangle \\
& - \underbrace{\sqrt{\frac{X_{J,m_F} + Y_{J,m_F}}{2X_{J,m_F}}}}_{c^{\downarrow}_{J,m_F,-}} \left|J, m_F + \frac{1}{2}\right\rangle \left|\frac{1}{2}, -\frac{1}{2}\right\rangle,
\end{aligned}
\tag{2.24}
$$

where the explicit expressions for X_{J,m_F} and Y_{J,m_F} are obtained in Eq. (A.4) of Appendix A. We call $c^{\uparrow}_{J,m_F,\pm}$ the amplitude of the $m_I = 1/2$ component in the eigenstates, and $c^{\downarrow}_{J,m_F,\pm}$ the amplitude of the $m_I = -1/2$ component. Note that the non-stretched states can possess both the spin-up and spin-down coefficients. To quantify the degree of the spin-up term in the eigenstates, we make use of the following quantity:

$$
S = {c^{\uparrow}_{J,m_F,\pm}}^2 - {c^{\downarrow}_{J,m_F,\pm}}^2. \tag{2.25}
$$

The eigenvalues for the stretched states (when $m_F = \pm J \pm 1/2$) are:

$$
E_{J,\pm(J+\frac{1}{2}),\pm} = \mp \left(g_J J + \frac{g_I}{2}\right) \mu_N B - \frac{hc_{IJ}}{2} J, \tag{2.26}
$$

and the relative eigenstates are fully-aligned product states of rotational and nuclear spin states:

$$
\left|J, \pm\left(J + \frac{1}{2}\right), \pm\right\rangle = |J, \pm J\rangle \left|\frac{1}{2}, \pm\frac{1}{2}\right\rangle. \tag{2.27}
$$

The levels are organized in manifolds labeled by the quantum number J, each comprised of $2(2J + 1)$ states. Figure 2.3 shows the structure of the hyperfine Hamiltonian for the first two manifolds. In each rotational manifold J, the levels are organized into 2 hyperfine manifolds, one for each value of ξ: the levels in the $\xi = +$ submanifold (lower sub-manifold) have $m_F \in [-J + 1/2, J + 1/2]$ and lower energy values

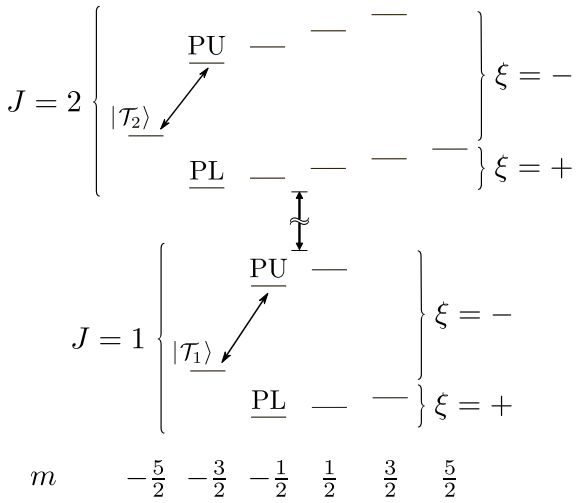

Figure 2.3: Schematic of the hyperfine level structure for the first two manifolds. The target ($|\mathscr{T}_J\rangle$), penultimate upper (PU), and penultimate lower (PL) states are depicted, as well as the signature transitions.

with respect to the levels of the $\xi = -$ sub-manifold (upper sub-manifold), which have $m_F \in [-J - 1/2, J - 1/2]$.
For the purpose of this thesis, we define the state $|J, -J - 1/2, -\rangle$ as the *target state*, or *leftmost state* (LM), and we will use the abbreviation $|\mathscr{T}_J\rangle$. This state will be used for the state preparation of the molecule. The $|J, -J + 1/2, -\rangle$ state of the upper sub-manifold to the right of the LM state is called *penultimate upper state* (PU), and the transition between the LM and PU states is called *signature transition* (ST).
The state $|J, -J + 1/2, +\rangle$ of the $\xi = +$ sub-manifold is called *penultimate lower* state (PL).

2.2.1 Magnetic field interaction regimes

We can identify different interaction regimes, depending on the magnetic field strength B. The first is the Zeeman regime, when $B \to 0$. The couplings of the external magnetic field with the angular momenta are considered as a perturbation with respect to the spin-rotation interaction.

Expanding X_{J,m_F} and Y_{J,m_F}, the non-stretched eigenstates and eigenvalues become:

$$\begin{aligned}
|J,m_F,+\rangle =& \sqrt{\frac{J+m_F+1/2}{2J+1}}\left|J,m_F-\frac{1}{2}\right\rangle\left|\frac{1}{2},\frac{1}{2}\right\rangle \\
&+\sqrt{\frac{J-m_F+1/2}{2J+1}}\left|J,m_F+\frac{1}{2}\right\rangle\left|\frac{1}{2},-\frac{1}{2}\right\rangle \\
|J,m_F,-\rangle =& \sqrt{\frac{J-m_F+1/2}{2J+1}}\left|J,m_F-\frac{1}{2}\right\rangle\left|\frac{1}{2},\frac{1}{2}\right\rangle \\
&-\sqrt{\frac{J+m_F+1/2}{2J+1}}\left|J,m_F+\frac{1}{2}\right\rangle\left|\frac{1}{2},-\frac{1}{2}\right\rangle \\
E_{J,m_F,\pm} =& \frac{hc_{IJ}}{4} \mp \Delta_J^{(I,J)} - g_{J,\pm}^{(Z)}\mu_N B m_F,
\end{aligned} \tag{2.28}$$

where $\Delta_J^{(I,J)} = \frac{1}{2}hc_{IJ}\left(J+\frac{1}{2}\right)$ is the splitting of the rotational manifold into two hyperfine manifolds due to nuclear spin-rotation coupling and $g_{J,\pm}^{(Z)} = \left[g_J \mp \frac{(g_J-g_I)}{2J+1}\right]$ is the effective g-factor that generates the Zeeman splitting which depends on J and ξ. In the limiting case of $B = 0$, the energies are not m_F-dependent. The stretched eigenstates and eigenvalues remains unchanged from the general case, and thus follow Eqs. (2.26) and (2.27).

The second regime we consider is called Paschen-Back regime, where $c_{IJ} \to 0$. In contrast to the Zeeman regime, the nuclear spin-rotation interaction is negligible with respect to the magnetic field couplings. Expanding c_{IJ} to the first-order, one obtains the following non-stretched eigenstates and eigenvalues:

$$\begin{aligned}
|J,m_F,+\rangle =& \left|J,m_F-\frac{1}{2}\right\rangle\left|\frac{1}{2},\frac{1}{2}\right\rangle \\
|J,m_F,-\rangle =& \left|J,m_F+\frac{1}{2}\right\rangle\left|\frac{1}{2},-\frac{1}{2}\right\rangle \\
E_{J,m_F,\pm} =& \frac{hc_{IJ}}{4} - g_J\mu_N B m_F \mp \frac{1}{2}\left[hc_{IJ}m_F - (g_J-g_I)\mu_N B\right]
\end{aligned} \tag{2.29}$$

which leads to a splitting of the Zeeman states into two substates. In the complete absence of nuclear spin-rotation coupling ($c_{IJ} = 0$), these collapse into a pair of degenerate states for each m_F split by the difference in g_J and g_I.

In most cases the molecular ions reside in neither the Zeeman nor the Paschen-Back regime, but rather in an intermediate regime where all the terms in the hyperfine Hamil-

tonian of Eq. (2.22) contribute.

In order to quantify the magnetic field regime, we can also define a figure of merit (FOM) based on the degree of hybridization of the countersymmetrically incremented projections of nuclear spin and rotation. We define the hybridization to be [10]:

$$\mathscr{H}(J, m_F, B) = 1 - \left| \frac{Y_{J,m_F}}{X_{J,m_F}} \right|, \tag{2.30}$$

which ranges between 0 and 1 in absolute value. We can establish the FOM for the B-field eliminating the m_F-dependence from the hybridization definition: setting $m_F = 0$ (the median) and making the values follow the direction of B by taking $1 - \mathscr{H}$:

$$\mathscr{F}(J, B) = 1 - \mathscr{H}(J, 0, m_F). \tag{2.31}$$

The FOM $\mathscr{F}(J, B)$ tends towards 0 in the Zeeman limit, towards 1 in the Paschen–Back limit, while acquiring intermediate values in the crossover regime.

2.2.2 Rotational state thermal distribution

We consider an experiment performed at room temperature $T \simeq 300\,\mathrm{K}$. The rotational population is in equilibrium with a thermal bath at blackbody temperature T given by

$$P_J = \frac{e^{-\frac{B_R J(J+1)}{k_B T}}}{\sum_{J=0}^{\infty} e^{-\frac{B_R J(J+1)}{k_B T}}}, \tag{2.32}$$

where k_B is the Boltzmann constant.
The part of the spontaneous decay rate that does *not* depend on m or Δm, for decays from rotational level J to $J-1$, is

$$\gamma_J^{SD} = \frac{8 d^2 B_R^3 J^3}{3\pi\epsilon_0 \hbar^4 c^3}, \tag{2.33}$$

where all quantities are expressed in SI units. In this expression, d is the molecular electric transition dipole moment, ϵ_0 is the vacuum permittivity, and c is the speed of light.
Blackbody radiation can also induce decay. The $m, \Delta m$-independent contribution of BBR-induced decay from J to $J-1$ is

$$\gamma_J^{BBR} = \frac{\gamma_J^{SD}}{e^{\frac{2B_R J}{k_B T}} - 1}. \tag{2.34}$$

The total decay rate out of the J manifold takes into account the spontaneous decay to $J-1$, the stimulated emission from J to $J-1$ caused by BBR, and the absorption by BBR from J to $J+1$.
This combined rate is given by [11]

$$\Gamma_J = \frac{1}{2J+1}\Big[J\left(\gamma_J^{SD} + \gamma_J^{BBR}\right) + (J+1)\gamma_{J+1}^{BBR}\Big]. \tag{2.35}$$

The associated lifetime of the rotational level J is simply the inverse of this rate:

$$\tau_J = \Gamma_J^{-1}. \tag{2.36}$$

2.3 Raman interaction and coupling coefficients

We consider a protocol for state preparation and coherent control of molecular ions that involves interaction with far-detuned continuous wave (CW) Raman beams with a wavelength $\lambda_{laser} = 1051\,\text{nm}$ ($\nu = 285.5\,\text{THz}$).
The molecular ions that will be used in this context are in their electronic and vibrational ground states and the Raman beams are far-detuned from the electronic transition between the ground and the first excited states. The molecular eigenstates belonging to the same rotational levels can be coupled with the Raman beams which excite *stimulated Raman transitions* on the motional-adding sideband [12].
Let's consider a three-level system composed of two molecular states in the same rotational manifold J, $|a\rangle = |J, m_{Fa}, \xi_a\rangle$ and $|b\rangle = |J, m_{Fb}, \xi_b\rangle$, and an excited intermediate electronic state $|e\rangle$. We denote the frequency difference as ω_{ae} and ω_{be}, respectively. We assume a bichromatic polarized light field having frequency $\{\omega_1; \omega_2\}$, derived from the CW laser whose frequency is split by two acousto-optic modulators (AOMs). We call their electric field amplitudes as $\{|\vec{E}_1|; |\vec{E}_2|\}$, and their polarizations as $\{\vec{q}^{(1)}; \vec{q}^{(2)}\}$.
In general, the polarization is expressed as

$$\vec{q}^{(n)} = q_{-1}^{(n)}\sigma^- + q_0^{(n)}\pi + q_1^{(n)}\sigma^+, \tag{2.37}$$

with $|\vec{q}^{(n)}|^2 = 1$. The π polarization is oriented parallel to the quantization axis, defined by the external magnetic field $\vec{B}$, and addresses transitions with $\Delta m = 0$, and σ^+ (σ^-) po-

larization rotates clockwise (anticlockwise) around the quantization axis when viewed along the wavevector, selecting $\Delta m = +1$ ($\Delta m = -1$) [13].
The experimental configuration uses two Raman beams with $\vec{q}^{(1)} = \sigma^-$ and $\vec{q}^{(2)} = \pi$ polarizations: we call $\omega_1 = \omega_{\sigma^-}$ and $\omega_2 = \omega_\pi$ their corresponding frequencies. Both laser fields are far off-resonant with respect to the $|a\rangle \leftrightarrow |e\rangle$ and $|b\rangle \leftrightarrow |e\rangle$ transitions [14]: in this way, as the population transfer to state $|e\rangle$ is negligible, we have full control of a pair of coupled states $\{|a\rangle ; |b\rangle\}$. The transition between the two ground states is realized as a stimulated Raman process in which one laser drives photon absorption, then the second stimulates photon emission, enhancing Raman scattering and leading to coherent transitions between $|a\rangle$ and $|b\rangle$. This is the so-called counter-rotating transition [9, 15]. With the $\sigma^- - \pi$ configuration, this results in the selection rule $\Delta m = \pm 1$. In addition to this, it is possible to have a co-rotating transition, where the photon is first stimulated, then absorbed. Since we are dealing with an off-resonant laser field, co-rotating terms cannot be neglected. A schematic of this process is shown in Figure 2.4.

Additionally, the laser field can drive Raman transitions on the blue-sideband. As

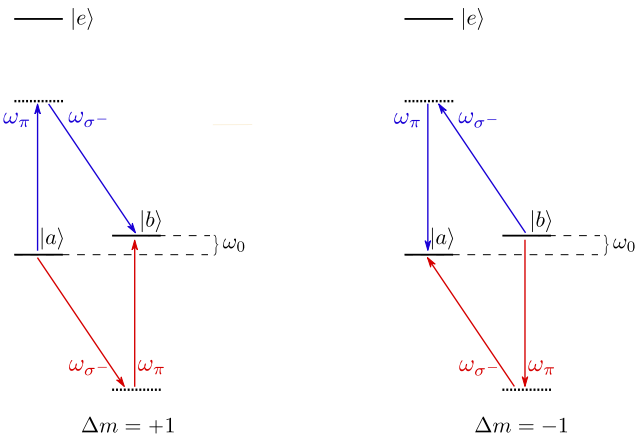

Figure 2.4: Raman coupling schemes with $\sigma_- - \pi$ polarization configuration. Raman laser excites two-level transitions with energy difference $\hbar\omega_0$, being off-resonant from $|e\rangle$, at $\Delta m = +1$ (left) and $\Delta m = -1$ (right). Counter-rotating (blue lines) and co-rotating (red lines) contributions are highlighted.

can be seen in Figures 2.5a and 2.5b, since the difference of Raman beam frequencies is shifted by ω_t and the molecular levels are equally spaced, blue-sideband Raman transitions select either the $\Delta m = -1$ or $\Delta m = +1$ transition which adds one phonon, since the other possible transition is off-resonant by ω_t when in the motional ground state. Indeed, in order to drive a molecular transition at frequency δ on the BSB, one has to set $\omega_\pi - \omega_{\sigma^-} = \omega_t + \delta$ for $\Delta m = +1$, and $\omega_{\sigma^-} - \omega_\pi = \omega_t + \delta$ for $\Delta m = -1$. Note that carrier Raman transitions are not directional: as shown in Figure 2.5c, given an initial

state, both $\Delta m = -1$ and $\Delta m = +1$ transitions are driven.

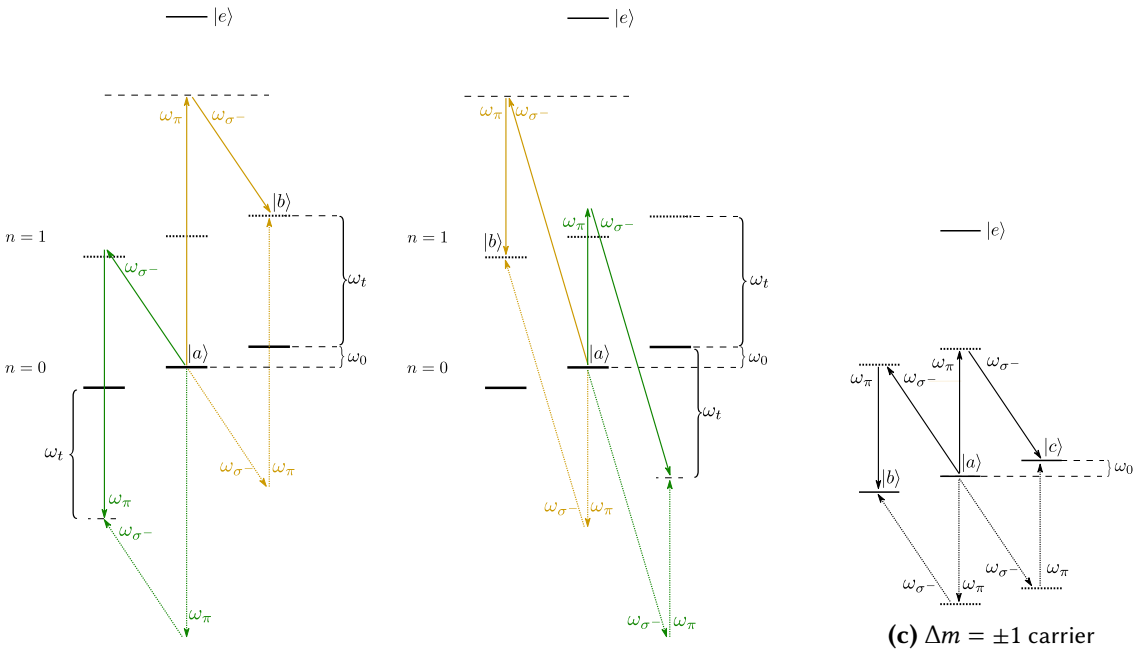

(a) $\Delta m = +1$ BSB transition. **(b)** $\Delta m = -1$ BSB transition. **(c)** $\Delta m = \pm 1$ carrier transition.

Figure 2.5: Raman beams excites two-level transitions with energy difference $\hbar\omega_0$, being off-resonant from $|e\rangle$. BSB transition for $\Delta m = +1$ (left), for $\Delta m = -1$ (center) and carrier transition (right) are displayed. BSB transitions select directionality (yellow line), while the other (green line) is off-resonant. The carrier transition is not directional. Counter-rotating (solid lines) and co-rotating (dashed lines) contributions are highlighted.

Hence, BSB Raman transitions are preferred for the directionality in the transition. In Appendix C, we report the computation of the coupling strength between the initial state $|J, m_{Fa}, \xi_a\rangle$ and the final state $|J, m_{Fb}, \xi_b\rangle$: this coefficient accounts for all possible contributions from transitions involving intermediate states with $J_e = J \pm 1$. Thus, when the molecule interacts with the Raman laser driving at a reduced Rabi frequency Ω_{Raman}, the effective Rabi frequency of the Raman transition can be expressed as the product of a transition-dependent term, c_{ab}, namely the coupling coefficient, and a laser-dependent term, Ω_{Raman}:

$$\Omega_{ab} = c_{ab}\Omega_{\text{Raman}}. \tag{2.38}$$

2.4 Quantum logic spectroscopy

Molecular spectroscopy is a fundamental tool to investigate molecular internal structure, revealing detailed information about their electronic, vibrational, and rotational levels.

However, differently from atoms, molecules possess a richer and more complicated internal structure, with many different decay channels and the possibility of interactions between molecular states. As a consequence, observing coherent optical excitation and achieving state-selective readout in molecules is significantly more challenging, since population can rapidly diffuse to many uncoupled internal states. This limits the applicability of techniques based on closed optical cycling transitions, which are used in atomic systems. These challenges are further increased in experiments involving isolated, single trapped molecular ions, for which the signal-to-noise ratio is low [16].
To study a molecular ion's internal structure with high precision and exert control over the molecular state, quantum logic spectroscopy (QLS) is implemented. QLS is a method which maps the internal level of a *spectroscopy ion* (the one being studied) to the internal level of a co-trapped *logic ion* used for readout, for which efficient control techniques are available. This is achieved through their shared motional mode, as schematized in Figure 2.6 [17, 18].
We employ the $^{40}Ca^{+}$ isotope as the logic ion, which possesses well characterized optical transitions, efficient closed-cycling transition, and long coherence times [16, 19]. The atomic electronic structure of the first three orbitals in Ca^{+} and their lifetimes are shown in Figure 2.7: in what follows, the $D_{5/2}$ and $S_{1/2}$ states will denote the Zeeman states $D_{5/2}(m_J = -1/2)$ and $S_{1/2}(m_J = -1/2)$, respectively. The spectroscopy ion is a molecular ion, in our case either $^{40}CaH^{+}$ or $^{40}CaOH^{+}$. The logic and spectroscopy ions are co-trapped in a linear RF Paul trap in which the ions can oscillate in the in-phase or out-of-phase axial motional modes. This shared mode caused by the Coulomb potential can be sympatetically cooled down to the ground state.

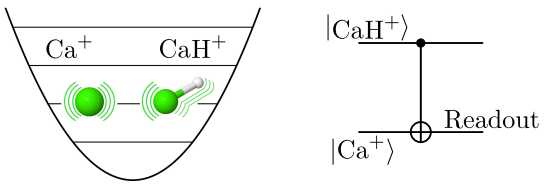

Figure 2.6: Schematic of the co-trapped $^{40}Ca^{+}$-$^{40}CaH^{+}$ system and molecular state readout.

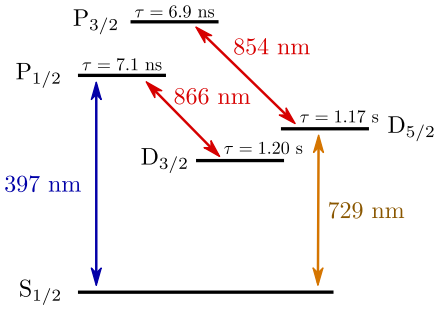

Figure 2.7: Ca^{+} energy level structure, with transition wavelength and decay times.

The QLS experimental protocol is schematized in Figure 2.8 and consists of four parts:

- **State preparation**: at room temperature, the CaH^+ and $CaOH^+$ molecular ions are in their electronic and vibrational ground state, and in a mixture of rotational states. The Ca^+ logic ion is treated as a qubit with $|0\rangle = S_{1/2}$ and $|1\rangle = D_{5/2}$, and it is used to cool the motional mode to $|n = 0\rangle$. First, Doppler cooling is applied on the $S_{1/2} \leftrightarrow P_{1/2}$ transition using the 397 nm laser, and repumping the $D_{3/2} \leftrightarrow P_{1/2}$ transition with an 866 nm laser. Then sideband cooling brings the system to the motional ground state, by exciting the $S_{1/2} \rightarrow D_{5/2}$ motional-subtracting sideband transition at 729 nm, and the carrier $D_{5/2} \rightarrow P_{3/2}$ transition with a 854 nm repumping laser, followed by the fast decay $P_{3/2} \rightarrow S_{1/2}$: this cycle brings the system back to the original state with one less photon.

- **Probe molecular transition**: we apply a motional-adding pulse which acts on the internal structure of the molecule. We use the 1051 nm CW-Raman beam as previously explained. The phonon number increases by 1 if the transition occurs.

- **Mapping to the atomic ion**: the shared motional mode is mapped to the Ca^+ ion electronic state using a motional-subtracting at 729 nm, which in the configuration considered in this thesis acts on the $S_{1/2}\,|n = 1\rangle \leftrightarrow D_{5/2}\,|n = 0\rangle$ transition. If the molecular transition was successfully driving in the previous step, meaning that the motional state is now $|n = 1\rangle$, this transition at 729 nm occurs as well; otherwise, the logic ion is left in the $S_{1/2}\,|n = 0\rangle$ state.

- **Readout**: to read out the molecular transition, we apply the 397 nm laser which excites the transition $S_{1/2} \rightarrow P_{1/2}$ in the logic ion. If the logic ion was in $S_{1/2}$ (meaning that the molecular transition did not happen), the 397 nm transition occurs and immediately decays to $S_{1/2}$ in a closed cycle producing fluorescence. At the same time, an 866 nm laser repumps the transition $D_{3/2} \leftrightarrow P_{1/2}$ to avoid that a second decay channel bringing the population into the dark $D_{3/2}$ state. Conversely, a lack of fluorescence means the ion is in the $D_{5/2}$ state and that the molecular transition was successful.

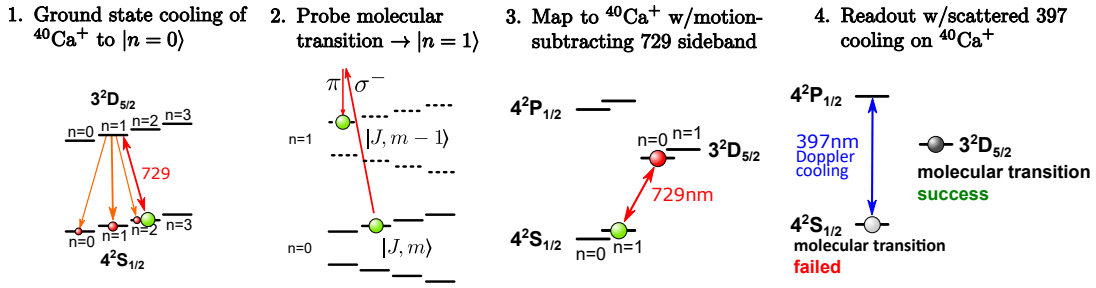

Figure 2.8: Quantum logic spectroscopy protocol for $^{40}CaH^+$ or $^{40}CaOH^+$ molecular ion state detection, co-trapped with a Ca^+ atomic ion.

In this way, the internal molecular state is not subject to destructive measurements,

but rather non-destructive ones, and is therefore preserved. QLS thus allows subsequent manipulation of the molecular state and molecular spectroscopy [20].

2.5 Optical dipole force (ODF)

In the context of quantum logic spectroscopy, the Raman beams with π and σ^- polarizations are used to drive stimulated Raman transitions on the motional-adding sideband. However, the beam polarizations are not perfectly orthogonal, and each beam contains small spurious components of different polarization. As shown in Figure 2.9, when there exists a non-zero component of a given polarization (expressed in the spherical basis) in both beams, and the two beams are detuned from each other by $\omega_t + \Delta_{\mathrm{BSB}}$, it becomes possible to off-resonantly drive coherent motion without inducing transitions in the internal molecular state. In this regime, the light fields produce an AC Stark shift of the atomic and molecular levels, which can be interpreted as a position-dependent optical potential. The gradient of this potential gives rise to a force field. Due to the interference between the two beams having the same polarization, whose frequency difference is close to the trap frequency ω_t, the resulting optical potential forms a traveling wave oscillating near ω_t [21, 22].

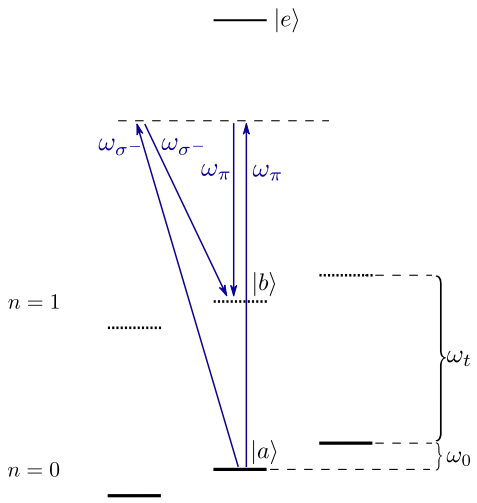

Figure 2.9: When spurious Raman beams contain same polarization components ($\sigma_- - \sigma_-$ or $\pi - \pi$), the optical dipole force displaces the motional state without changing the internal level.

This generates a periodic force called optical dipole force (ODF) that coherently drives the motional degree of freedom while leaving the internal state unchanged. It displaces

the ground state $|0\rangle$ to a coherent state $|\alpha\rangle$ [23]. Hence, the ODF can be modeled with a displacement operator $\mathscr{D}(\alpha) = e^{\alpha\hat{a}^\dagger - \alpha^*\hat{a}}$, such that:

$$|\alpha\rangle = \mathscr{D}(\alpha)\,|0\rangle\,. \tag{2.39}$$

The Hamiltonian of a harmonic oscillator, representing the motional mode, defines the coherent displacement. In the interaction picture, considering the BSB rotating frame shifting the frequencies by $-\omega_t$, the ODF Hamiltonian reads as:

$$\hat{H}_{\mathrm{ODF}}(t) = \hbar\left[f(t)\hat{a}^\dagger + f^*(t)\hat{a}\right] = \frac{i\hbar\Omega_{\mathrm{ODF}}}{2}\left(\hat{a}^\dagger e^{-i\delta_{\mathrm{ODF}}t} - \hat{a}e^{i\delta_{\mathrm{ODF}}t}\right) \tag{2.40}$$

where δ_{ODF} is the frequency detuning with respect to the motional frequency ($\omega_l - \omega_0 = \omega_t$), and Ω_{ODF} is the Rabi frequency of the ODF. A larger Ω_{ODF} corresponds to a larger fraction of spurious polarization in the beams, and thus to a stronger ODF effect.
With a non-zero detuning, the ODF Hamiltonian is time-dependent. The time-evolution operator is defined as a time-ordered exponential:

$$U(t) = \mathscr{T}\,\exp\left\{-\frac{i}{\hbar}\int_0^t \hat{H}_{\mathrm{ODF}}(t')dt'\right\}, \tag{2.41}$$

or expanded using the Magnus expansion as $U(t) = \exp\left[\Omega(t)\right]$, with $\Omega = \sum_{n=1}^{\infty}\Omega_n(t)$ [24], with the first two orders given by:

$$\begin{aligned}
\Omega_1 &= \frac{i}{\hbar}\int_0^t dt_1 \hat{H}_{\mathrm{ODF}}(t_1) \\
\Omega_2 &= -\frac{1}{2\hbar^2}\int_0^t dt_1 \int_0^{t_1} dt_2 \left[\hat{H}_{\mathrm{ODF}}(t_1), \hat{H}_{\mathrm{ODF}}(t_2)\right].
\end{aligned} \tag{2.42}$$

Using the Hamiltonian in Eq. 2.40, one gets:

$$\begin{aligned}
\Omega_1 &= \frac{i\Omega_{\mathrm{ODF}}}{\delta_{\mathrm{ODF}}}\left[\hat{a}^\dagger \sin\left(\frac{\delta_{\mathrm{ODF}}t}{2}\right)e^{-\frac{\delta_{\mathrm{ODF}}t}{2}} + h.c.\right] = \alpha\hat{a}^\dagger - \alpha^*\hat{a}, \\
\Omega_2 &= -i\left(\frac{\Omega_{\mathrm{ODF}}}{2\delta_{\mathrm{ODF}}}\right)^2\left[\delta_{\mathrm{ODF}}t - \sin(\delta_{\mathrm{ODF}}t)\right] = -i\beta(t),
\end{aligned} \tag{2.43}$$

with

$$\begin{aligned}\alpha &= \frac{i\Omega_{\mathrm{ODF}}}{\delta_{\mathrm{ODF}}} e^{-\frac{i\delta_{\mathrm{ODF}}t}{2}} \sin\left(\frac{\delta_{\mathrm{ODF}}t}{2}\right), \\ \beta &= \left(\frac{\Omega_{\mathrm{ODF}}}{2\delta_{\mathrm{ODF}}}\right)^2 \left[\delta_{\mathrm{ODF}}t - \sin(\delta_{\mathrm{ODF}}t)\right].\end{aligned} \tag{2.44}$$

Since $\beta(t)$ is not an operator anymore, higher order terms in the expansion vanish, thus making the time-evolution operator the displacement operator:

$$U(t) = e^{-i\beta(t)} D(\alpha). \tag{2.45}$$

Being off-resonant of δ_{ODF}, the motional state undergoes a displacement whose trajectory in phase space is circular, as shown in Figure 2.10. The diameter of the trajectory is $2\pi r = \frac{\Omega_{\mathrm{ODF}}}{\delta_{\mathrm{ODF}}}$, spaced with an angular speed equal to δ_{ODF}, and the loops are closed at $t = \frac{2\pi}{\delta_{\mathrm{ODF}}}$ [25]. Each time the loop is closed, the motional state acquires a global geometrical phase, $\beta(t)$, which is proportional to the enclosed area [26]. During the QLS probing

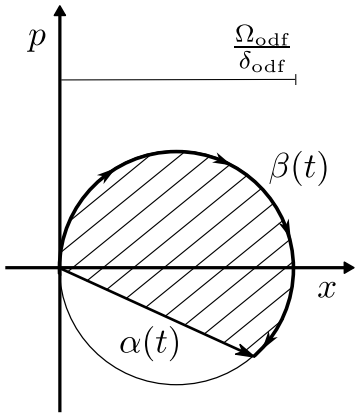

Figure 2.10: Following Eq. (2.45), the detuned optical dipole force produces a coherent displacement of the motional state in the phase space following a circular trajectory.

of the molecular transition, motional-adding sideband pulses are driven in order to excite a given molecular transition. We call the molecular transition frequency ω_{mol}, and the eventual frequency detuning from the motional-adding molecular transition Δ_{BSB}. The corresponing BSB Hamiltonian follows Eq. 2.18.

As can be seen in Figure 2.11, the ODF Hamiltonian and the motional-adding molecular transition Hamiltonian have different detuning dependencies [27]: while the first is δ_{ODF} off-resonant, the second is $\Delta_{\mathrm{BSB}} = \delta_{\mathrm{ODF}} - \omega_{\mathrm{mol}}$ off-resonant.

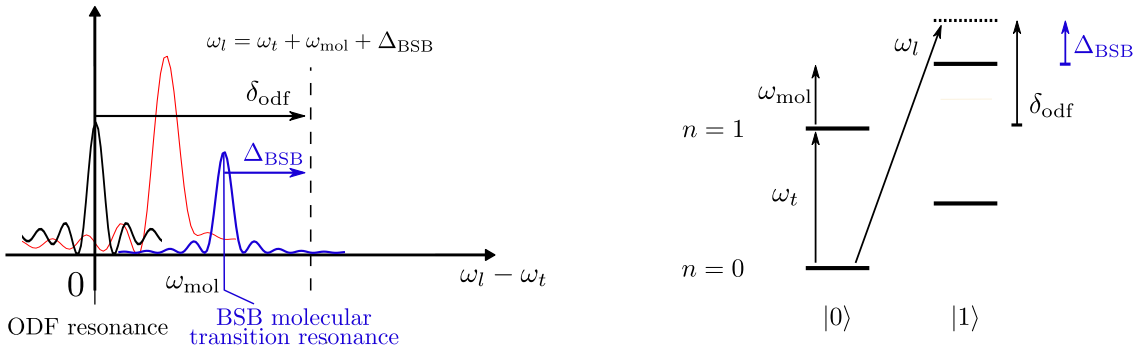

Figure 2.11: Frequency-domain (left) and level-diagram (right) representation of the motional-adding sideband molecular transition Δ_{BSB} and motional δ_{ODF} detunings, with respect to the BSB reference frame. The black curve represents the ODF signal alone, the blue one the BSB transition signal alone, while the red one the signal coming from the combined ODF and BSB transition action.

The resulting Hamiltonian is given by:

$$\begin{aligned}\hat{H} &= \hat{H}_{\text{BSB}} + \hat{H}_{\text{ODF}} \\ &= i\hbar\frac{\Omega_{\text{BSB}}}{2}\left(e^{-i\Delta_{\text{BSB}}t}\hat{a}^\dagger\hat{\sigma}_+ - e^{+i\Delta_{\text{BSB}}t}\hat{a}\hat{\sigma}_-\right) + \frac{i\hbar\Omega_{\text{ODF}}}{2}\left(\hat{a}^\dagger e^{-i\delta_{\text{ODF}}t} - \hat{a}e^{i\delta_{\text{ODF}}t}\right),\end{aligned} \tag{2.46}$$

where Ω_{BSB} is the effective Rabi frequency of the BSB Hamiltonian. The signal associated to the BSB molecular transition is thus modified due to the presence of the ODF.

2.6 Rapid adiabatic passage

Molecular ions possess a rich internal level structure. Therefore, these large-scale multi-level systems require highly robust manipulation techniques: experimental parameters are prone to noise or fluctuations which can reduce driving efficiency and decrease state of operation fidelity. In particular, the necessity to realize precise state preparation of the molecular ions is analyzed, which considers the population transfer of each rotational manifold in a given state: a naive approach attempting to drive Rabi oscillations between pairs of nearly-degenerate states often does not work or is time-consuming and highly sensitive to experimental imperfections. These experimental imperfections affect the Raman Rabi frequency and frequency detunings.
An alternative approach is provided by the use of rapid adiabatic passage (RAP) pulses [28]. The RAP pulses allow for population swapping between two states in a more robust and efficient manner, as they are less sensitive to experimental imperfections [29]. Although experimentally more demanding to implement, these pulses can be realized

either as carrier or sideband transitions: in our context of stimulated Raman transitions, acousto-optic modulators (AOMs) are used to ad-hoc sweep the $\omega_{\sigma-}$ and ω_{π} frequencies, and thus create the RAP pulses.
Moreover, in contrast to driving Rabi oscillations, RAP pulses enable simultaneous manipulations of multiple different manifolds, which are subsets of molecular states: as the molecular manifold structures are similar, differing only by small variations in the energy splitting between the states, a single RAP pulse can perform population transfer of several manifolds at the same time, resulting in a great gain in terms of time and fidelity.
The rapid adiabatic passage pulse consists of a time-dependent reduced Rabi frequency $\Omega(t)$ and a time-dependent frequency detuning $\Delta(t)$. It is applied over a finite time window $0 \leq t \leq T$, outside of which the reduced Rabi frequency is assumed to vanish. In particular, we consider a Gaussian reduced Rabi frequency envelope and a linear frequency chirp, described by [30]:

$$\begin{cases} \Omega(t) = \Omega_0 e^{-\frac{(t-\frac{T}{2})^2}{2\sigma^2}}, \\ \Delta(t) = \dfrac{D}{T}\left(t - \dfrac{T}{2}\right) + \delta \end{cases} \quad \text{with} \quad 0 \leq t \leq T, \tag{2.47}$$

where $\delta = \omega_l - \omega_{\text{mol}} - \omega_t$ represents the frequency detuning from the two-level blue-sideband transition frequency.
Thus, $\Delta(t)$ ranges from $-D/2 + \delta$ at $t = 0$ to $D/2 + \delta$ at $t = T$, where D is the frequency sweep range, and T the time duration of the RAP pulse. Ω_0 is the peak reduced Rabi frequency (reached at $T/2$), and σ the temporal pulse width of the Gaussian.
The evolution of a system driven by a RAP pulse can be depicted in the Bloch sphere, where the two qubit states are positioned at the poles of the Bloch sphere $\hat{z}$-axis. The evolution of the state vector $|\psi\rangle$ is represented using the Bloch vector $\vec{S} \in \mathbb{R}^3$ and defined by the optical Bloch equations (OBEs), neglecting coherences effect:

$$\frac{d\vec{S}}{dt} = \vec{Q} \times \vec{S}, \tag{2.48}$$

where $\vec{Q}$ is the torque vector. In this case, it is defined as $\vec{Q}(t) = (\Omega(t), 0, \Delta(t))$ [30]. This torque vector needs to slowly change over time, from $\vec{Q}(0)$ to $\vec{Q}(T)$: hence, to ensure that the laser parameter varies slowly over time, the following adiabaticity condition

needs to be satisfied [31]:

$$\frac{\left|\frac{d\vec{Q}}{dt}\right|}{|\vec{Q}|} \ll |\vec{Q}|. \tag{2.49}$$

This translates into the following condition:

$$\mathscr{A}(t) = \frac{\sqrt{\Omega^2(t)\frac{(t-T/2)^2}{\sigma^4} + \frac{D^2}{T^2}}}{\Omega^2(t) + \Delta^2(t)} \ll 1. \tag{2.50}$$

Using $\Omega_0 = 50\,\text{kHz}$, $T = 5\,\text{ms}$, $\sigma = T/5$, and $D = 100\,\text{kHz}$ for a molecular transition with $\delta = -22\,\text{kHz}$, the time evolution of the Bloch vector and the corresponding adiabaticity parameter $\mathscr{A}(t)$ are depicted in Figure 2.12.

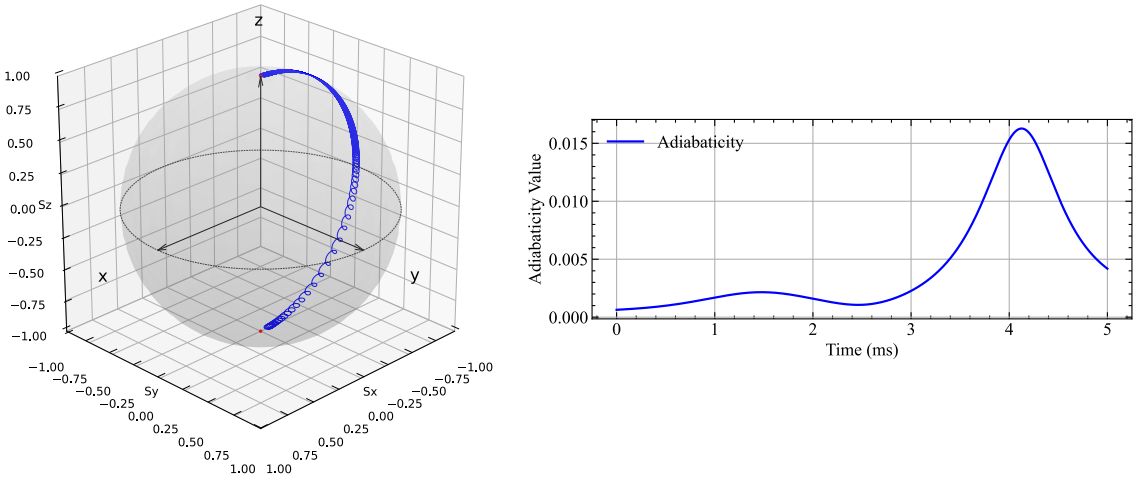

Figure 2.12: With $\Omega_0 = 50\,\text{kHz}$, $T = 5\,\text{ms}$, $\sigma = T/5$, $D = 100\,\text{kHz}$, and $\delta = -22\,\text{kHz}$, the time evolution of the state vector $\vec{S}$ in the Bloch sphere starting from $+\hat{z}$ and following optical Bloch equations (left); and of the adiabaticity parameter $\mathscr{A}(t)$ (right).

Considering a BSB molecular transition ω_{mol} with effective Raman Rabi frequency $\Omega_0 = \eta\Omega_{ab}$ and frequency detuning from the BSB molecular transition δ, the BSB Hamiltonian reads as:

$$\hat{H}_{\text{BSB}}^{RAP}(t) = \frac{\hbar\Omega(t)}{2}\left(e^{-i\Delta(t)t}\hat{a}^{\dagger}\hat{\sigma}_{+} + e^{+i\Delta(t)t}\hat{a}\hat{\sigma}_{-}\right). \tag{2.51}$$

3

Molecular quantum logic spectroscopy simulations

In this Chapter we focus on one calcium ion (Ca^+) and one molecular ion confined in a linear Paul trap. The shared translational degrees of freedom of the ion crystal can be cooled efficiently via sympathetic cooling of the molecular ions through laser-cooled atomic ions, which is a crucial prerequisite for high precision quantum control [32, 33, 34]. Several heteronuclear molecular ions have been studied in the context of ion-trap physics and quantum logic spectroscopy (QLS) [9, 20, 35, 36, 37, 38].
Molecular ions such as $^{40}CaH^+$ and $^{40}CaOH^+$ are of particular relevance since they form nuclear spin 1/2 linear rotor molecules, which provide a rich internal structure for spectroscopic investigations and are typically generated inside the trap through chemical reactions. These reactions occur between trapped Ca^+ ions and residual background gas molecules present in the vacuum chamber. At room temperature, these reactions proceed efficiently and rapidly populate the electronic and vibrational ground states of the molecular ions, while leaving them distributed across a thermal mixture of rotational states [9, 39, 40].
The QLS framework plays a central role in enabling precision spectroscopy of such molecular ions, where Ca^+ serves as the logic ion [41]. The ions are coupled through their common motional modes in the Paul trap, such that laser manipulations performed on one ion can be mapped onto the other. For instance, blue sideband (BSB) excitations can be implemented on the molecular ion and read out through red sideband (RSB) transitions on the atomic ion. In this way, the otherwise inaccessible internal state of the molecular ion becomes experimentally observable.
The purpose of this Chapter is to investigate the quantum-mechanical properties of these molecular ions with particular attention to their interaction with laser light. Building on this foundation, we proceed to analyze the molecular structure in detail and to simulate the hyperfine molecular spectra, which guides the experimental measurements

via high-resolution molecular QLS.

3.1 CaH^+ and $CaOH^+$ molecular ions

The molecular ions that will be used in this context ($^{40}CaH^+$ and $^{40}CaOH^+$) are in their electronic and vibrational ground states and the Raman beams are far-detuned from the electronic transition between the ground and the first excited states: for $^{40}CaH^+$ it occurs at a frequency of $\nu \simeq 750\,\text{THz}$ [36], while for $^{40}CaOH^+$ at a frequency of $\nu \simeq 1100\,\text{THz}$ [39, 42].
The diatomic molecule $^{40}CaH^+$ has an experimentally measured rotational constant of $B_R/h = 142.501\,777\,9(17)\,\text{GHz}$ in its vibrational ground state, while the first order correction is 5 order of magnitude smaller [36, 20]. The nuclear spin $I = 1/2$ comes from the hydrogen nucleus. The nuclear spin-rotation coupling c_{IJ} and the g-factor for rotation are experimentally computed in the ground vibrational state $v = 0$, and reported for the first 15 rotational states in Table 3.1 [9]:

Table 3.1: Numerical values of c_{IJ} and g_J for the first 15 rotational manifolds J of $^{40}CaH^+$ [9].

	J value														
	0	1	2	3	4	5	6	7	8	9	10	11	12	13	14
c_{IJ} (kHz)	8.27	8.26	8.26	8.26	8.26	8.25	8.25	8.24	8.24	8.23	8.22	8.21	8.20	8.19	8.18
g_J	-1.35	-1.35	-1.35	-1.34	-1.34	-1.34	-1.34	-1.34	-1.33	-1.33	-1.33	-1.32	-1.32	-1.31	-1.31

The $^{40}CaH^+$ electric dipole moment is computed to be $d \simeq 5.3$ Debye [43]. The Boltzmann constant is $k_B = 2.083\,66 \times 10^7\,\text{kHz}\,\text{K}^{-1}$, while the nuclear magneton $\mu_N = 0.762\,259\,323\,\text{kHz}\,\text{G}^{-1}$, and the proton g-factor $g_I = 5.585\,694\,689\,3$ [44, 45, 46]. Using these values, one can compute the amplitudes of the hybridized Zeeman states, the eigenenergies, and the coupling coefficients among those. In Figure 3.1 the levels for the $J = 2$ rotational manifold are shown for different magnetic fields regimes.

The triatomic molecule $^{40}CaOH^+$ is calculated to be linear in its ground vibrational state $v = 0$. The rotational constant has been calculated to be $B_R/h = 10.96\,\text{GHz}$ in the vibrational ground state [39]. The nuclear spin $I = 1/2$ comes from the hydrogen nucleus. The nuclear spin-rotational interaction c_{IJ} and the g-factor for rotation have been calculated to be $c_{IJ} = 1.49\,\text{kHz}$ and $g_J = -0.036$ [47]: these values have not been determined experimentally and their precise determination will be possible only after obtaining the spectrum of the molecule. The electric dipole moment has been calculated

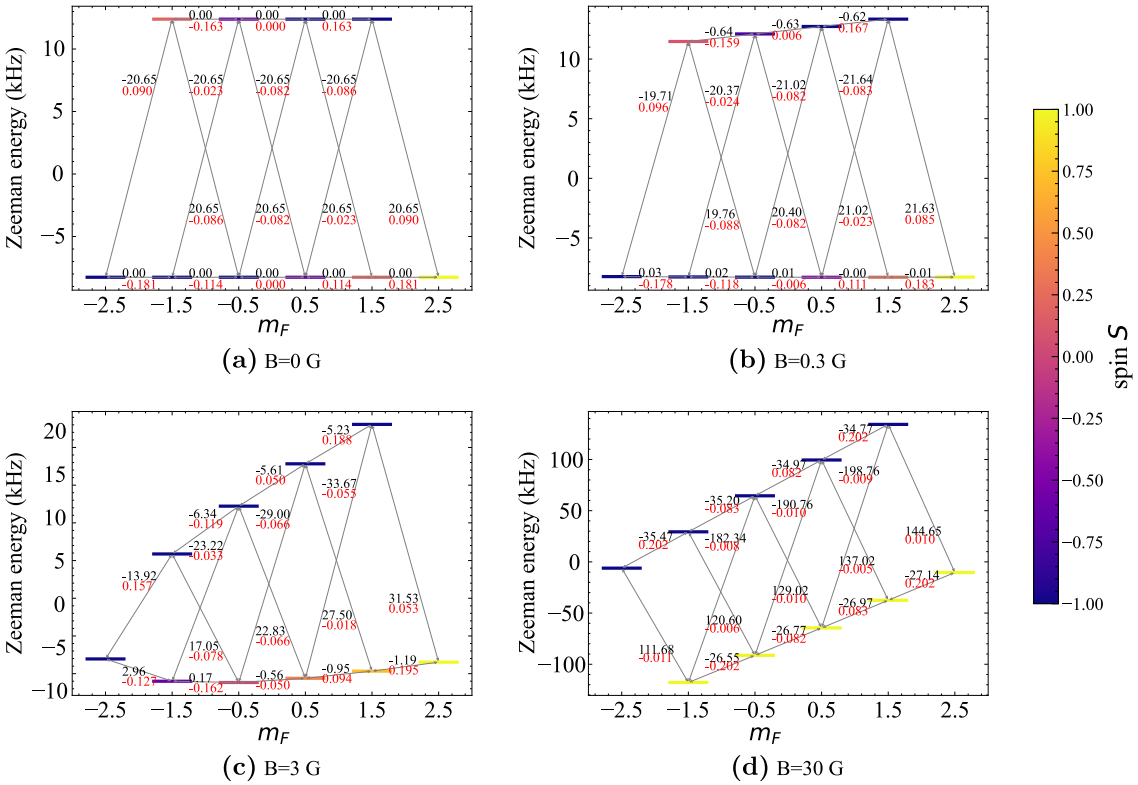

(a) B=0 G (b) B=0.3 G (c) B=3 G (d) B=30 G

Figure 3.1: $^{40}CaH^+$ states and energies for the $J = 2$ manifold, for different regimes: zero B-field (3.1 a), Zeeman (3.1 b), intermediate (3.1 c), Paschen-Back (3.1 d). The energy differences (black, in kHz), and coupling coefficients (red) are reported for the $\Delta m = -1$ Raman transitions. The colorbar represents the quantity defined in Eq. (2.25).

to be $d = 6.3$ Debye [47]. The structure of the $J = 2$ manifold is shown in Figure 3.2 for different magnetic field regimes.

The rotational state populations and the $\mathscr{F}(J, B)$ FOM of the B-field regime for the molecular ions $^{40}CaH^+$ and $^{40}CaOH^+$ are displayed in Figure 3.3.

In both molecules, degeneracy occurs at zero magnetic field, and in both the Zeeman and Paschen-Back regimes the transition frequencies occurring inside the sub-manifold are all similar; however, in the intermediate regime, the signature transition frequencies are significantly different from the ones of the other Zeeman transitions within each sub-manifold. Moreover, the signature transition frequencies are J-dependent in the intermediate regime, and thus have unique frequencies making it possible to readout the occupied level J with a single transition, assuming population has been pumped to one of the two states connecting it. For this reason, if an appropriate optical pumping scheme can concentrate population into the stretched and penultimate states, then the signature transitions can be driven and used for the identification of which J-manifold

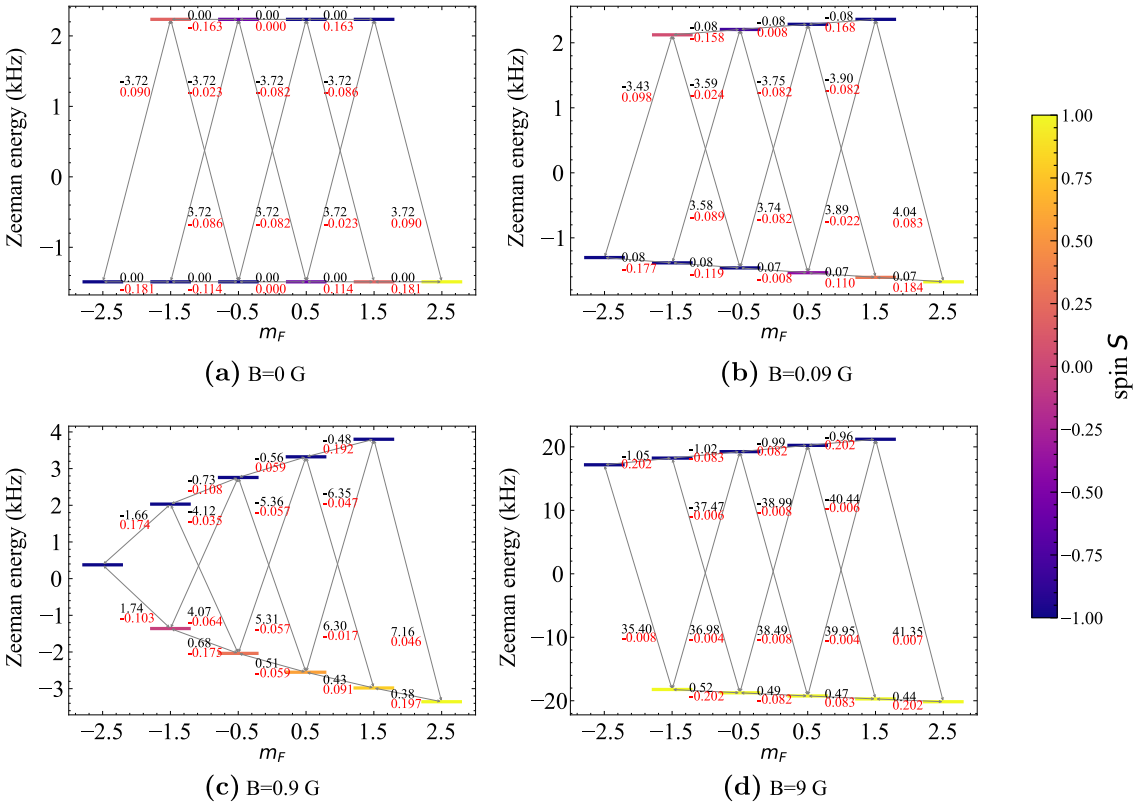

Figure 3.2: $^{40}CaOH^+$ states and energies for the $J = 2$ manifold, for different regimes: zero B-field (3.2 a), Zeeman (3.2 b), intermediate (3.2 c), Paschen-Back (3.2 d). The energy differences (black, in kHz), and coupling coefficients (red) are reported for the $\Delta m = -1$ Raman transitions. The colorbar represents the quantity defined in Eq. (2.25).

is occupied. To highlight this concept, for both $^{40}CaH^+$ and $^{40}CaOH^+$ molecules, the signature transition frequencies for the rotational manifolds J are displayed in Figure 3.4 in the intermediate regime for B, together with the neighboring transitions (used as a representative of the transitions within a sub-manifold) and the sub-manifold splittings.

In the intermediate regime for $^{40}CaH^+$, the signature transition frequencies are effectively different from those of the penultimate transition; they are also J-dependent since consecutive signature transitions differ several kHz from each other.
Differently from $^{40}CaH^+$, the $^{40}CaOH^+$ molecule has a thermal distribution at room temperature where around 50 rotational states J are occupied (see Figure 3.3), such that a significant fraction of the population is in all three B-field regimes. For this reason, once we choose the B-field in which most manifolds lie in the intermediate regime for $^{40}CaOH^+$ (for example, at $B = 3.27$ G), we need to deal with the lower rotational manifolds being in the Paschen-Back regime, and the higher rotational manifolds in the Zeeman one (see Figure 3.3). In this way, as shown in Figure 3.2 the target state transi-

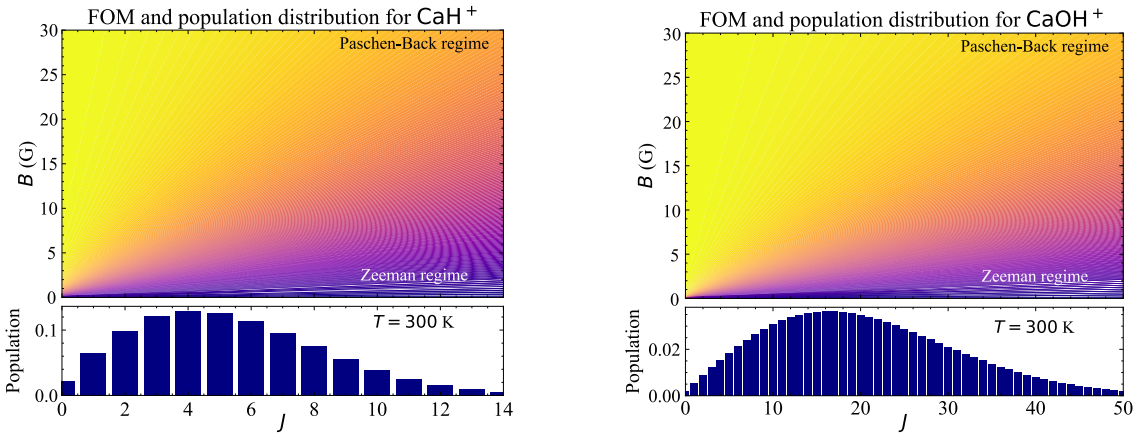

Figure 3.3: Figure of merit of the B-field (defined in Eq. (2.31)) and rotational thermal population (defined in Eq. (2.32)) at $T = 300\,\mathrm{K}$ for $^{40}CaH^+$ (left) and $^{40}CaOH^+$ (right).

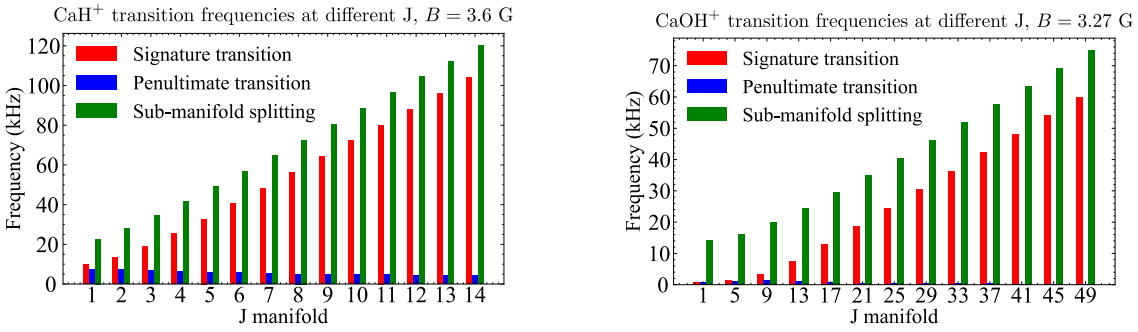

Figure 3.4: Signature transition frequencies (red), penultimate upper transition (blue) and sub-manifold splittings (green) for $^{40}CaH^+$ at $B = 3.6\,\mathrm{G}$ (left) and $^{40}CaOH^+$ at $B = 3.27\,\mathrm{G}$ (right).

tions from being next to the lower sub-manifold in the Zeeman regime manifolds (high J), to being next to the upper sub-manifold in the Paschen-Back manifolds (low J). Thus, the signature transitions remain J-dependent except for the ones of the first rotational manifolds, which differ by only a few hundreds of Hz from each other. Decreasing the B-field would bring more rotational manifolds in the intermediate regime, but also many others in the Zeeman one (see Figure 3.3) making the signature transitions much more similar to the sub-manifold splitting transitions for a broader range of manifolds. The drawback of having the lower-J signature transition frequencies very close and overlapping is challenging and unavoidable, having a significant impact on on the ability to distinguish neighboring J states and thus the determination of the molecular state, even though the probability of being in a low-J rotational state is relatively small.

Because the signature transition frequencies in $^{40}CaOH^{+}$ overlap, they are particularly sensitive to experimental imperfections—such as Raman detuning miscalibration and trap frequency fluctuations—as well as variations in the Hamiltonian parameters from theoretical calculations, as the coefficients c_{IJ} and g_J have so far only been obtained from theory. Their experimental determination will become possible once an appropriate optical pumping scheme is implemented, as has already been demonstrated for ^{40}CaH [20]. Hence, we also investigate how the signature transition frequencies change when varying c_{IJ} and g_J from their theoretical values. The corresponding relative variations are illustrated in Figure 3.5.

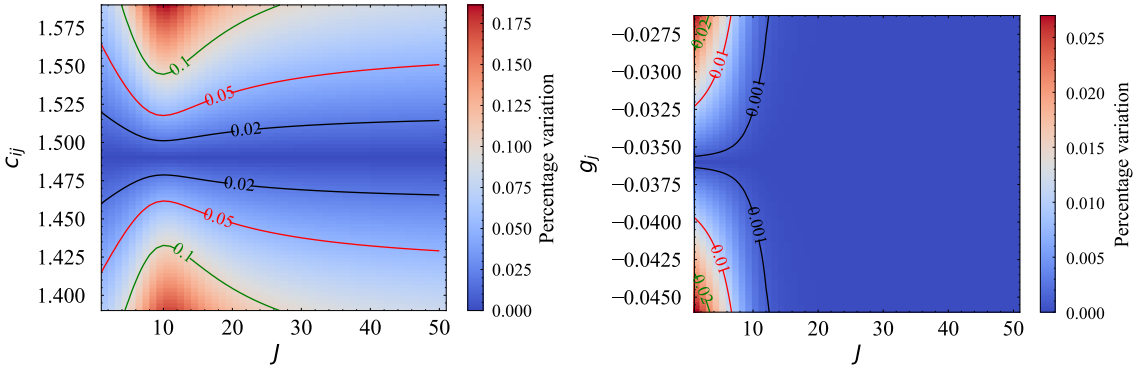

Figure 3.5: Signature transition frequency relative variation when varying c_{IJ} (left) and g_J (right) for the $^{40}CaOH$ molecular ion.

Small variations of c_{IJ} lead to significant relative shifts of the signature transition frequencies, whereas g_J, already small, does not induce changes of comparable magnitude.

3.2 Physics simulator

To simulate the behavior of the molecules, a *physics simulator* was developed.
This physics simulator has the aims to implement a computationally efficient model, capable of executing real-time decisions during spectroscopy experiments and dynamically adjusting measurement choices for optimal information extraction. The simulator translates quantum phenomena into a classical and probabilistic framework. This implementation requires fast computations on the order of milliseconds.
Specific circumstances will require the use of purely quantum calculations, which were performed with the QuTiP library [48] and will serve as a preliminary step to quantitatively and qualitatively pre-calculate properties and quantities that will then be inserted

into the classical model.
Even though a classical probabilistic model lowers computational costs by optimizing efficiency, numerous limitations must be considered when evaluating the accuracy of the model. First, we assume that the quantum state of the molecule is a mixed state and lacks coherence. As a consequence, we simulate only populations, neglecting coherences and the possibility of generating superpositions from the molecule-laser interaction.
A statistical mixture of the states $|m\rangle$ in a given J has the following density matrix:

$$\rho_J = \frac{1}{2(2J+1)}\Bigg(\sum_{m=-J-1/2}^{J-1/2} |J,m,\xi=-\rangle\langle J,m,\xi=-| + \sum_{m=-J+1/2}^{J+1/2} |J,m,\xi=+\rangle\langle J,m,\xi=+|\Bigg). \tag{3.1}$$

The interpretation of the mixed state is that the molecule is in one of these states probabilistically, and only a measurement can determine which one.
On the other hand, a coherent superposition of the same states includes off-diagonal coherence terms, and the corresponding density matrix is:

$$\rho_J = \sum_{\xi,\xi'=\pm} \sum_{m\in M_\xi} \sum_{m'\in M_{\xi'}} C_{m,\xi} C^*_{m',\xi'} |m,\xi\rangle\langle m',\xi'| \tag{3.2}$$

with $M_{\xi=-} = \{-J-1/2,\dots,J-1/2\}$ and $M_{\xi=+} = \{-J+1/2,\dots,J+1/2\}$.
This assumption is likely justified because during the experiment the laser pulse interacts with the molecule multiple times, each with a time-dependent Rabi phase which is not phase-locked to the molecule.
Having this shot-to-shot randomization of the phase, any superposition would quickly dephase, thus decohering the coherent state into a mixed state.
This argument holds during the application of optical pumping, since the driving laser is continuously applied and has a finite coherence time and with the effect of dissipation via sideband cooling, results in a mixed state. It also holds when applying multiple subsequent measurements, where signature transitions are driven back and forth many times.
Another limitation of employing a classical probabilistic physics simulator lies in the method used to describe the interactions between molecular levels. As shown in Figure 3.6, in the $\sigma^- - \pi$ polarization configuration we are primarily considering, each man-

ifold is a multi-level system in which each state interacts according to the $\Delta m = \pm 1$ selection rules with the four adjacent states, in what we refer to as *direct coupling*. The motional adding-sideband transitions combined with motional dissipation via sympathetic cooling enforce a directionality to the interaction; therefore, each level actually couples to at most two other levels, neglecting *off-resonant coupling*. With $|J, m\rangle\,|n = 0\rangle \rightarrow |J, m-1\rangle$ being the intended transition, off-resonant coupling between $|J, m-1\rangle\,|n = 1\rangle \rightarrow |J, m-2\rangle\,|n = 2\rangle$ is also possible.

As a consequence, when computing the excitation probability induced by the laser interaction, one has to deal with a three-level system illustrated in Figure 3.7. In this configuration, the initial state $|a\rangle$ can undergo two different transitions to levels that are not coupled to each other by the Raman laser $|b\rangle$ and $|c\rangle$. We denote the two corresponding detunings Δ_{ab} and Δ_{ac}, and the respective Rabi frequencies by Ω_{ab} and Ω_{ac}. These differ because the same reduced Rabi frequency Ω is weighted by two different coupling coefficients c_{ab} and c_{ac}.

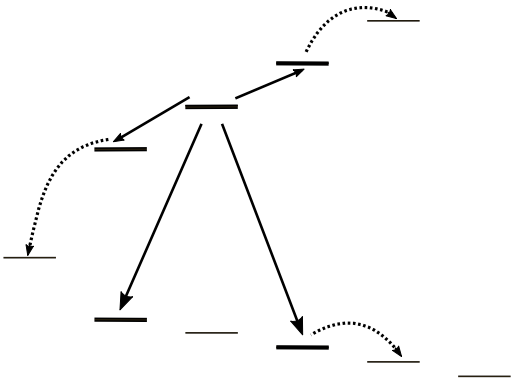

Figure 3.6: Schematic of the possible transitions (sideband transitions which are then cooled) a given state can undergo with the $\sigma^- - \pi$ two-beam Raman configuration: direct transitions to neighboring states with $\Delta m = \pm 1$ (solid arrows), and off-resonant transitions to more distant states (dashed arrows).

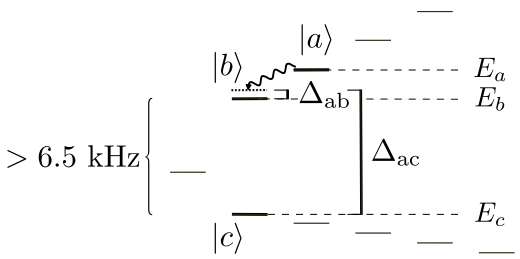

Figure 3.7: Vee linkage pattern for a three-level system. Laser pulse excites transitions from initial state $|a\rangle$ to final states $|b\rangle$ and $|c\rangle$, separated at least by 6.5 kHz.

Computing the excitation probabilities for this Vee system is only feasible numerically, as there is no closed-form expression analogous to (2.6) for a three-level system. In principle, given the time duration and Rabi frequency parameters of all pulses involved, it would be possible to pre-compute these probabilities. However, it is essential to retain flexibility regarding the type of pulse applied together with fast, real-time computations.

Fortunately, in our case the three-level system can be effectively reduced to a two-level system. In a generic Vee configuration, the two possible ending states $|b\rangle$ and $|c\rangle$ belong to different sub-manifolds: these exhibit their minimum energy separation at $m_F = -J + 1/2$ due to the structure of both molecules. This separation ranges from approximately 18.2 kHz ($J = 1$) to 106.0 kHz ($J = 14$) for $^{40}CaH^+$ at $B = 3.6$ G, and from 6.5 kHz ($J = 1$) to 61.5 kHz ($J = 50$) for $^{40}CaOH^+$ at $B = 3.27$ G. Consequently, the worst-case scenario for the approximation corresponds to a splitting of 6.5 kHz between states $|b\rangle$ and $|c\rangle$.

Therefore, in a three-level system, if the initial state is in resonance with one transition, it is off-resonant with the other by at least 6.5 kHz, making the corresponding excitation probability negligibly small. This is verified by considering the excitation dynamics which shows a range of characteristics based on how the detunings relate to the Rabi frequencies. In our case, however, the detuning is significantly larger than the Rabi frequencies. In this limit, only a negligible population accumulates in the off-resonant level, while the dynamics is reduced to an effective two-level transfer between the resonant states. By applying adiabatic elimination of the off-resonant state, the three-state system can therefore be simplified to a two-state description.

Using the set of differential equations (B.5) derived in Appendix B, we simulate the system population dynamics starting from an initial population entirely in state $|a\rangle$ with $\Delta_{\mathrm{ab}} = 50$ Hz and $\Delta_{\mathrm{ac}} = 6.5$ kHz. This corresponds to an on-resonance transition to level $|b\rangle$ and an off-resonance transition to level $|c\rangle$. We assume a reduced Rabi frequency of $\Omega_{\mathrm{Raman}} = 1$ kHz, with coupling coefficients $c_{ab} = c_{ac} = 0.1$ to represent the worst-case scenario. Hence, the effective Rabi frequencies are $\Omega_{\mathrm{ab}} = \Omega_{\mathrm{ac}} = 100$ Hz. The resulting population evolutions are shown in Figure 3.8a. It is noteworth that at least for the first oscillation period the population peaks of the two- and three- level approximations are overlapping, and negligible population occurs in state $|c\rangle$. This result justifies adiabatic elimination of state $|c\rangle$ from the equations of motion and, in conclusion, it is safe to treat the direct coupling of three-level systems with the approximation of two-level system.

Conversely, if one considers the case – which does not occur in our situation – where transition from level $|a\rangle$ is near resonance to both levels $|b\rangle$ and $|c\rangle$, this approximation is no longer valid. As shown in Figure 3.8b, for the case $\Delta_{ab} = 50$ Hz, $\Delta_{ac} = 100$ Hz and $\Omega_{ab} = \Omega_{ac} = 100$ Hz, the actual excitation dynamics exhibits a chaotic behavior, and the two-level approximation yields completely different results.

Moreover, in our system it may also occur that the transitions from level $|a\rangle$ to both $|b\rangle$ and $|c\rangle$ are off-resonance. In this case, as illustrated in Figure 3.8c, where $\Delta_{ab} = 2$ kHz, $\Delta_{ac} = 4.5$ kHz and $\Omega_{ab} = \Omega_{ac} = 100$ Hz, one can see that although the two-level approx-

imation again produces significantly different results, the population remains almost entirely in level $|a\rangle$. The excitation is so small that it can be considered negligible in both cases.

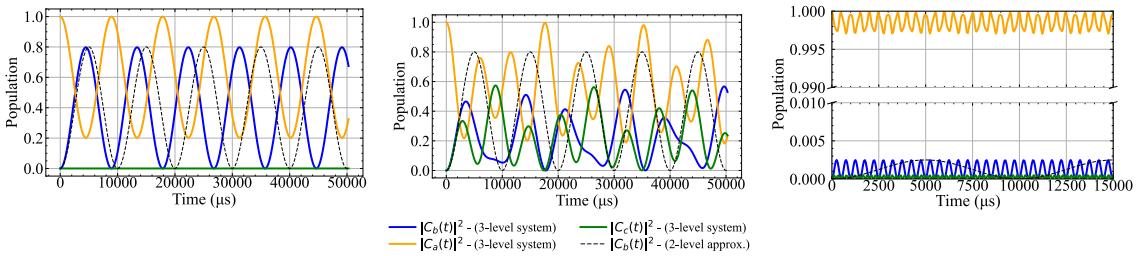

(a) Transition from state $|a\rangle$ to state $|b\rangle$ is on-resonance ($\Delta_{ab} = 50$ Hz), and to state $|c\rangle$ is off-resonance ($\Delta_{ac} = 6.5$ kHz).

(b) Transitions from state $|a\rangle$ to states $|b\rangle$ and $|c\rangle$ are on-resonance ($\Delta_{ab} = 50$ Hz and $\Delta_{ac} = 100$ Hz).

(c) Transitions from state $|a\rangle$ to states $|b\rangle$ and $|c\rangle$ are off-resonance ($\Delta_{ab} = 2$ kHz and $\Delta_{ac} = 4.5$ kHz).

Figure 3.8: Three-level system dynamics with population initialization in $|a\rangle$ and comparison with the two-level approximation. Different situations are analyzed, with $\Omega_{ab} = \Omega_{ac} = 100$ Hz. The black curve represents the population transfer between $|a\rangle$ and $|b\rangle$ under the two-level approximation, the green curve shows the corresponding dynamics using the full three-level description, and the orange curve illustrates the interaction between $|a\rangle$ and the off-resonant state $|c\rangle$ in the same three-level framework.

By applying adiabatic elimination, the two possible transitions originating from a given level are considered as *mutually exclusive events* – since at most one of them can occur – rather than as *independent events*, which would instead allow for the possibility that both transitions take place.
As a final consideration, off-resonant coupling to more distant states is another phenomenon that arises in the description of a multi-level mechanical system. As illustrated in Figure 3.6, off-resonant coupling occurs when residual coupling occurs prior to the motional excitation being cooled away: as a consequence, the initial state is coupled to the neighboring state but residual population is mapped to more distant states. The effect of off-resonant coupling depends on the pulse duration and the Rabi frequencies, Raman detunings and cooling rates, and it will be analyzed in more detail in the following Chapter, with particular attention to the limitations of the current classical model and to the Rabi frequency regimes in which off-resonant coupling can be safely neglected.

Within all these approximations, the physical model simulates the behaviour of a general linear molecular ion with nuclear spin 1/2 in its $^1\Sigma$ ground state, in the presence of an external magnetic field B. It takes as input the molecular parameters of the Hamiltonian of Eq. (2.19), as well as those necessary to describe the interaction with the laser

field: the g-factor for rotation g_J, the rotation-nuclear spin coupling c_{IJ}, the rotational constant B_R, the external magnetic field strength B, the temperature T, the frequency of the Raman beam ω_R, and the frequency of the electronic transition between the ground and first excited states ω_e. Moreover the manifolds of the molecules are simulated up to a final rotational state $J_{\max}$, where its occupational population starts to be negligible: as illustrated in Figure 3.3, a $J_{\max} = 14$ is chosen for $^{40}CaH^+$ and $J_{\max} = 50$ for $^{40}CaOH^+$. Using these input parameters, the main information of the molecules is reported in two dataframes. The states dataframe, `state_df`, includes the state quantum numbers, spin-up and spin-down amplitude components, and rotational and hyperfine energies. Moreover, the information regarding all possible transitions, schematized as two-level system transitions between adjacent states $|a\rangle$ and $|b\rangle$, following the approximations described above, is reported in the dataframe `transition_df`. This dataframe contains the following parameters: the manifold J, the initial and final quantum number m_F and ξ, the energy difference between the states ΔE_{ab} and the coupling coefficient of the transition c_{ab}.

The state distribution $\vec{\pi}$ of the linear molecular ion is then computed. In the thermal equilibrium at blackbody temperature T, the rotational states are occupied with probability P_J as defined in Eq. (2.32), whereas all the states belonging to the manifold are equally populated with probability:

$$\pi_{J,m_F,\xi} = \frac{P_J}{2(2J+1)} \tag{3.3}$$

in such a way that $\sum_{J,m_F,\xi} \pi_{J,m_F,\xi} = \|\vec{\pi}\|_1 = 1$.

To obtain the molecular spectrum, the excitation probability of each state is evaluated. For a given state $|a\rangle$, the contributions from the two possible transitions are summed, consistent with the mutually exclusive event definition:

$$p_a^{\text{exc}}(\nu;\Theta) = \sum_b p_{ab}^{\text{exc}}(\nu;\Theta) \tag{3.4}$$

where the transition probabilities depend on the laser detuning ν and other laser parameters Θ (pulse duration, Rabi frequency, and experimental imperfections). It is important to ensure that $p_a^{\text{exc}}(\nu;\Theta) \leq 1 \quad \forall a$: this condition is naturally satisfied due to the adiabatic elimination approximation and the use of sufficiently small Rabi frequencies. Collecting these values for all states defines the excitation probability vector $\vec{p}^{\text{exc}}(\nu;\Theta)$.

Finally, the spectrum is computed as:

$$S(\nu;\Theta) = \vec{\pi} \cdot \vec{p}^{\,\mathrm{exc}}(\nu;\Theta) \tag{3.5}$$

scanning over the detuning ν.

3.3 Spectrum of the molecular Hamiltonian

After studying the energy level structures of both molecular ions, we proceed to simulate and compute the spectrum of the molecular Hamiltonian.
The hyperfine spectrum of the $^{40}CaH^+$ cation has already been experimentally obtained [9]: for this reason, we apply the *physics simulator* as previously described in order to reproduce the known experimental spectrum, using it as a validation benchmark before extending the model to the $^{40}CaOH^+$ molecule whose spectrum has not yet been experimentally measured.
Experimental imperfections are considered for both molecules, as motivated by the discussion in Chapter 2. The exact magnitudes of these imperfections are unknown, but educated guesses can be chosen to capture the correct scale:

1. **Miscalibration**: constant deviations throughout the entire simulation, representing systematic offsets in the experimental setup. Each parameter is randomly drawn once from a Gaussian distribution at the beginning of the simulation:
   (a) **Frequency**: Gaussian fluctuations with standard deviation $\sigma = 50\,\mathrm{Hz}$, accounting for uncertainties in the trap frequency and Raman detuning miscalibration,
   (b) **Reduced Rabi frequency**: Gaussian fluctuations with standard deviation $\sigma = 10\%$ of the nominal value, representing laser power miscalibration.

2. **Shot-to-shot fluctuations**: stochastic variations applied independently at each pulse, capturing the experimental instability in time-dependent parameters. For each laser pulse, the parameter value is drawn from a Gaussian distribution:
   (a) **Frequency**: Gaussian fluctuations with $\sigma = 30\,\mathrm{Hz}$, arising from trap frequency drifts, magnetic field fluctuations, and AOM instability,
   (b) **Reduced Rabi frequency**: Gaussian fluctuations with $\sigma = 1\%$ of the nominal value, reflecting laser amplitude instability.

In addition, a false positive detection rate of 1.5% has been included to account for spurious excitations caused by motional heating.
For the $^{40}CaH^+$ molecule, the calculations were performed considering a magnetic field strength of $B = 3.6\,\mathrm{G}$ (intermediate regime), and simulating its levels up to and including the $J = 14$ manifold. The temperature is set to $T = 300\,\mathrm{K}$, while the laser drives $\Delta m = -1$ blue-sideband transitions with $t = 1000\,\mu\mathrm{s}$ pulses having a reduced Rabi frequency $\Omega_{\mathrm{Raman}} = 5\,\mathrm{kHz}$. The simulated Raman spectra for $^{40}CaH^+$, probed with 500 scan points, with and without the experimental imperfections are shown in Figure 3.9a.
The frequency axis is shifted by the offset value of the motional frequency. The $^{40}CaH^+$ spectrum shows two significant peaks around $\nu_1 \simeq -2\,\mathrm{kHz}$ and $\nu_2 \simeq -6\,\mathrm{kHz}$, as expected. Indeed, the nearly-degenerate transitions between non-stretched states in the lower $\xi = +$ sub-manifolds have an energy spacing of approximately $-2\,\mathrm{kHz}$ ($\Delta m = -1$), while those in the upper $\xi = -$ sub-manifolds are spaced by roughly $-6\,\mathrm{kHz}$. The contributions relative to all these transitions at similar frequencies ($-2\,\mathrm{kHz}$ and $-6\,\mathrm{kHz}$) sum up, thus creating the two peaks. This symmetry structure is truly beneficial for the purpose of the state preparation protocol: it allows to develop a general optical pumping scheme that is nearly resonant for a multitude of transitions simultaneously.
Considering the $^{40}CaOH^+$ molecule, a magnetic field strength of $B = 3.27\,\mathrm{G}$ is taken into account (intermediate regime), simulating up to and including the $J = 50$ manifold. At room temperature $T = 300\,\mathrm{K}$, the laser drives $\Delta m = -1$ blue-sideband transitions with $t = 5000\,\mu\mathrm{s}$ pulses having a reduced Rabi frequency $\Omega_{\mathrm{Raman}} = 0.796\,\mathrm{kHz}$. The reduced Rabi frequency is decreased to distinguish and resolve nearby peaks, while the pulse duration increased to keep the pulse area approximately constant. The $^{40}CaOH^+$ simulated Raman spectra with and without the experimental imperfections, probed with 400 scan points, are depicted in Figure 3.9b.
A similar symmetry of the level structure still holds, and, in this case, the two peaks corresponding to the multiple transitions between neighboring states in the two sub-manifolds are around $\nu_1 \simeq -0.35\,\mathrm{kHz}$ for the upper sub-manifold $\xi = -$, and $\nu_2 \simeq 0.15\,\mathrm{kHz}$ for the lower sub-manifold $\xi = +$. Note that the lower sub-manifold $\xi = +$ has opposite slope in energy with m_F as compared to $^{40}CaH^+$.

In general, in the intermediate regime the signature transitions are J-dependent and depicted by the red columns in Figures 3.9a and 3.9b. The scope of the state preparation protocol is to identify in which rotational level J the molecule is by making use of these J-dependent signature transitions. However the excitation probabilities associated to the signature transitions are small: this is explained by the fact that the population P_J relative to the rotational manifold J is equally distributed between the $2 \cdot (2J + 1)$ levels

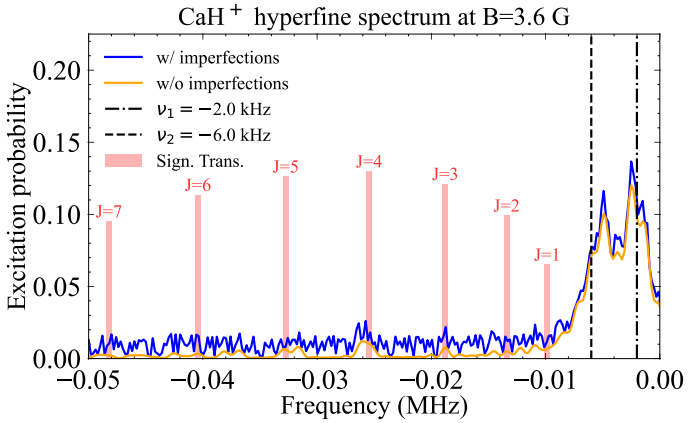

(a) At $B = 3.6$ G, the $\Delta m = -1$ simulated spectrum with $t = 1$ ms pulses, 500 scan points, and reduced Rabi frequency $\Omega_{\text{Raman}} = 5$ kHz.

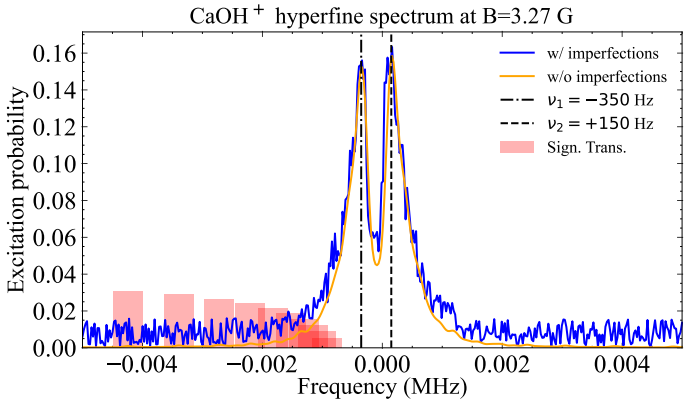

(b) At $B = 3.27$ G, the $\Delta m = -1$ simulated spectrum with $t = 5$ ms pulses, 400 scan points, and reduced Rabi frequency $\Omega_{\text{Raman}} = 0.796$ kHz.

Figure 3.9: Hyperfine Raman spectra for $^{40}CaH^+$ (top) and $^{40}CaOH^+$ (bottom) molecular ions at $T = 300$ K, with and without experimental imperfections.

of the manifold, hiding the signature transition signal.

Furthermore, the signature transition peaks for $^{40}CaOH^+$ are weaker compared to those of $^{40}CaH^+$, since the population is distributed over a larger number of rotational manifolds which reduces the occupation probability of each individual state. In addition, the signature transition frequencies for $^{40}CaOH^+$ exhibit a stronger overlap, being located near the hyperfine peaks and close to the zero-frequency region due to the fact that the first rotational manifolds lie in the Zeeman regime.

Moreover, comparing the two spectra, we notice that in $^{40}CaOH^+$ the hyperfine peaks are shifted closer to the zero point frequency as well.

In any case, the physics simulator provides a molecular spectrum of $^{40}CaH^+$ that closely

resembles the experimental one [9]. This agreement corroborates and validates the underlying model, supporting its application to the $^{40}CaOH^{+}$ molecule. One relevant physical effect not included in the simulated spectrum is the optical dipole force (ODF), which gives rise to a peak around the frequency $\nu - \nu_t = 0$, as discussed in the Theory Section 2 and further addressed in the following Section.

3.4 Optical dipole force (ODF)

The optical dipole force (ODF) arises when the polarizations of the σ and π beams are not perfectly orthogonal, and when the magnetic field axis is not perfectly collinear with the sigma beam k-vector and π beam polarization vector. In such cases, each beam contains a fraction of the same polarization, which in turn drives a coherent excitation of the motional degree of freedom due to the frequency difference between the beams matching the motional frequency. As a consequence, the molecular motional state is displaced from the ground state into a coherent state. This effect can be described by a Hamiltonian whose time evolution essentially corresponds to a displacement operator with Rabi frequency Ω_{ODF} (as defined in (2.40)), which adds to the blue-sideband Hamiltonian governing the molecular transition.
The system is simulated using QuTiP and consists of three components. First, the molecular part is modeled as a three-level system. A single blue-sideband transition at frequency ω_{mol} is included between two of the levels at Rabi frequency Ω_{mol}, while the third level remains unaffected by the transition and is used to account for a non-unitary population distribution. Second, the motional degree of freedom is represented by a truncated Fock space with N levels. Finally, the ion is described as a two-level system that undergoes the red-sideband readout of the molecular BSB transition, as well as the action of the ODF.
The experimental data of the ODF due to the Raman beams interacting with the calcium atom are shown in Figure 3.10, together with simulation results obtained for 1 ms pulses, $\Omega_{\mathrm{ODF}} = 1.676\,\mathrm{kHz}$, and an initial motional coherent state with displacement eigenvalue $\alpha = 0.2$.

The RSB atomic readout signal resembles a sinc^2 function, with the presence of periodic relative minima and maxima. Moreover, the displacement in the phase space of the initial coherent state produces background noise at the level of few percent far from the zero-frequency region, while the principal peak is contained in the frequency range $[-1; +1]\,\mathrm{kHz}$.

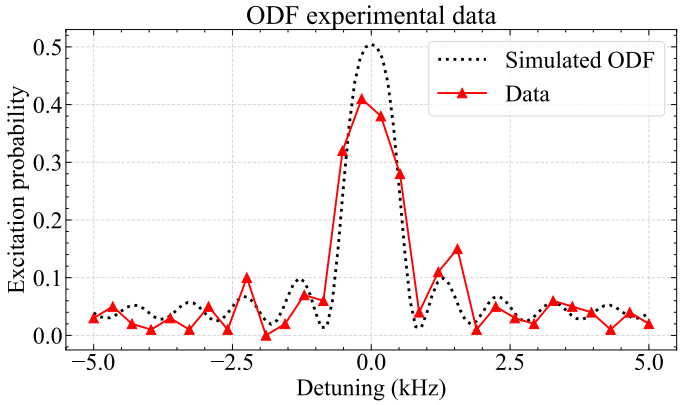

Figure 3.10: ODF experimental data (red line), and simulated data (black line) with 1 ms pulses, $\Omega_{\mathrm{ODF}} = 1.676\,\mathrm{kHz}$ and an initial coherent motional state $|\alpha = 0.2\rangle$.

Taking into account the differences in their rotational and nuclear spin parameters, the $^{40}CaH^+$ and $^{40}CaOH^+$ molecules experience different consequences in the presence of an ODF. In particular, it has been observed that the principal peaks of the $^{40}CaH^+$ hyperfine spectrum are located near $\sim -2\,\mathrm{kHz}$ and $\sim -6\,\mathrm{kHz}$, perfectly visible despite the presence of the ODF mechanism. Conversely, the $^{40}CaOH^+$ molecule possesses the hyperfine peaks at frequencies much closer to the zero-frequency region, around $\sim -350\,\mathrm{Hz}$ and $\sim 150\,\mathrm{Hz}$; as a consequence, those peaks are completely hidden under the ODF signal making it highly complicated to experimentally obtain the hyperfine spectrum signal with a good signal-to-noise ratio.

For this reason, the goal is to simulate a realistic peak of the actual $^{40}CaOH^+$ BSB transition in the presence of the ODF. In order to simplify the multi-level system of the molecule, only the most significant molecular transition frequency is considered, that is the frequency of one of the two peaks of the $^{40}CaOH^+$ hyperfine spectrum.

I considered the left peak at $\nu_1 \simeq -350\,\mathrm{Hz}$, $\Omega_{\mathrm{mol}} = \frac{\pi}{1\,\mathrm{ms}} = 3.14\,\mathrm{kHz}$, and simulated the atomic readout of the blue-sideband transition with and without the presence of the ODF at various magnetic fields. The signals for $B = 3.27\,\mathrm{G}$ (intermediate regime) are shown in Figure 3.11a: the BSB transition without the ODF is completely covered by the ODF signal, and the combined action of the BSB transition and the ODF produces a curve almost equivalent to the ODF signal alone. These results are certainly even worse for the right peak at $\nu_2 \simeq 150\,\mathrm{Hz}$.

A possible strategy to increase the SNR of the molecular hyperfine transition through the frequency-dependent false-positives produced by the ODF would be to increase the magnetic field strength with the aim to push the two hyperfine peaks away from the zero-frequency region. At $B = 10\,\mathrm{G}$, the left peak is shifted to $\nu_1 \simeq -815\,\mathrm{Hz}$, while at

$B = 50\,\mathrm{G}$ to $\nu_1 \simeq -2.110\,\mathrm{kHz}$. The simulation results for these magnetic field values are displayed in Figures 3.11b and 3.11c, respectively. As the peak of the molecular transition shifts further to the left, it becomes more visible, and only around $B = 50\,\mathrm{G}$ does the molecular signal become clearly distinguishable from the ODF peak. However, obtaining such a high magnetic field intensity experimentally is difficult.
Alternatively, the polarization purity of the beams can be improved. Taking into account the current values used in the simulation, we obtain the fraction $\frac{\Omega_{\mathrm{ODF}}}{\Omega_{\mathrm{mol}}} = \frac{1.676}{3.14} \simeq 0.53$ between the Rabi frequency of the transition with correct polarization and the transition with incorrect polarization. By reducing the wrong polarization fraction by a factor of 10, with $\Omega_{\mathrm{ODF}} = 0.168\,\mathrm{kHz}$, the ODF peak would be significantly reduced. The results varying the magnetic field intensity ($B = 3.27\,\mathrm{G}$, $B = 10\,\mathrm{G}$, $B = 50\,\mathrm{G}$) are shown in Figures 3.11d, 3.11e and 3.11f.

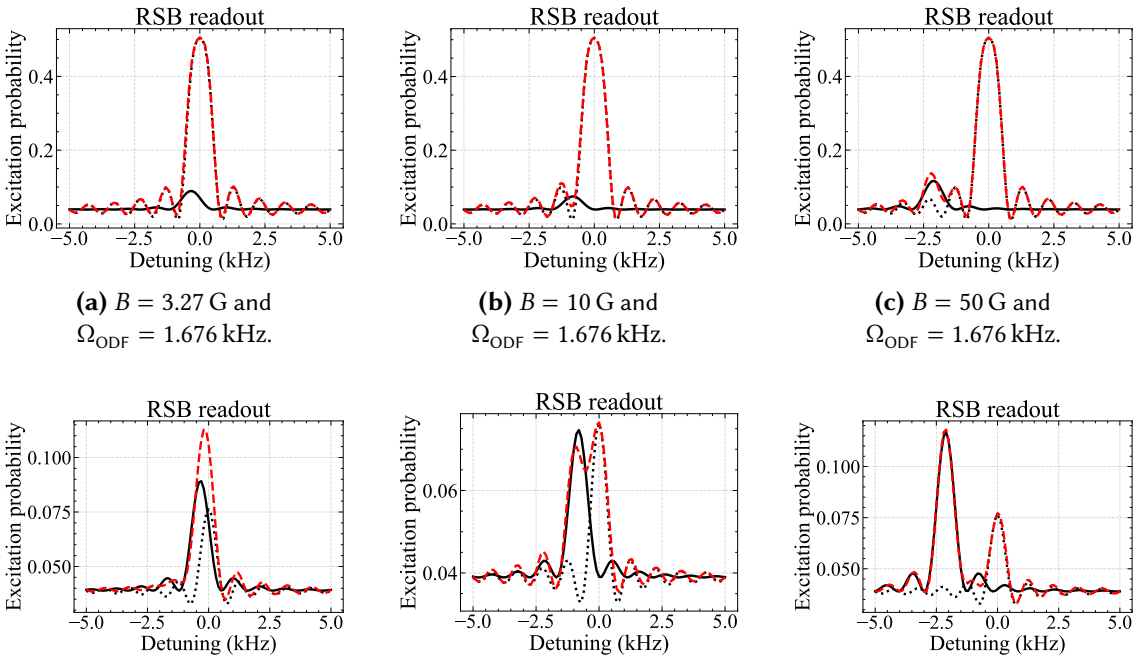

(a) $B = 3.27\,\mathrm{G}$ and $\Omega_{\mathrm{ODF}} = 1.676\,\mathrm{kHz}$.

(b) $B = 10\,\mathrm{G}$ and $\Omega_{\mathrm{ODF}} = 1.676\,\mathrm{kHz}$.

(c) $B = 50\,\mathrm{G}$ and $\Omega_{\mathrm{ODF}} = 1.676\,\mathrm{kHz}$.

(d) $B = 3.27\,\mathrm{G}$ and $\Omega_{\mathrm{ODF}} = 0.168\,\mathrm{kHz}$.

(e) $B = 10\,\mathrm{G}$ and $\Omega_{\mathrm{ODF}} = 0.168\,\mathrm{kHz}$.

(f) $B = 50\,\mathrm{G}$ and $\Omega_{\mathrm{ODF}} = 0.168\,\mathrm{kHz}$.

Figure 3.11: For $^{40}CaOH^+$, ODF simulations (dashed black line) and comparison with a BSB transition, shown both in the presence (dashed red line) and absence (black solid line) of the ODF. The analysis considers $\Omega_{\mathrm{mol}} = 3.14\,\mathrm{kHz}$, exploring different values of magnetic field B and ODF strength Ω_{ODF}.

With $\Omega_{\mathrm{ODF}} = 0.168\,\mathrm{kHz}$, already at $B = 10\,\mathrm{G}$ the peak of the molecular transition is visible and separated from the peak due to the ODF. However, further optimizing the polarization of the laser beams with respect to the current values and maintaining its stability keeping it stable ultimately requires interferometric stability, both in path

length and polarization drifts from temperature drifts.
For this reason, a different strategy has been implemented to circumvent the presence of the ODF and make the two hyperfine peaks of the $^{40}CaOH^{+}$ molecule visible, even at intermediate magnetic field strenghts.

3.4.1 Loop closing strategy

The ODF produces a motional state displacement in phase space, following the displacement operator defined in Eq. (2.45), which possesses a radius and an angular velocity dependent on the Rabi frequency Ω_{ODF} and on the frequency detuning δ.
As a consequence, in order to suppress the motional excitation from the ODF, a new method was implemented involving the closing of the loops from the ODF in the phase space.
This strategy includes the application of a variable pulse duration, dependent on the frequency detuning:

$$T = N \cdot \frac{2\pi}{\delta} \tag{3.6}$$

where N is the number of closed loops in the phase space and δ the frequency detuning in the x-axis. Thus, applying a δ-dependent pulse duration should suppress motional excitation from the ODF.
The radius of the loops created in the phase space are δ-dependent as well: as δ decreases, the radius increases, and consequently it takes longer to close the loop. For this reason, the number of loops N is progressively decreased as we approach the zero-frequency region: from $N = 4$ at large detunings to $N = 1$ at small detunings. Moreover, in order to avoid excessively long pulse durations near the zero-frequency region, taking into account a heating rate of 1 phonon/second, this strategy is applied with a maximum pulse duration of $T = 15\,\mathrm{ms}$.
Finally, the presence of a variable pulse duration means that the Rabi frequency of the molecular transition no longer corresponds to the π-time. To restore pointwise this property, a T-dependent (and therefore δ-dependent) Rabi frequency of the molecular transition is also chosen:

$$\Omega_{\mathrm{mol}} = \frac{\pi}{T} = \frac{\delta}{2}. \tag{3.7}$$

Applying this strategy at $B = 3.27\,\mathrm{G}$ to the left hyperfine peak at frequency $\nu_1 \simeq -350\,\mathrm{Hz}$, with Rabi frequency $\Omega_{\mathrm{ODF}} = 1.676\,\mathrm{kHz}$ to fit the experimental data, we obtain the sim-

ulated RSB readout shown in Figure 3.12.
In the simulations, the motional excitation from the ODF peak is successfully suppressed, except for the zero-frequency region where the maximum pulse duration $T = 15\,\text{ms}$ is reached. The BSB transition is driven without the presence of oscillations thanks to the variable Rabi frequency of the molecule.
By comparing the results with the detection signal in Figure 3.11a, where the ODF completely obscures the molecular transition, we are able to theoretically demonstrate this strategy.

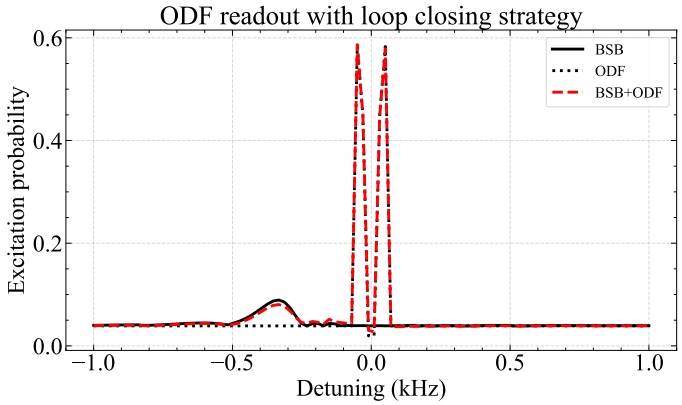

Figure 3.12: Blue-sideband transition of the left hyperfine peak at $\nu = -350\,\text{Hz}$ with and without the ODF, using the loop closing strategy. Here we consider $B = 3.27\,\text{G}$ and a Rabi frequency $\Omega_{\text{ODF}} = 1.676\,\text{kHz}$.

4

State preparation

After simulating the hyperfine spectra of the molecular ions $^{40}CaH^+$ and $^{40}CaOH^+$, and having validated the model by obtaining results for $^{40}CaH^+$ in agreement with experimental data [9], we proceed to develop a protocol for preparing the molecule in a pure initial state and subsequently identifying it. This protocol is designed to be general and flexible, allowing its application to other linear molecular ions with nuclear spin 1/2 while relying on an off-resonant laser source to drive Raman transitions is not specific to the molecular species.
In particular, each manifold J has a thermal population distributed equally among the states within the manifold. This population must be concentrated to a target state $|\mathcal{T}_J\rangle$. This procedure enhances the signal-to-noise ratio (SNR) associated with the J-dependent signature transitions.
In this Chapter we introduce a two-stage state preparation scheme. In the first stage, optical pumping is applied to concentrate the population of each manifold into a limited subset of states. In the second stage, rapid adiabatic passage is employed to transfer the population from these subsets to the target state. In the final part, the spectrum after the state preparation is simulated.

4.1 Optical pumping

Optical pumping involves the use of the same 1051 nm blue-sideband Raman transitions previously employed for quantum logic spectroscopy. Instead of performing multiple individual pulses, the beams continuously drive the system to converge from an initial configuration to one in which the dark state is created. Since blue-sideband transitions produce motional excitation, in order to induce directionality in the Raman transitions, and hence pump, optical pumping must be accompanied by controlled dissipation: for this reason, the molecule's motion is sympathetically cooled by the co-trapped atomic

ion which undergoes sideband cooling. In fact, since the motion of the molecular ion and atomic ion is shared, cooling the atom with a certain cooling rate Γ_{cooling} also cools the molecule. For efficient pumping, we need to ensure that in the presence of heating at rate Γ_{heating}, that $\Gamma_{\text{cooling}} > \Gamma_{\text{heating}}$.
To simulate the optical pumping mechanism on a manifold J, for the Raman sideband interaction we construct the relative time-dependent Hamiltonian as the sum of the contributions from all possible single 2-level transitions at $\Delta m = \pm 1$ (following considerations of the previous Chapter, neglecting off-resonant coupling):

$$\hat{H}_J^{\text{BSB}}(\Lambda; t) = \sum_i \hat{H}_i^{\text{BSB}}(\Lambda, \Phi_i; t) \tag{4.1}$$

where Λ represents the global parameters that include the Raman detuning ω_{Raman} and reduced Rabi frequency Ω_{Raman}, while Φ_i denotes the local parameters relative to the i-th transition, i.e., the coupling coefficient c_{ab} and the molecular transition frequency ω_{mol}. The Hamiltonian $\hat{H}_i^{\text{BSB}}(\Lambda, \Phi_i; t)$ relative to the single i-th transition follows Eq. (2.18) and has dimension:

$$\dim(\hat{H}_i^{\text{BSB}}) = n_{\text{internal}} \cdot n_{\text{motional}} \tag{4.2}$$

where n_{internal} is the number of states contained in the manifold and n_{motional} the number of simulated motional levels. As a consequence, $\dim(\hat{H}_J^{\text{BSB}}) = \dim(\hat{H}_i^{\text{BSB}})$.
We build the density matrix as the tensor product between a mixed state for the internal state space, and the ground state for the motional state space:

$$\hat{\rho}_0 = \hat{\rho}_{\text{internal}} \otimes \hat{\rho}_{\text{mot}} = \frac{1}{n_{\text{internal}}} \hat{\mathbb{I}}_{n_{\text{internal}}} \otimes |0\rangle \langle 0| . \tag{4.3}$$

We use the Lindblad master equation to evolve this density matrix with the Hamiltonian of Eq. (4.1) and the following collapse operator describing the dissipation of the cooling process:

$$\hat{L} = \sqrt{\Gamma_{\text{cooling}}}\, \hat{\mathbb{I}}_{\text{internal}} \otimes \hat{a}, \tag{4.4}$$

where $\hat{\mathbb{I}}_{\text{internal}}$ is the identity operator in the internal space, $\hat{a}$ the lowering operator in the motional space, and Γ_{cooling} the cooling rate.
In this way, we obtain the final density matrix $\hat{\rho}_f$ at final time t_f. In order to extract the values of the state populations and the average phonon number, we build the following

operators:

$$\hat{N} = \hat{\mathbb{I}}_{\text{internal}} \otimes \hat{n}, \tag{4.5}$$

$$\hat{P}_j = (|j\rangle\langle j|) \otimes \hat{\mathbb{I}}_{\text{motional}}, \tag{4.6}$$

where $\hat{n}$ is the number operator on the motional Fock space while $|j\rangle$ represents the j-th internal state, and we apply them to the final density matrix obtaining the following expectation values:

$$\bar{n} = \langle \hat{n} \rangle = \text{Tr}\left[\hat{\rho}_f \hat{N}\right] \tag{4.7}$$

$$p_j = \langle \hat{P}_j \rangle = \text{Tr}\left[\hat{\rho}_f \hat{P}_j\right]. \tag{4.8}$$

The hyperfine spectra of the molecules exhibit two peaks, at frequencies ν_1 (corresponding to the upper sub-manifolds) and ν_2 (corresponding to the lower sub-manifolds), which arise from the overlap of contributions from all transitions between the manifolds occurring at similar frequencies.
Consequently, in order to pump the entire population of a manifold into its target state, the leftmost (LM) state, we implement a two-stage optical pumping scheme illustrated in Figure 4.1. In the first stage, two Raman beams derived from the same laser source, with frequency difference ν_1 and wave-vector difference aligned along the motional axis, are applied at $\Delta m = -1$ to drive the population of the upper sub-manifold toward the left. In the second stage, the Raman detuning is changed to ν_2 at $\Delta m = -1$ to similarly pump the population of the lower sub-manifold toward the left.

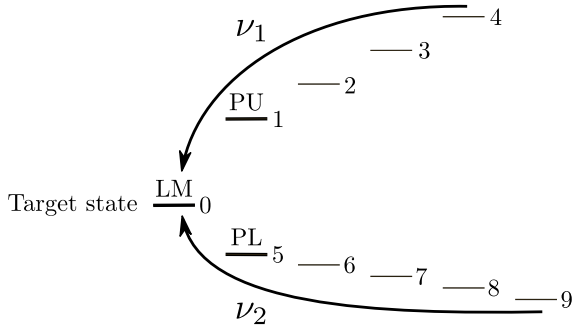

Figure 4.1: Two-stage optical pumping scheme with frequency ν_1 and ν_2 which transfers the population to the leftmost states; the leftmost state (LM, i.e., the target state), penultimate upper state (PU), and penultimate lower state (PL).

The laser acts simultaneously on all manifolds, redistributing the initially equally

populated states within each manifold. We thus expect to reach a situation in which the most populated states are the leftmost (LM), the penultimate upper (PU), and the penultimate lower (PL) states. In principle, the population in the PU and PL states is only partially transferred to the LM state, depending on the frequency difference between the states (i.e., the magnetic field regime and the specific manifold J considered) and on the Rabi frequency.

We now simulate the optical pumping scheme to the $^{40}CaH^{+}$ molecule at $B = 3.6\,\mathrm{G}$. Initially, each manifold is prepared in a completely mixed hyperfine state and in the motional ground state, as defined in Eq. (4.3). A 50 ms blue-sideband pulse is then simulated to drive $\Delta m = -1$ transitions. The frequency detuning between the two Raman beams is set to $\omega_{\mathrm{Raman}} = -2\,\mathrm{kHz}$, while the reduced Rabi frequency is chosen to be equal to the cooling rate, $\Omega_{\mathrm{Raman}} = \Gamma_{\mathrm{cooling}} = 10\,\mathrm{kHz}$. In the second step of the optical pumping sequence, the same laser is applied with the frequency detuning shifted to $\omega_{\mathrm{Raman}} = -6\,\mathrm{kHz}$. In this way, the population of each manifold is progressively pumped toward the leftmost states. The results of the two optical pumping stages for the manifold $J = 8$ are presented in Figure 4.2. This figure shows the time evolution of the population among the internal levels, which are indexed according to the scheme illustrated in Figure 4.1.

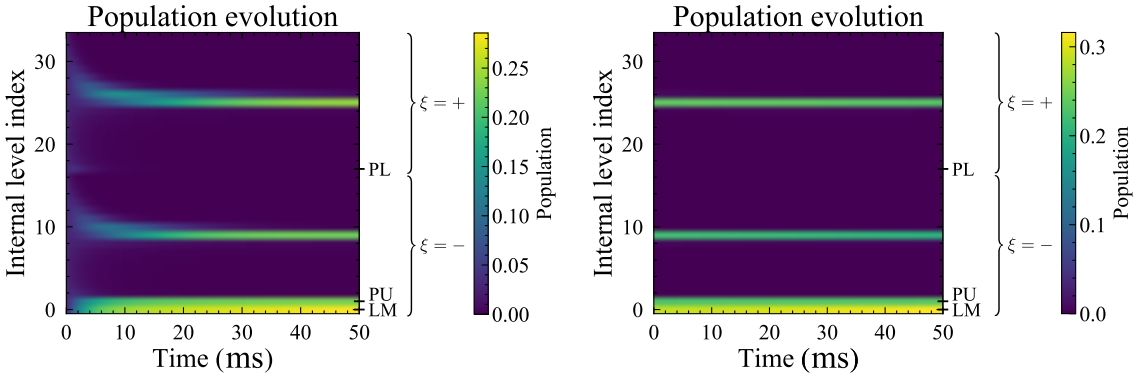

Figure 4.2: Simulation of the two-stage optical pumping scheme applied on the $J = 8$ manifold of the $^{40}CaH^{+}$ molecule at $B = 3.6\,\mathrm{G}$. The population evolution is displayed over time with $t = 50\,\mathrm{ms}$ pulses at $\nu_1 = -2\,\mathrm{kHz}$ (left) and at $\nu_2 = -6\,\mathrm{kHz}$ (right).

Already after the first pumping step at ν_1, also the population of the upper sub-manifold is driven toward the left. This occurs because the transitions within the upper sub-manifold are off-resonant by approximately 4 kHz, which is smaller than the reduced Rabi frequency of 10 kHz. Nevertheless, the second optical pumping step at ν_2 is performed to ensure that any residual population in the upper sub-manifold is also

transferred leftward. As a result, the population of the target state increases and a dark state is reached.
In this dark state, the population is efficiently pumped into the target state, which becomes the most populated; however, a significant fraction of the population remains trapped in the middle of each sub-manifold, in the region where $m_F \simeq 0$. This behavior is consistently observed across most of the simulated manifolds of the molecule. In addition, a residual population persists in the penultimate upper (PU) state. This is due to the fact that the $J = 8$ signature transition frequency is $-58.57\,\mathrm{kHz}$, which is much larger than the off-resonant Raman detunings applied at $-2\,\mathrm{kHz}$ and $-6\,\mathrm{kHz}$. Such behavior depends on the manifold under consideration and on its corresponding signature transition. Finally, the population of the penultimate lower (PL) state is fully transferred to the LM state, since the frequency difference of this transition is $-2.25\,\mathrm{kHz}$, which is smaller than the reduced Raman Rabi frequency. This effect also depends on the specific manifold and its corresponding LM $\leftrightarrow$ PL transition.

We now turn to the discussion of optical pumping in the $^{40}CaOH^+$ molecule. In this case, the two frequencies of the hyperfine spectrum are $\nu_1 \simeq -350\,\mathrm{Hz}$ and $\nu_2 \simeq 150\,\mathrm{Hz}$. Initially, each manifold is prepared in a completely mixed state, and a blue-sideband pulse of duration $t = 50\,\mathrm{ms}$ at $\Delta m = -1$ is simulated, with a Raman detuning from the blue-sideband frequency of $\omega_{\mathrm{Raman}} = -350\,\mathrm{Hz}$ and reduced Rabi frequency $\Omega_{\mathrm{Raman}} = \Gamma_{\mathrm{cooling}} = 5\,\mathrm{kHz}$. Subsequently, the same laser beams are applied with only the detuning from the blue-sideband frequency changed to $\omega_{\mathrm{Raman}} = 150\,\mathrm{Hz}$. The results of the two steps of simulated optical pumping for the manifold $J = 8$ are shown in Figure 4.3.

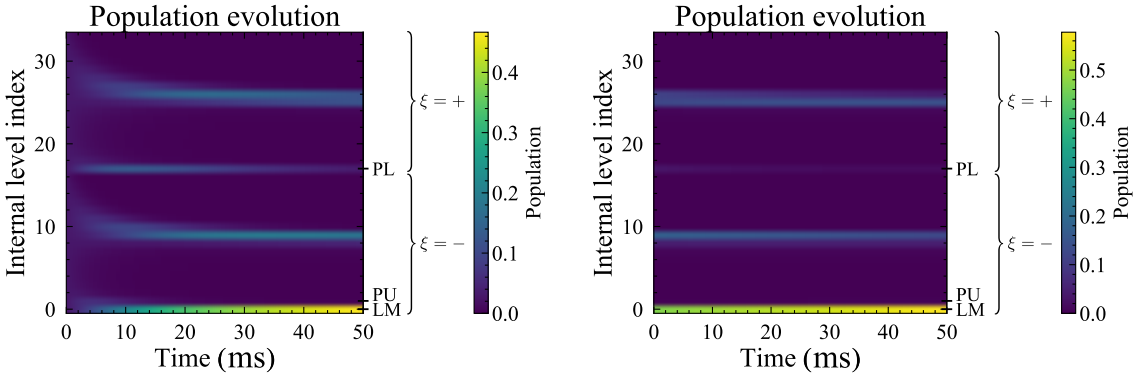

Figure 4.3: Simulation of the two-stage optical pumping scheme applied on the $J = 8$ manifold of the $^{40}CaOH^+$ molecule at $B = 3.27\,\mathrm{G}$. The population evolution is displayed over time with $t = 50\,\mathrm{ms}$ pulses at $\nu_1 = -350\,\mathrm{Hz}$ (left) and at $\nu_2 = 150\,\mathrm{Hz}$ (right).

As in the previous case, already the first optical pumping step at ν_1 successfully transfers

the population of the lower manifold to the target state. This occurs because the transitions within the lower sub-manifold are only slightly off-resonant, by approximately 500 Hz, which is considerably smaller than the reduced Rabi frequency. Nevertheless, the second pumping step at ν_2 is performed, as it contributes to an additional $\sim 10\%$ increase of the total population in the manifold in the target state. Overall, the population is efficiently pumped into the target state $|\mathcal{T}_8\rangle$, reaching a population of 60%.
In contrast to the previous case, the populations of the PU and PL states are transferred to the LM state. However, as before, a significant fraction of the population remains trapped in the middle of each sub-manifold, in the region where $m_F \simeq 0$. This prevents the complete transfer of population into the target state of each manifold and is consistently observed across all other simulated manifolds of the molecule.

In general, this pumping scheme operates as expected, demonstrating its applicability to two different molecular species. The population is effectively transferred to the target state, enabling the acquisition of the pumped spectrum by driving the signature transitions. However, particularly in the case of $CaOH^+$, where the number of available rotational states is large, improving the population transfer is necessary to achieve a good signal-to-noise ratio. This can be accomplished with an improved pumping scheme that introduces a third Raman branch to remove the population trapped in the middle of each sub-manifold.

4.1.1 Three-branch pumping scheme

Population is trapped in the middle of each sub-manifold when employing Raman beams with σ^- and π polarizations that drive a Raman transition between two molecular levels with $\Delta m = \pm 1$. Using this two-branch $\sigma^-\pi$ configuration we can calculate the coupling coefficients between molecular levels: for a fixed manifold J, we are specifically interested in the values of the coupling coefficients connecting the states that belong to the same sub-manifold. These transitions are highlighted in Figure 4.1.
Optical pumping can also be performed using Raman beams with different polarizations. In particular, in the experimental setup we implement a third branch of the same laser beam, with σ^+ polarization and a distinct wave-vector $\mathbf{k}$ such that the wave-vector difference with the σ^- beam lies along the motional axis. In this way, we are able to drive Raman transitions at $\Delta m = -2$ using the σ^- and σ^+ polarizations, as illustrated in Figure 4.4.

Having different polarizations, these two different configurations ($\sigma^-\pi$ and $\sigma^-\sigma^+$)

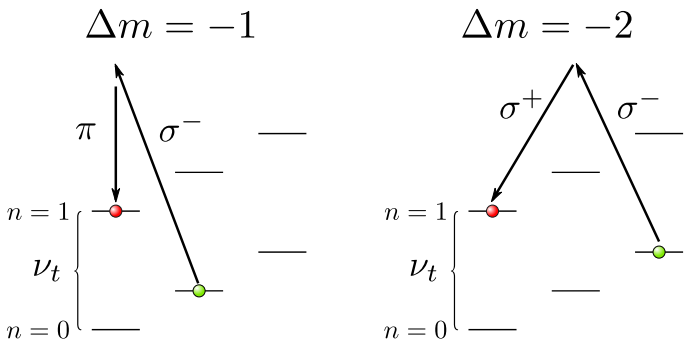

Figure 4.4: Comparison between blue sideband pulses at $\Delta m = -1$ using $\sigma^-\pi$ polarization configuration and at $\Delta m = -2$ using $\sigma^-\sigma^+$ polarization configuration.

stimulate Raman transitions with $\Delta m = -1$ and $\Delta m = -2$, respectively, and have different coupling coefficients. We studied how the coupling coefficients change when implementing the third branch with σ^+.

For the $^{40}CaH^+$ molecule, we calculate all coupling coefficients of the transitions within the same sub-manifold, focusing first on $\xi = -$ and then on $\xi = +$. This procedure is carried out for both the $\sigma^-\pi$ configuration at $\Delta m = -1$, and the $\sigma^-\sigma^+$ configuration at $\Delta m = -2$. Figure 4.5 reports a comparison between the two Raman configurations of the absolute value of the coupling coefficients as a function of m_F^{init} (the m_F of the initial level of the transition), for both sub-manifolds.

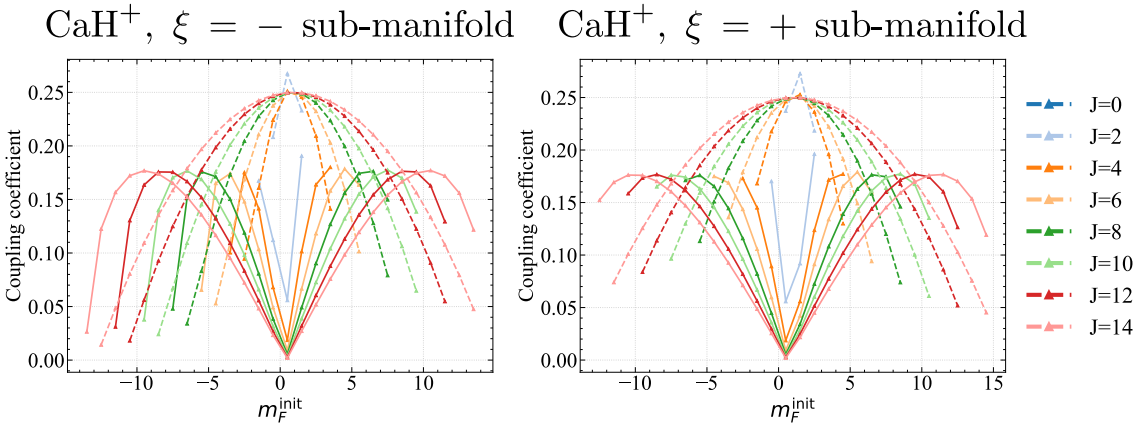

Figure 4.5: Absolute value of the coupling coefficients of transitions within the upper (left) and lower (right) sub-manifolds as a funciton of m_F^{init}, the projection of total angular momentum of the initial state of the transition. For different manifolds J, a comparison between the $\sigma^-\pi$ (solid lines, $\Delta m = -1$) and $\sigma^-\sigma^+$ (dashed lines, $\Delta m = -2$) configurations is shown for the $^{40}CaH^+$ molecular ion.

The same analysis of the $^{40}CaOH^+$ molecule is shown in Figure 4.6.

The following observation applies to both molecular ions we consider: for both sub-manifolds, the coupling coefficients tend to vanish in the central region under the $\Delta m =$

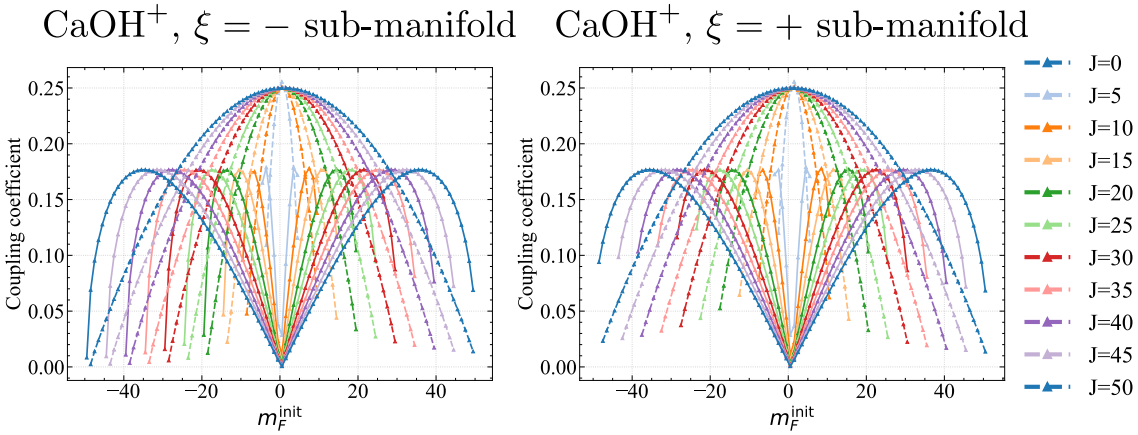

Figure 4.6: Absolute value of the coupling coefficients of transitions within the upper (left) and lower (right) sub-manifolds as a funciton of m_F^{init}, the projection of total angular momentum of the initial state of the transition. For different manifolds J, a comparison between the $\sigma^-\pi$ (solid lines, $\Delta m = -1$) and $\sigma^-\sigma^+$ (dashed lines, $\Delta m = -2$) configurations is shown for the $^{40}CaOH^+$ molecular ion.

-1 configuration. Since the molecular states are only weakly coupled during optical pumping, the population encounters a barrier that prevents its transfer, thereby justifying the presence of a dark state with residual population in the middle of the sub-manifolds.

In contrast, with the $\Delta m = -2$ Raman configuration the coupling coefficients between molecular states are maximized precisely in the region where $m_F \to 0$.

We exploit this property to develop an updated pumping scheme that also incorporates the $\sigma^-\sigma^+$ configuration. The updated three-branch pumping scheme we propose consists of the following steps:

1. BSB Raman pulse at ν_1, using the $\sigma^-\pi$ configuration with $\Delta m = -1$, to pump the population of the upper sub-manifold to the left with some trapping in the middle of the upper sub-manifold.

2. BSB Raman pulse at ν_2, using the $\sigma^-\pi$ configuration with $\Delta m = -1$, to pump the population of the lower sub-manifold to the left with some trapping in the middle of the lower sub-manifold.

3. BSB Raman pulse at $2 \cdot \nu_1$, using the $\sigma^-\sigma^+$ configuration with $\Delta m = -2$, to remove the trapped population in the upper sub-manifold. A factor of two arises because the transitions are driven not between neighboring states, but between states separated by an intermediate molecular state, thereby doubling the energy difference.

4. BSB Raman pulse at $2 \cdot \nu_2$, using the $\sigma^-\sigma^+$ configuration with $\Delta m = -2$, to remove the trapped population in the lower sub-manifold.

5. BSB Raman pulse at ν_1, using the $\sigma^-\pi$ configuration with $\Delta m = -1$, to complete the transfer of the upper population released in step 3.

6. BSB Raman pulse at ν_2, using the $\sigma^-\pi$ configuration with $\Delta m = -1$, to complete the transfer of the lower population released in the step 4.

This updated six-stage optical pumping scheme is illustrated in Figure 4.7.

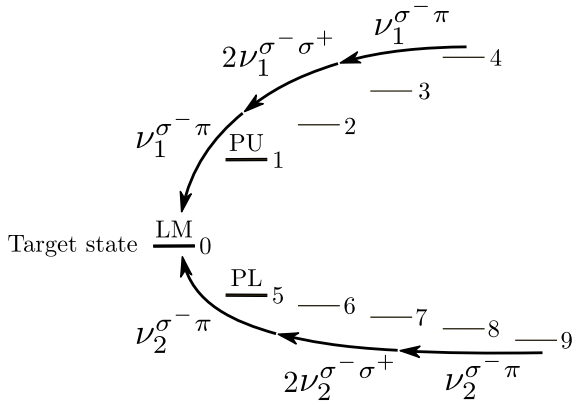

Figure 4.7: Six-stage optical pumping scheme with frequency ν_1 and ν_2 which transfers the population to the leftmost states: the leftmost state (LM, i.e. the target state), penultimate upper state (PU) and penultimate lower state (PL). Two different polarization configuration $\sigma^-\pi$ and $\sigma^-\sigma^+$ are used.

We now simulate the updated optical pumping scheme on the molecular ions by introducing the third branch. Each manifold of the $^{40}CaH^+$ ion is initially prepared in a completely mixed hyperfine state and motional ground state with $B = 3.6\,\text{G}$. Blue-sideband pulses are then simulated with a reduced Rabi frequency of $\Omega_{\text{Raman}} = \Gamma_{\text{cooling}} = 10\,\text{kHz}$, while switching both the Raman detuning ω_{Raman} (between $\nu_1 = -2\,\text{kHz}$ and $\nu_2 = -6\,\text{kHz}$) and the laser configuration ($\sigma^-\sigma^+$ or $\sigma^-\pi$) according to the six-stage scheme described previously. The overall result for the $^{40}CaH^+$ molecule is shown in Figure 4.8.

Similarly, we implement the same procedure for the $^{40}CaOH^+$ ion at $B = 3.27\,\text{G}$. In this case, the blue-sideband pulses are simulated with a reduced Rabi frequency of $\Omega_{\text{Raman}} = \Gamma_{\text{cooling}} = 5\,\text{kHz}$, while the Raman detuning is alternated between $\nu_1 = -350\,\text{Hz}$ and $\nu_2 = 150\,\text{Hz}$, and the polarization configurations ($\sigma^-\sigma^+$ or $\sigma^-\pi$) are applied in accordance with the six-stage protocol. The corresponding population dynamics for $^{40}CaOH^+$ are reported in Figure 4.9.

This simulation of the sequence of $\Delta m = [-1, -2, -1]$ Raman demonstrates that the population that was previously trapped in the middle of the sub-manifolds (see Figures 4.2 and 4.3) is now completely removed, demonstrating the success of this approach.

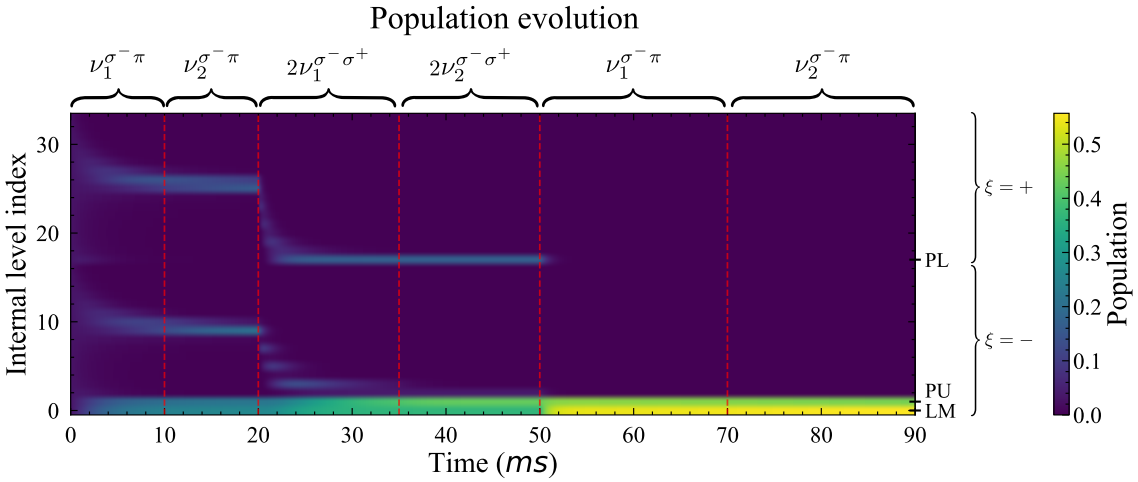

Figure 4.8: Simulation of the six-stage optical pumping scheme applied on the $J = 8$ manifold of the $^{40}CaH^+$ molecule at $B = 3.6$ G. The population evolution of the internal levels (indexed according to the scheme illustrated in Figure 4.7) is displayed. Red dashed lines separate the stages, indicating switching of the laser detuning between $\nu_1 = -2$ kHz and $\nu_2 = -6$ kHz and the associated laser configuration.

At this stage, having removed trapped population from the middle of the sub-manifolds, it is useful to observe the efficiency of optical pumping in the three leftmost states as a function of J. For the remaining manifolds, the population is obtained by fitting. For both molecules, the results of the simulations are shown in Figure 4.10.

For the $^{40}CaOH^+$ molecule, we observe that the target state is moderately populated in the manifolds which are in the intermediate magnetic field regime, around $J \simeq 10$. Moving towards the higher-J manifolds, the population of the target state saturates at approximately 50%, while the remaining population is found in the PU state. This indicates that the population of the entire lower sub-manifold is correctly transferred to the target state, whereas the population of the upper sub-manifold is transferred to the PU state. Indeed, high-J manifolds lie in the Zeeman regime and in this regime the target state lies next to the lower sub-manifold, as shown in Figure 3.2.
Additionally, the target states of the lower-J manifolds are also only half populated, with the remaining population residing in the PL state. In this case, the lower-J manifolds are in the Paschen-Back regime, and the target state is located next to the upper sub-manifold. Consequently, the population of the entire upper sub-manifold is correctly transferred to the target state, while that of the lower sub-manifold remains in the PL state.
Conversely, the $^{40}CaH^+$ molecule does not possess manifolds in the Paschen–Back regime, allowing the target states of the lower-J manifolds to become highly populated. However, the high-J manifolds also lie in the Zeeman regime, and for the same reasons

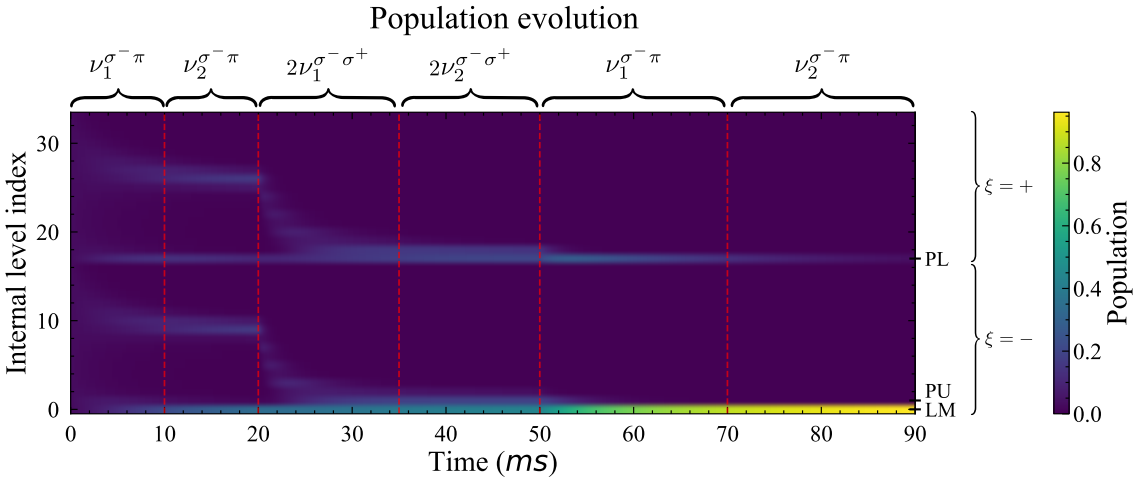

Figure 4.9: Simulation of the six-stage optical pumping scheme applied on the $J = 8$ manifold of the $^{40}CaOH^+$ molecule at $B = 3.27\,G$. The population evolution of the internal levels (indexed according to the scheme illustrated in Figure 4.7) is displayed. Red dashed lines separate the stages, indicating switching of the laser detuning between $\nu_1 = -350\,Hz$ and $\nu_2 = 150\,Hz$ and the associated laser configuration.

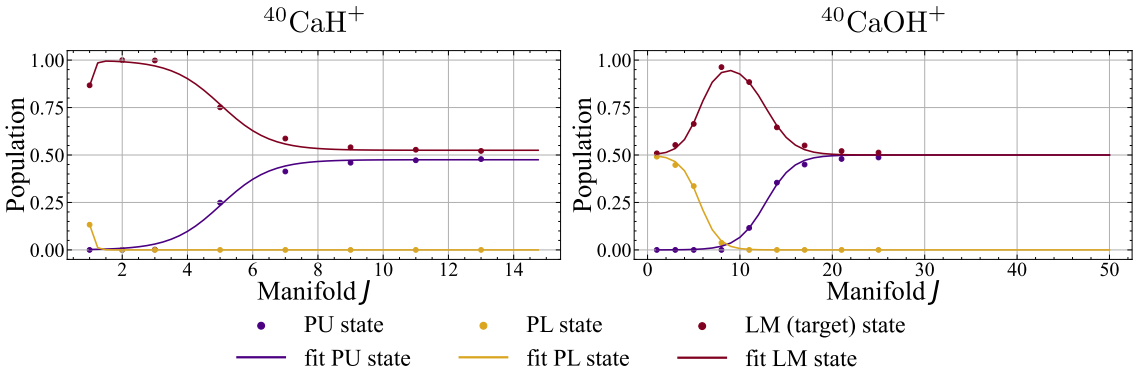

Figure 4.10: Population of the LM, PU and PL states across different manifolds after the six-stage pumping sequence, for the $^{40}CaH^+$ (left) and $^{40}CaOH^+$ (right) molecules.

discussed previously, their target states reach only about half of the total population. In summary, especially for the $^{40}CaOH^+$ molecule, the target state is populated with only half of the total population of the corresponding J manifold most of the time. This implies that when the signature transition is driven, the corresponding signal exhibits a peak signal that is reduced by a factor of two compared to the case where the full population of the manifold is transferred to the target state.

A possible method to overcome this limitation would be to consecutively drive, for each manifold, the specific transition from the PU or PL state to the target state. However, this approach is impractical for $^{40}CaOH^+$ (since it would be possible, if needed, for $^{40}CaH^+$ at room temperature), where the presence of about fifty thermally populated manifolds would require driving fifty consecutive pulses. This substantially increases

the duration of the state-preparation sequence. Moreover, for the $^{40}CaOH^{+}$ molecule, the signature transition frequencies have not been experimentally measured, which introduces uncertainty to the efficiency of this method.
For these reasons, we opt for an alternative, more flexible, and faster method based on the rapid adiabatic passage (RAP) technique, described in the following Section.

4.2 Rapid adiabatic passage (RAP)

To improve the efficiency of state preparation, we employ sideband pulses by rapid adiabatic passage (RAP), explained in the Theory Chapter 2. This technique is particularly useful for refining state preparation in multi-level systems in a way that is robust with respect to experimental parameters [30].
After the optical pumping stage, the most populated molecular states within each manifold are the LM, PU, and PL states. To complete the transfer of population to the target state (LM) of each manifold, we employ Raman-driven RAP sideband pulses which transfer the population of the PU and PL states in the ground motional state to the LM state in the first excited motional state, acting successfully on different manifolds at the same time.
In this scheme, we take advantage of the fact that the target state initially resides in the ground motional state, while the first excited state is unoccupied. By performing RAP pulses on the sideband transition, the population from the PU and PL states can be efficiently transferred to the LM state without disturbing the existing population of the target state. In contrast, if the RAP pulses were applied on the carrier transition, the population in LM would be swapped back to the PU or PL states.
Then, by cooling the system, we transfer the LM population from the first excited motional state to the ground motional state, thus completing the state preparation. The entire procedure is schematically illustrated in Figure 4.11.

The Raman-driven RAP sideband pulses have time-dependent envelope of the reduced Rabi frequency and linearly time-dependent Raman detuning. These influence all manifolds of the molecule simultaneously, so long as the frequency sweep covers the range of transitions we seek to drive.
For each manifold J, the BSB Hamiltonian $H_J^{\mathrm{BSB}}(\Lambda, \Phi_J; t)$ describing the 2-level transition is computed. Here, Λ represents the global parameters including the Raman detuning ω_{Raman} and the reduced Raman Rabi frequency Ω_{Raman}, while Φ_J denotes the local parameters relative to the J-th 2-level transition, i.e., the coupling coefficient c_{ab} and

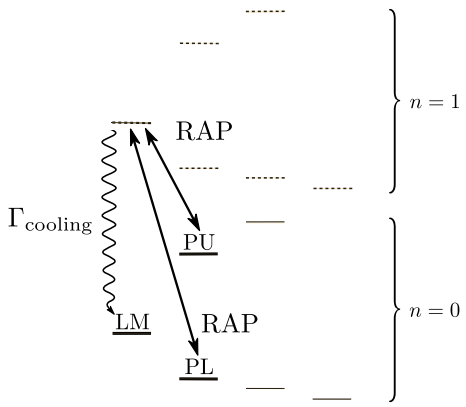

Figure 4.11: Raman-driven RAP pulses acting on the $|\text{PL}\rangle\,|n=0\rangle \leftrightarrow |\text{LM}\rangle\,|n=1\rangle$ and $|\text{PU}\rangle\,|n=0\rangle \leftrightarrow |\text{LM}\rangle\,|n=1\rangle$ transitions. After cooling the system the entire population is transferred to the $|\text{LM}\rangle\,|n=0\rangle$ state.

the molecular transition frequency ω_{mol}. Finally, we initialize the population entirely in the initial states (PU or PL) to compute the population transfer efficiency under the RAP-driven pulses.

For the $^{40}CaH^+$ molecule, we employ a $T = 50\,\text{ms}$ Raman-driven RAP BSB pulse with a Raman detuning $\omega_{\text{Raman}} = -130\,\text{kHz}$ acting on the transition $|\text{PU}\rangle\,|n=0\rangle \leftrightarrow |\text{LM}\rangle\,|n=1\rangle$. Adopting the notation of Eq. (2.47), we set a Raman detuning chirp amplitude $D = 100\,\text{kHz}$, a temporal width of the reduced Rabi frequency Gaussian envelope $\sigma = T/7$, and a peak reduced Rabi frequency $\Omega_0 = 50\,\text{kHz}$. The adiabaticity condition of Eq. (2.50) is satisfied across all manifolds.

The population initially residing in the PU states within the ground motional state is efficiently transferred to the LM state in the first excited motional state with 80% fidelity for the manifolds between $J = 4$ and $J = 13$. To provide a representative example, the time-dependent envelopes of the reduced Rabi frequency $\Omega(t)$ and the laser detuning $\Delta(t)$ for the $J = 14$ manifold are shown in Figure 4.12a, while the corresponding simulated population transfer dynamics are presented in Figure 4.12b.

Regarding the $^{40}CaOH^+$ molecule, multiple RAP pulses are required since the number of populated manifolds is much larger (50 instead of 14) and a single RAP pulse cannot simultaneously address all of them while satisfying the adiabaticity condition.

Moreover, for lower J, it is necessary to transfer the population from the PL state to the target state. For this reason, we employ the following four RAP pulses with pulse duration $T = 50\,\text{ms}$, $\sigma = T/7$ and $\Omega_0 = 50\,\text{kHz}$:

1. PL state populations of all the manifolds are transferred with a pulse acting on the transition $|\text{PL}\rangle\,|n=0\rangle \leftrightarrow |\text{LM}\rangle\,|n=1\rangle$. We set the Raman detuning $\omega_{\text{Raman}} = -10\,\text{kHz}$ and $D = 70\,\text{kHz}$.

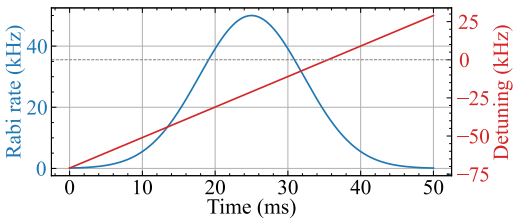

(a) Time-dependent envelopes of the reduced Rabi frequency $\Omega(t)$ and the laser detuning $\Delta(t)$ for the $J = 14$ manifold in $^{40}CaH^+$.

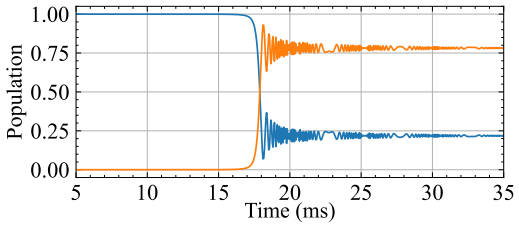

(b) Population transfer under the Raman-driven RAP BSB pulse between the $|0\rangle = |PU\rangle\,|n = 0\rangle$ (blue line) and $|1\rangle = |LM\rangle\,|n = 1\rangle$ (orange line) states of the $J = 14$ manifold in $^{40}CaH^+$.

Figure 4.12: $T = 50$ ms Raman-driven RAP BSB pulse with $\omega_{\text{Raman}} = -130$ kHz, $D = 100$ kHz, $\sigma = T/7$ and $\Omega_0 = 50$ kHz.

2. PU state populations are transferred with a 80% fidelity in the manifolds between $J = 1$ and $J = 33$ with a pulse acting on the transition $|PU\rangle\,|n = 0\rangle \leftrightarrow |LM\rangle\,|n = 1\rangle$. We set the Raman detuning $\omega_{\text{Raman}} = -60$ kHz and $D = 60$ kHz.

3. PU state populations are transferred with a 80% fidelity in the manifolds between $J = 36$ and $J = 43$ with a pulse acting on the transition $|PU\rangle\,|n = 0\rangle \leftrightarrow |LM\rangle\,|n = 1\rangle$. We set the Raman detuning $\omega_{\text{Raman}} = -60$ kHz and $D = 25$ kHz.

4. PU state populations are transferred with a 80% fidelity in the manifolds between $J = 45$ and $J = 49$ with a pulse acting on the transition $|PU\rangle\,|n = 0\rangle \leftrightarrow |LM\rangle\,|n = 1\rangle$. We set the Raman detuning $\omega_{\text{Raman}} = -70$ kHz and $D = 25$ kHz.

At this stage, having simulated the optical pumping and Raman-driven RAP pulse sequences that constitute the state preparation scheme, we can analyze the population of the LM, PU and PL states as a function of J. The results of the simulations for both molecules are shown in Figure 4.13.

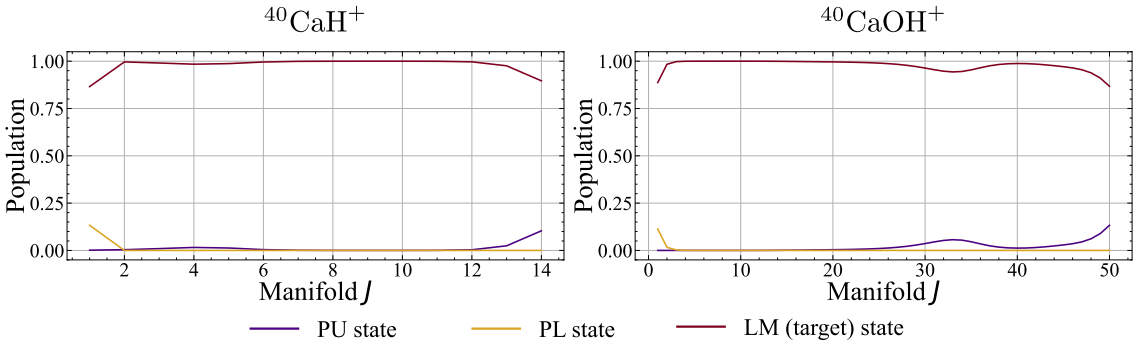

Figure 4.13: Population of the LM, PU and PL states across different manifolds after the six-stage pumping and Raman-driven RAP pulse sequences, for $^{40}CaH^+$ (left) and $^{40}CaOH^+$ (right).

Comparing these results with the state population in the absence of the RAP sequence (shown in Figure 4.10), it is evident that the target states are populated with nearly the

entire population of the corresponding manifold. In this way, after having devised an ad-hoc pumping scheme and applied the RAP pulses, we have an efficient hyperfine state preparation scheme for these molecular ions.

4.3 Pumped spectrum

The optical pumping and RAP stages form a robust state preparation scheme for these molecular ions, where the target states $|\mathcal{T}_J\rangle$ are populated with near unity efficiency. At this point, we proceed to simulate the molecular ion CW Raman spectrum, that we refer to as the *pumped spectra*.

Computing the pumped spectrum serves two purposes. First, it verifies that the state preparation was successful. In particular, we expect an enhanced SNR associated with the J-dependent signature transitions, with peaks nearly as high as the corresponding manifold population P_J. Second, it allows us to compare the simulations with the experimental data. In addition to the hyperfine spectra, the $^{40}CaH^+$ pumped spectrum has already been experimentally measured. We apply the physics simulator on the $^{40}CaH^+$ ion as a validation benchmark before expanding the model to the $^{40}CaOH^+$ molecule, whose pumped spectrum has not yet been experimentally obtained.

The following experimental imperfections have been considered for both molecules, as explained and motivated in Chapter 3:

1. **Miscalibration**: at the start of the simulation, each parameter is randomly selected once from a Gaussian distribution.

   (a) **Frequency**: Gaussian distribution with standard deviation $\sigma = 50\,\text{Hz}$,

   (b) **Reduced Rabi frequency**: Gaussian distribution with standard deviation $\sigma =$ 10% of the nominal value.

2. **Shot-to-shot fluctuation**: the parameter value is taken from a Gaussian distribution for every laser pulse.

   (a) **Frequency**: Gaussian fluctuations with standard deviation $\sigma = 30\,\text{Hz}$,

   (b) **Reduced Rabi frequency**: Gaussian fluctuations with standard deviation $\sigma = 1\%$ of the nominal value.

A false positive detection rate of 1% is accounted for in the simulations. The ODF excitation is not simulated, as it is confined near the zero-frequency region and does not affect the signal of the signature transitions. To evaluate the efficiency of optical pumping alone, we simulate the pumped spectra without the RAP pulses. We consider the $^{40}CaH^+$ molecule after the six-stage optical pumping with $B = 3.6\,G$ and $T = 300\,K$. The laser drives $\Delta m = -1$ blue-sideband transitions with $t = 1000\,\mu s$ pulses at various reduced Rabi frequencies ($\Omega_{Raman} = 3.0\,kHz$ and $6.0\,kHz$).
We also simulate the $^{40}CaOH^+$ molecule after the six-stage optical pumping at $B = 3.27\,G$ and $T = 300\,K$. The laser drives $\Delta m = -1$ blue-sideband transitions with $t = 5000\,\mu s$ pulses at various reduced Rabi frequencies ($\Omega_{Raman} = 0.9\,kHz$, $3.0\,kHz$ and $6.0\,kHz$). The simulated pumped CW Raman spectra for $^{40}CaH^+$ and $^{40}CaOH^+$, probed with 1000 scan points, are shown in Figures 4.14a and 4.14b, respectively.
The peaks associated with the J-dependent signature transitions are clearly visible, especially for the $^{40}CaH^+$ ion due to the higher thermal populations in each of the smaller set of manifolds. The $^{40}CaH^+$ simulated pumped spectrum closely resembles the experimental measurement [9]. This agreement validates the physics simulator, allowing it to be applied to the $^{40}CaOH^+$ molecule. Conversely, despite that the $^{40}CaOH^+$ spectrum is partially obscured by the false positive signal and the signature transition frequencies are closely spaced, their peaks are visible for a broad range of J. In general, lower reduced Rabi frequencies lead to a higher SNR for the lower-J signature transitions, as the frequency differences are better resolved.
At this point, we repeat the simulations of the spectra, keeping the same laser parameters while considering the molecular ions subjected to both the optical pumping stage and RAP pulses, which couple population from states with significantly different transition frequencies from the majority of the Zeeman states. The simulated CW Raman spectra for $^{40}CaH^+$ and $^{40}CaOH^+$ after the entire state preparation procedure are shown in Figures 4.15a and 4.15b.
The signature transition SNR is improved for both molecules. The $^{40}CaOH^+$ molecule gains a more significant advantage from the RAP pulses, as the peaks appear with more contrasts over a broader range of J with respect to the previous case. For a qualitative comparison, Figures 4.16a and 4.16b show the previously calculated spectra at reduced Rabi frequency $\Omega_{Raman} = 6.0\,kHz$, both with and without the application of RAP pulses, for the two molecules.
Even though the signature transitions are distinguishable after the pumping stage, the RAP pulses improve the SNR, especially for the $^{40}CaOH^+$ molecule where the excitation probability is partially obscured by the false positive signal and a small enhancement

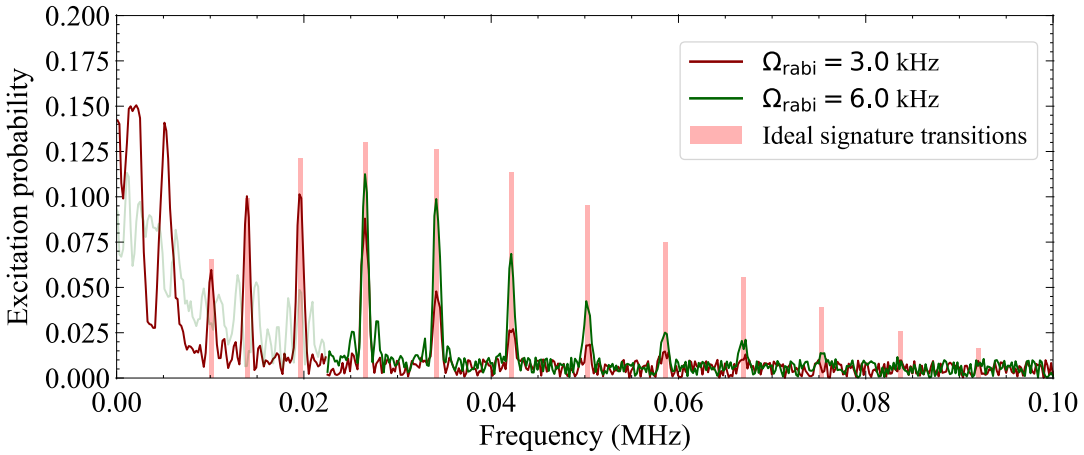

(a) The $^{40}CaH^+$ simulated spectrum at $B = 3.6$ G with $t = 1$ ms pulses, 1000 scan point, at reduced Rabi frequencies $\Omega_{Raman} = 3.0$ kHz and 6.0 kHz.

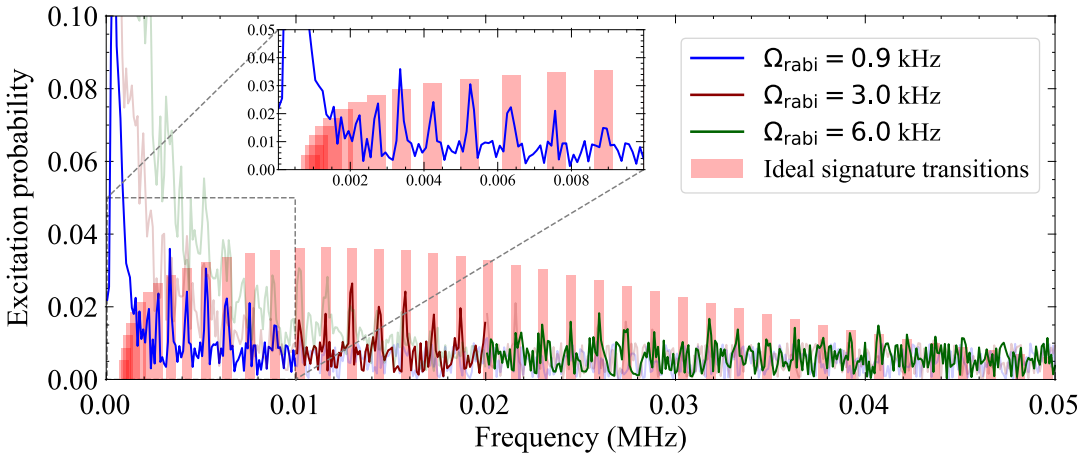

(b) The $^{40}CaOH^+$ simulated spectrum at $B = 3.27$ G with $t = 5$ ms pulses, 1000 scan point, at reduced Rabi frequencies $\Omega_{Raman} = 0.9$ kHz, 3.0 kHz and 6.0 kHz.

Figure 4.14: CW Raman spectra for $^{40}CaH^+$ (top) and $^{40}CaOH^+$ (bottom) after the six-stage optical pumping scheme without RAP pulses.

can make the difference between resolving and missing a peak. Furthermore, the RAP pulses constitute an essential tool to reduce the space of accessible states within the manifold to a single state, thereby enabling the identification of both the manifold and the Zeeman state.

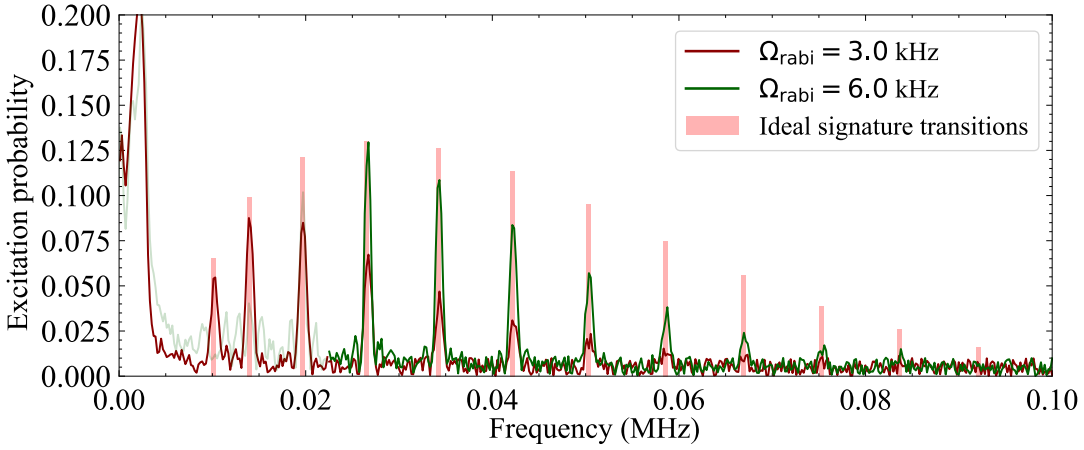

(a) The $^{40}CaH^+$ simulated spectrum at $B = 3.6$ G with $t = 1$ ms pulses, 1000 scan point, at reduced Rabi frequencies $\Omega_{Raman} = 3.0$ kHz and 6.0 kHz.

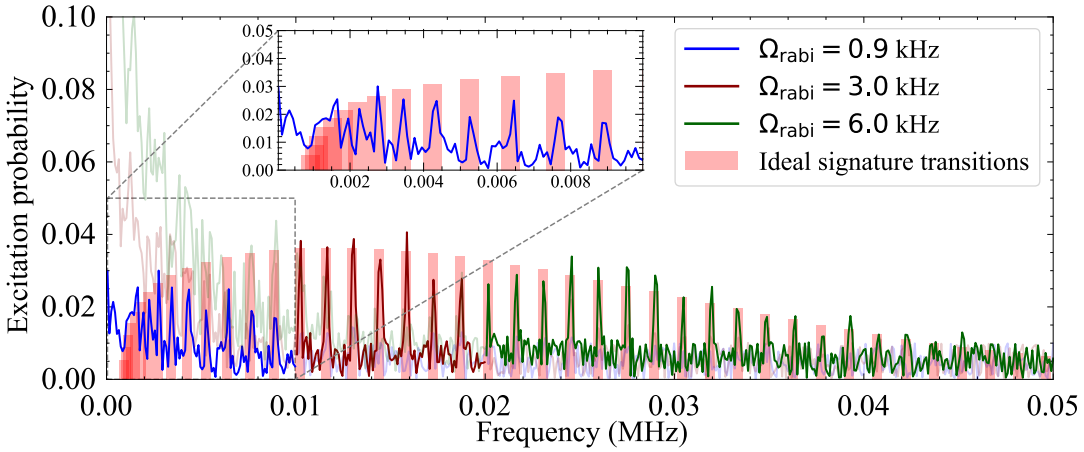

(b) The $^{40}CaOH^+$ simulated spectrum at $B = 3.27$ G with $t = 5$ ms pulses, 1000 scan point, at reduced Rabi frequencies $\Omega_{Raman} = 0.9$ kHz, 3.0 kHz and 6.0 kHz.

Figure 4.15: CW Raman spectra for $^{40}CaH^+$ (top) and $^{40}CaOH^+$ (bottom) after the six-stage optical pumping scheme and RAP pulses.

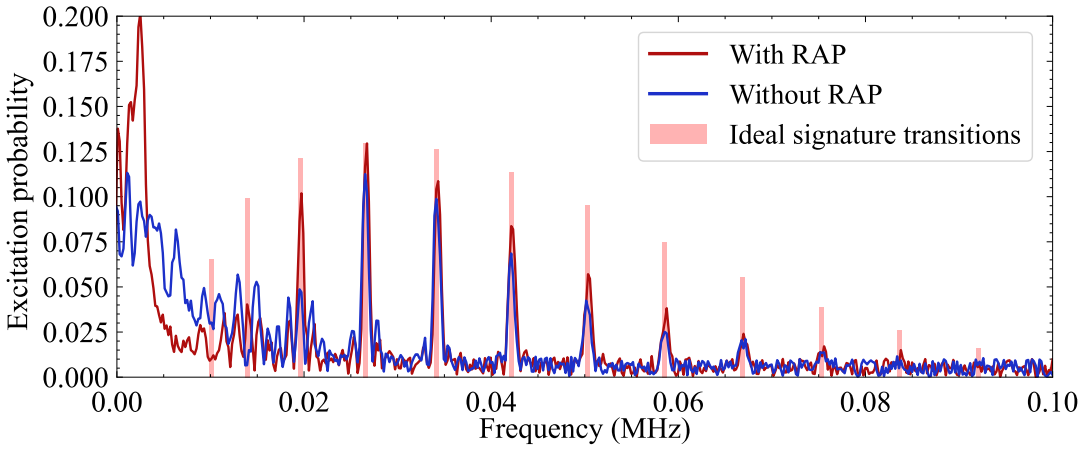

(a) The $^{40}CaH^+$ simulated spectrum at $B = 3.6$ G with $t = 1$ ms pulses, 1000 scan point, at reduced Rabi frequency $\Omega_{\text{Raman}} = 6.0$ kHz.

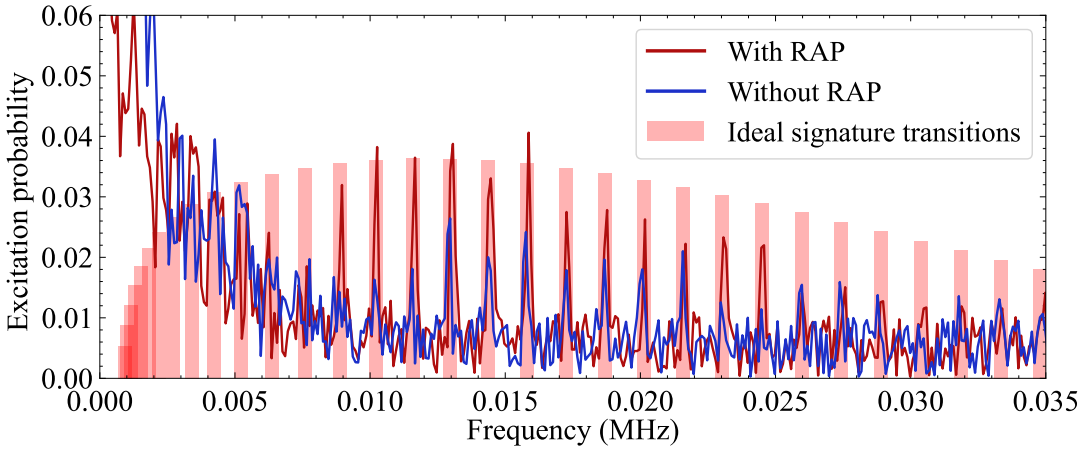

(b) The $^{40}CaOH^+$ simulated spectrum at $B = 3.27$ G with $t = 5$ ms pulses, 1000 scan point, at reduced Rabi frequency $\Omega_{\text{Raman}} = 6$ kHz.

Figure 4.16: Comparison of the CW Raman spectra for $^{40}CaH^+$ (top) and $^{40}CaOH^+$ (bottom) after the six-stage optical pumping scheme with and without RAP pulses.

5

Bayesian state estimation

The efficient preparation and identification of quantum states in molecular systems are essential prerequisites for implementing high-fidelity quantum control protocols. In this context, the state-preparation stage as previously discussed aims to transfer the thermal population from each molecular manifold to its corresponding target state, and the simulated pumped spectrum illustrates this population redistribution.
In this Chapter, we develop a framework designed to significantly enhance the quantum control of a wide class of molecular species – including complex polyatomic molecular ions – by exploiting the powerful toolbox provided by quantum logic spectroscopy (QLS), which enables precise and non-destructive interrogation of molecular states.
These techniques rely on the ability to infer the manifold, and thus the state, of molecules, which is almost impossible to track in some molecular species such as $^{40}CaOH^{+}$. This is due to the presence of numerous states, closely spaced energy levels, and overlapping transitions making direct state readout difficult.
To overcome these limitations, we explore Bayesian state estimation to infer the molecular state distribution based on measurement outcomes, incorporating prior knowledge from the state distribution of the molecule. This framework would allow us to control and manipulate the identified molecular state.

5.1 Bayesian molecular state inference framework

Bayes' theorem [49] provides a fundamental framework for updating the probability distribution of a set of parameters Θ in light of new experimental evidence. It relates the prior knowledge about the system, encoded in the distribution $P(\Theta)$, to the updated belief after a measurement outcome m is observed [50]. Formally, the theorem can be

expressed as

$$P(\Theta|m) = \frac{P(m|\Theta)P(\Theta)}{P(m)}, \tag{5.1}$$

where $P(m|\Theta)$ is the *likelihood* of obtaining the measurement outcome m given a particular set of parameters Θ, and $P(m) = \int P(m|\Theta)P(\Theta)d\Theta$ is a normalization constant called *evidence* or *marginal likelihood* that ensures that the posterior distribution integrates to one.

The probability distribution $P(\Theta)$ is referred to as the *prior*, representing our initial knowledge or assumptions about the parameters before performing the measurement. The updated distribution $P(\Theta|m)$ is called the *posterior*, and quantifies our refined knowledge after taking into account the measurement results.

In our case, the model parameter to be estimated, Θ, represents the molecular state we want to infer, s. The prior and posterior are therefore the probability distributions of the molecular states before and after the measurements, which depend on the so-called experimental design ξ. The experimental design represents some controllable aspects of an arbitrary experiment, whose choice will influence the experiment's outcome [51]. The design includes the choice of the types of pulses to drive in order to obtain an outcome (linked to the choice of transitions to excite, if one or more) and the order in which they are performed sequentially, as well as the experimental parameters, such as Raman detuning and reduced Rabi frequency.

In this context, we consider a fixed design, determined prior to the experiment and independent of the measurement outcomes: for this reason, this inference problem is called *static* Bayesian state estimation. Molecular states constitute a discrete set, and the domain of priors and posteriors is a discrete space: this greatly reduces the calculation speed of Bayes' theorem.

As a consequence, Bayes' theorem becomes:

$$P(s|m_k, \xi) = \frac{P(m_k|s, \xi)P(s, \xi)}{\sum_s P(m_k|s, \xi)P(s, \xi)}. \tag{5.2}$$

By performing consecutive measurements, we can iteratively incorporate the information gained at each step, updating the probability distribution accordingly. In this framework, the posterior from the previous iteration serves as the prior for the next one:

$$P^{(t+1)}(s|m_k^{(t+1)}, \xi) = \frac{P(m_k^{(t+1)}|s, \xi)P^{(t)}(s, \xi)}{\sum_s P(m_k^{(t+1)}|s, \xi)P^{(t)}(s, \xi)}. \tag{5.3}$$

In the framework of quantum logic spectroscopy, each measurement yields a binary outcome corresponding to the detection or absence of fluorescence from the logic ion. An outcome $m_k = 1$ denotes the observation of fluorescence photons, indicating that the excitation process has occurred and that the molecular transition of interest has been successfully driven. Conversely, an outcome $m_k = 0$ corresponds to the absence of fluorescence, implying that the excitation did not take place and the molecule remained in its initial (dark) state. These two possible outcomes define a discrete measurement space $\{0, 1\}$, consistent with projective measurements on a two-level system.

5.1.1 Likelihood computation

The physical system under consideration is a quantum system. Consequently, the outcome of a measurement physically changes the state: by conditioning on a specific measurement result, we project the system onto the corresponding quantum state. This process is called post-selection, and it is fundamentally different from a mere reweighting of probability distributions, where one only updates statistical weights without altering the underlying physical state.
For this reason, the likelihood represents two distinct meanings:

1. Likelihood as a physical transition map: $P(m_k|s, \xi)$ represents the physical effect of the measurement. The result corresponds to the evolution of the state after the measurement, conditioned on the outcome.

2. Likelihood as a purely Bayesian object: $P(m_k|s, \xi)$ represents the probability of obtaining the outcome given the state, without implying any physical change of the state itself. In this sense, the likelihood serves only to perform a knowledge update, not a physical evolution.

The two representations can coincide if the likelihood is expressed as a map that describes both the outcome probabilities *and* the physical transformation of the state given the outcome.
In our context, given the need for a computationally efficient model, we must develop a classical framework that reproduces the underlying quantum phenomena. Following the same rationale discussed in Section 3.2, coherences are neglected, and the multi-level system is approximated as a mixed state. Only the populations are simulated, allowing us to compute the excitation probabilities of the molecular states.
For these reasons, the likelihoods are expressed in matrix form, using excitation matrices.

The excitation matrix T_J represents a classical transition matrix that describes the transition probabilities between the molecular states within the J manifold.
We define $M_{\xi=-} = \{-J - 1/2, ..., J - 1/2\}$ and $M_{\xi=+} = \{-J + 1/2, ..., J + 1/2\}$ as the sets of quantum numbers m_F corresponding to the lower and upper sub-manifolds, respectively. The states belonging to the J-th manifold are then denoted as:

$$S_J = \{|J, -, m\rangle_{m\in M_-}, |J, +, m\rangle_{m\in M_+}\}. \tag{5.4}$$

Thus, S_J contains all $2(2J + 1)$ states associated with the J-th manifold, with the sub-manifold ordering $\xi = -$ preceding $\xi = +$.
The overall state space is therefore

$$S = \{S_{J=0}, S_{J=1}, ..., S_{J=J_{\max}}\} \tag{5.5}$$

and its dimension is $n = \dim(S) = \sum_{J=0}^{J_{\max}} 2(2J + 1)$. The transition matrix of the J-th manifold then becomes:

$$T_J = \begin{pmatrix} p_{S_J^{(1)}\to S_J^{(1)}} & p_{S_J^{(2)}\to S_J^{(1)}} & \cdots & p_{S_J^{(2(2J+1))}\to S_J^{(1)}} \\ p_{S_J^{(1)}\to S_J^{(2)}} & p_{S_J^{(2)}\to S_J^{(2)}} & & \vdots \\ \vdots & & \ddots & \vdots \\ p_{S_J^{(1)}\to S_J^{(2(2J+1))}} & \cdots & \cdots & p_{S_J^{(2(2J+1))}\to S_J^{(2(2J+1))}} \end{pmatrix}, \tag{5.6}$$

where the two-state excitation probabilities are computed according to Eq. (2.6).
Since the Raman laser does not drive transitions between states belonging to different manifolds, the total transition matrix is block-diagonal and can be written as follows:

$$T = \left(\begin{array}{c|c|c|c} T_{J=0} & \mathbf{o} & \cdots & \mathbf{o} \\ \hline \mathbf{o} & T_{J=1} & \cdots & \mathbf{o} \\ \hline \vdots & \vdots & \ddots & \vdots \\ \hline \mathbf{o} & \mathbf{o} & \cdots & T_{J=J_{\max}} \end{array}\right). \tag{5.7}$$

For T to represent a physically valid transformation, it must preserve probabilities. There-

fore, all its elements are non-negative, and each column sums to one:

$$T_{ij} \geq 0, \qquad \sum_i T_{ij} = 1 \quad \forall j. \tag{5.8}$$

In this way, we build the likelihood associated with outcome 0, $\mathscr{L}_0$, by considering the diagonal elements of the matrix T, which represent the probabilities that each state remains unexcited given the outcome $m_k = 0$:

$$\mathscr{L}_0 = P(m_k = 0|s, \xi) = \mathrm{diag}(T) = \begin{pmatrix} p_{S^{(1)}\to S^{(1)}} & \mathbf{0} & \cdots & \mathbf{0} \\ \mathbf{0} & p_{S^{(2)}\to S^{(2)}} & & \vdots \\ \vdots & & \ddots & \mathbf{0} \\ \mathbf{0} & \cdots & \mathbf{0} & p_{S^{(n)}\to S^{(n)}} \end{pmatrix}, \tag{5.9}$$

with $s \in S$. The likelihood associated with outcome 1, $\mathscr{L}_1$, is the complementary matrix, which contains only the off-diagonal elements of T, i.e., those representing transitions between different states:

$$\mathscr{L}_1 = P(m_k = 1|s, \xi) = T - \mathscr{L}_0$$

$$= \begin{pmatrix} \mathbf{0} & p_{S^{(2)}\to S^{(1)}} & \cdots & p_{S^{(n)}\to S^{(1)}} \\ p_{S^{(1)}\to S^{(2)}} & \mathbf{0} & & \vdots \\ \vdots & & \ddots & p_{S^{(n)}\to S^{(n-1)}} \\ p_{S^{(1)}\to S^{(n)}} & \cdots & p_{S^{(n-1)}\to S^{(n)}} & \mathbf{0} \end{pmatrix}, \tag{5.10}$$

with $s \in S$. For each initial state $S^{(i)}$, the sum of the transition probabilities over all possible final states and outcomes must equal one, which is indeed satisfied:

$$\sum_i \left(\mathscr{L}_{0i,j} + \mathscr{L}_{1i,j}\right) = \sum_i T_{i,j} = 1. \tag{5.11}$$

The prior and posterior probability distributions are represented as probability vectors, obtained by concatenating all molecular states ordered according to the state sets defined in Eq. 5.5:

$$P(s, \xi)^{\mathrm{T}} \qquad \text{with} \quad s \in S. \tag{5.12}$$

At each step t, the iterative Bayes' theorem is applied but the posterior is not computed as an element-wise product between the likelihood and the prior; instead, it is obtained

through a matrix–vector multiplication:

$$P^{(t+1)}(s|m_k^{(t+1)},\xi) \propto \mathscr{L}_k P^{(t)}(s,\xi), \tag{5.13}$$

followed by normalization.

5.1.2 Monte Carlo sampling for Bayesian inference

In each run of the simulation, the molecular state is inferred by applying the iterative Bayesian update rule. At every measurement step, the posterior probability distribution over the molecular states is updated according to the likelihood of the observed outcome and the prior distribution from the previous iteration. Because the molecular system under study includes a large number of internal states distributed across multiple rotational manifolds, it is essential to account for both the thermal population of the manifolds and the relative distribution of population among the states within each manifold. These distributions reflect the specific state-preparation scheme performed prior to the inference process and encode our prior knowledge about the system configuration.

To obtain statistically reliable results and to properly characterize the stochastic nature of the system dynamics, we adopt a Monte Carlo approach in which a large number of independent simulation runs are performed [52, 53]. Each run starts from a different initial molecular state randomly sampled according to the initial thermal and Zeeman-prepared distributions. The number of Monte Carlo realizations required depends on the number of available initial states and the structure of the state space. Since the state-preparation procedure significantly reduces the effective space of possible molecular states, the set of relevant initial conditions becomes limited – typically to one target state per manifold J of the molecular ion. This corresponds to approximately 14 states for $^{40}CaH^+$ and about 50 for $^{40}CaOH^+$. Nevertheless, intrinsic quantum and experimental stochastic mechanisms can cause fluctuations even under nominally identical initial conditions, meaning that repeated simulations are still required to capture the full statistical behavior of the system. Consequently, a high number of Monte Carlo runs is necessary to achieve convergence of the estimated probabilities and to provide a statistically meaningful validation of the Bayesian inference algorithm.

5.2 Bayesian model

5.2.1 Measurement settings

In the context of static Bayesian state estimation we need to compute an ensemble of measurement settings a priori which represent the set of possible pulses to drive in order to excite the molecules with the aim of inferring its state. To identify the molecular state we employ the J-dependent signature transitions (STs) between the target (LM) and the penultimate upper (PU) states $|J, -J-1/2, -\rangle \leftrightarrow |J, -J+1/2, -\rangle$.
These transitions uniquely identify the manifold J if the molecular ion lies in the intermediate magnetic field regime. The $^{40}CaH^+$ molecule's thermally-populated states nearly all lie in the intermediate regime at $B = 3.6\,\mathrm{G}$, and the signature transitions differ several kHz from each other allowing them to be singularly addressed. In contrast, signature transition frequencies in $^{40}CaOH^+$ overlap and are closely spaced: this is due to the fact that lower-J manifolds lie in the Paschen-Back regime, and higher-J manifolds in the Zeeman regime. Hence, in addition to being more sensitive to experimental imperfections, driving a ST can also excite neighboring STs, complicating unambiguous manifold detection.
For these reasons, the Raman difference frequencies of the pulses composing the measurement settings are set equal to the signature transition frequencies. To drive the transitions we need to consider both negative ST frequencies $|\mathrm{PU}\rangle \rightarrow |\mathrm{LM}\rangle$ at $\Delta m = -1$, and positive frequencies $|\mathrm{LM}\rangle \rightarrow |\mathrm{PU}\rangle$ at $\Delta m = +1$.
Moreover, to maximize excitation of STs, π-pulses must be considered and π-pulse durations, t_J^π, need to be computed. Given the reduced Raman Rabi frequency Ω_{Raman} and the coupling coefficient of the J-th signature transition c_J^{ST}, the π-pulse duration is given by:

$$t_J^\pi = \frac{\pi}{\Omega_{\mathrm{Raman}} \cdot c_J^{\mathrm{ST}}}. \tag{5.14}$$

Denoting the set of ST frequencies at negative frequency ($\Delta m = -1$) and at positive frequency ($\Delta m = +1$) respectively as:

$$\begin{aligned} \mathscr{F}_- &= \left\{ \omega^{(-)}_{\mathrm{Raman},J} = \frac{1}{\hbar}\Delta E_{a_J \rightarrow b_J} \middle| J = 1, \dots J_{\max} \right\} \\ \mathscr{F}_+ &= \left\{ \omega^{(+)}_{\mathrm{Raman},J} = \frac{1}{\hbar}\Delta E_{b_J \rightarrow a_J} \middle| J = 1, \dots J_{\max} \right\}, \end{aligned} \tag{5.15}$$

where $a_J = |\mathrm{LM}\rangle_J = |J, -J - 1/2, -\rangle$ and $b_J = |\mathrm{PU}\rangle_J = |J, -J + 1/2, -\rangle$, the measurement setting ensemble is defined as:

$$\mathscr{P} = \left\{ \mathscr{P}_- = \left(\mathscr{F}_-^{(J)}, t_J^\pi, \Omega_{\mathrm{Raman}}\right), \mathscr{P}_+ = \left(\mathscr{F}_+^{(J)}, t_J^\pi, \Omega_{\mathrm{Raman}}\right) \middle| J = 1, \dots J_{\max} \right\}. \tag{5.16}$$

Each measurement pulse is uniquely associated with the likelihoods for the 0 and 1 outcomes, determined by the Raman laser parameters:

$$\mu \longleftrightarrow (\mathscr{L}_0, \mathscr{L}_1), \qquad \forall \mu \in \mathscr{P}. \tag{5.17}$$

This allows us to pre-compute both the measurement settings and the likelihoods at the beginning of the experiment, reducing the computational cost of the Bayesian algorithm.
The measurement pulse is always followed by a detection procedure that reveals the 0 or 1 outcome, allowing us to consider the correct likelihood for the Bayesian update. As a consequence, in order to drive the measurement pulse and detect the outcome, the following times must be considered:

- Sideband cooling sequence of 15 ms to bring the system into the motional ground state,
- Red-sideband pulse of 100 µs to transfer the state of the spectroscopy ion to the logic one,
- Detection time of 500 µs to detect the 0/1 outcome with the fluorescence signal on the logic ion.

The sideband cooling process is the most time-consuming.

It is possible to build different kinds of measurements in order to decrease the time the inference process takes to converge. This approach would conceive a measurement as composed of multiple pulses with a single detection event and sideband cooling process. In absence of experimental imperfections, a 0 outcome means that none of the pulses excited the molecule while a 1 outcome means that at least one pulse drove a transition without revealing which of those. Driving different pulses and realizing a single detection and cooling process would optimize the duty cicle of the experiment.
If the measurement is composed of multiple shots, each of those is associated with a

transition matrix which changes the state distribution:

$$P(s,\xi) \xrightarrow{T_1} T_1 P(s,\xi) \xrightarrow{T_2} T_2 T_1 P(s,\xi) \dots \xrightarrow{T_n} T_n \dots T_2 T_1 P(s,\xi). \tag{5.18}$$

The total measurement transition matrix is then $T_{\text{tot}} = T_n \dots T_2 T_1$, allowing us to compute the likelihoods $\mathscr{L}_0$ and $\mathscr{L}_1$ using Eqs. (5.9) and (5.10).
In the Bayesian inference process the pumping sequence will be also used. However, since the pumping is not followed by a measurement detection and it is not associated with an outcome, there are no likelihoods related to it and it does not represent a measurement pulse. Nevertheless, the pumping sequence changes the state distribution, and from the analysis from the Chapter 4 we can retrieve the updated state population and modify the prior accordingly.

5.2.2 Experimental imperfections and Bayesian strategies

Experimental imperfections have a crucial influence on the Bayesian state estimation process, strongly affecting its inference efficiency. This is especially true for the $^{40}CaOH^{+}$ molecule where the signature transition frequencies are overlapping and closely-spaced. The exact magnitudes of the experimental imperfections are unknown, but we can make the following educated guesses:

1. **False positive rate** set to $p_{\text{fp}} = 3\%$, which represents the probability to classify a 0 outcome as a 1 outcome due to spurious motional excitation, either from imperfect cooling or heating during the sequence,

2. **False negative rate** set to $p_{\text{fn}} = 3\%$, which represents the probability to classify a 1 outcome as a 0 outcome due to unwanted cooling, spontaneous decay, or off-resonant coupling to the carrier from the Raman pulse,

3. **Miscalibration**: represents constant offsets from the nominal values that are drawn once at the beginning of each run:

   (a) **Raman difference frequency**: we consider a Gaussian distribution with standard deviation $\sigma^{\text{mis}}_{\omega_{\text{Raman}}} = 50\,\text{Hz}$,

   (b) **Reduced Rabi frequency**: we consider a Gaussian distribution with standard deviation $\sigma^{\text{mis}}_{\Omega_{\text{Raman}}} = 10\%$ of the nominal value.

4. **Shot-to-shot fluctuations**: represent stochastic deviations drawn independently for each pulse:

(a) **Raman difference frequency**: we consider Gaussian fluctuations with standard deviation $\sigma^{\text{shot}}_{\omega_{\text{Raman}}} = 30\,\text{Hz}$,

(b) **Reduced Rabi frequency**: we consider Gaussian fluctuations with standard deviation of $\sigma^{\text{shot}}_{\Omega_{\text{Raman}}} = 1\%$ of the nominal value.

The Bayesian model needs to take into account these imperfections in order to handle the possibility that 0/1 outcomes are indeed real, that excitation probabilities are lower than expected, or that the pulses drive neighboring signature transitions: for these reasons, different strategies have been implemented.

The first strategy consists of incorporating false negatives and positives into the update of the prior knowledge about the system. The likelihoods must account for the fact that observing a 1 does not guarantee excitation, and viceversa:

$$\begin{aligned} \mathscr{L}_0 &\longmapsto (1 - p_{\text{fn}})\mathscr{L}_0 + p_{\text{fp}}\mathscr{L}_1, \\ \mathscr{L}_1 &\longmapsto p_{\text{fn}}\mathscr{L}_0 + (1 - p_{\text{fp}})\mathscr{L}_1. \end{aligned} \tag{5.19}$$

The updated $\mathscr{L}_1$ is composed not only of (modulated) off-diagonal terms but also of small diagonal elements, and the updated $\mathscr{L}_0$ not only of (modulated) diagonal terms but also of small off-diagonal terms. However, this strategy does not allow the Bayesian model to infer whether a particular detected outcome is a real or false signal, but instead makes the assumption that it is a real signal with a lower probability. To solve this problem, we need to implement a second strategy to update the decision making of the measurements to apply in a sequence.
For example, if one drives a signature transition for a given manifold J at $\Delta m = -1$, $\mu_J^- \in \mathscr{P}_-$, obtaining a 0/1 outcome, in order to be sure that outcome is indeed real we can drive the same signature transition back at $\Delta m = +1$, $\mu_J^+ \in \mathscr{P}_+$: the second outcome could either confirm the previous outcome or deny it providing the opposite result. Following this reasoning we can build a priori ad-hoc "blocks" of measurement pulses which, fixing the manifold J, drive back and forth the signature transition of that manifold. The aim of these blocks is to strengthen the knowledge about the state distribution of a given manifold, basing on the fact that repeated false outcomes are progressively unlikely.

To determine the presence of the molecule in one manifold, we define different *blocks* according to the number and sequence of the applied measurements, where μ_J^- is labeled as "$-$" and μ_J^+ as "$+$":

Block label	Sequence	Size
0	+	1
1	+ − −	3
2	+ − +	3
3	+−	2
4	+ − +−	4
5	+ − − + −−	6
6	+ + + − − − + + +	9
7	+ + + + −− − − + + ++	12
8	+ − + − + − + − +− + − + − + − + − + − +−	24
9	+ + + + − − − − + + ++ − − − − + + + + − − −−	24

Table 5.1: List of measurement blocks used in the Bayesian model. The signature transition at $\Delta m = +1$, μ_J^+, is labeled as "+´´, the one at $\Delta m = -1$, μ_J^-, as "−´´.

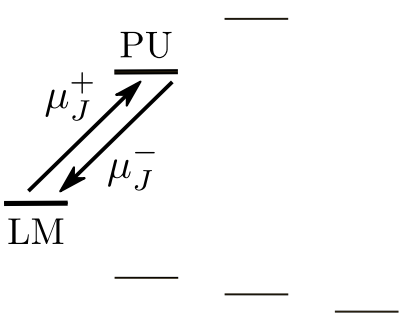

Figure 5.1: For a given manifold J, schematic representation of the driven signature transition inside a block, μ_J^- at $\Delta m = -1$ and μ_J^+ at $\Delta m = +1$.

It is also possible to compare different blocks in terms of the success rate of the state estimation and the overall estimation performance.

To deal with parameter fluctuations, other strategies can be implemented. We need to build a more robust Bayesian model to take into account that the Raman difference frequency and reduced Rabi frequency values are shifted according to the given Gaussian distribution. Thus, we apply the *marginalization* of the likelihoods according to the distribution of the noisy parameters:

$$\begin{aligned} \mathscr{L}_0 &= \int_\Omega \mathscr{L}_0(\Omega) P(\Omega) d\Omega, \\ \mathscr{L}_1 &= \int_\Omega \mathscr{L}_1(\Omega) P(\Omega) d\Omega, \end{aligned} \tag{5.20}$$

where Ω represents the noisy parameters, in our context the Raman difference frequency and the reduced Rabi frequency $(\omega_{\text{Raman}}, \Omega_{\text{Raman}})$, and $P(\Omega)$ the corresponding probability distribution.

Fortunately, Rabi frequency fluctuations only slightly impact the transition excitation probabilities, producing small variations in terms of amplitudes and π-times; hence, it can be neglected to simplify likelihood computation. Conversely, Raman difference frequency fluctuations cause two main issues: first, they heavily reduce the amplitudes of

the Rabi oscillations, especially when the Rabi frequency is small in comparison; second, neighboring signature transitions can be increasingly off-resonant driven. This is particularly true for the $^{40}CaOH^{+}$ lower-J manifolds where the signature transitions are $\sim 100\,\mathrm{Hz}$ apart.
We thus reduce the noisy parameter space to consider Raman frequency difference fluctuations only, and the likelihood marginalization is simplified with a proper discretization to:

$$\begin{aligned}\mathscr{L}_0 &= \sum_{\omega_{\mathrm{Raman}}} \mathscr{L}_0(\omega_{\mathrm{Raman}})P(\omega_{\mathrm{Raman}}),\\ \mathscr{L}_1 &= \sum_{\omega_{\mathrm{Raman}}} \mathscr{L}_1(\omega_{\mathrm{Raman}})P(\omega_{\mathrm{Raman}}).\end{aligned} \tag{5.21}$$

Computed as a weighted mean, the marginalized likelihoods preserve the normalization condition:

$$\begin{aligned}\sum_i (\mathscr{L}_0 + \mathscr{L}_1)_{ij} &= \sum_i \sum_{\omega_{\mathrm{Raman}}} P(\omega_{\mathrm{Raman}})\,(\mathscr{L}_0(\omega_{\mathrm{Raman}}) + \mathscr{L}_1(\omega_{\mathrm{Raman}}))_{ij}\\ &= \sum_{\omega_{\mathrm{Raman}}} P(\omega_{\mathrm{Raman}}) \sum_i (\mathscr{L}_0(\omega_{\mathrm{Raman}}) + \mathscr{L}_1(\omega_{\mathrm{Raman}}))_{ij}\\ &= \sum_{\omega_{\mathrm{Raman}}} P(\omega_{\mathrm{Raman}}) = 1.\end{aligned} \tag{5.22}$$

Indeed, the weighted average of a probability vector, where the weights are probabilities, is itself a probability vector.
We consider two different sources of errors for the Raman difference frequency, miscalibration and shot-to-shot fluctuations, and both contributions are considered in the marginalization process. Since both contributions are Gaussian, the Raman frequency difference distribution $P(\omega_{\mathrm{Raman}})$ is Gaussian as well with standard deviation:

$$\sigma^{\mathrm{tot}}_{\omega_{\mathrm{Raman}}} = \sqrt{\left(\sigma^{\mathrm{mis}}_{\omega_{\mathrm{Raman}}}\right)^2 + \left(\sigma^{\mathrm{shot}}_{\omega_{\mathrm{Raman}}}\right)^2}, \tag{5.23}$$

hence $P(\omega_{\mathrm{Raman}}) \sim \mathcal{N}(\omega_{\mathrm{Raman}}, \sigma^{\mathrm{tot}}_{\omega_{\mathrm{Raman}}})$.

5.2.3 Off-resonant coupling

The experimental design ξ not only includes the type of measurement pulses (signature transitions) and their sequence, but also the reduced Raman Rabi frequency Ω_{Raman}. The choice of the reduced Rabi frequency depends on several factors, primarily the type of molecular ion under consideration and the structure of its internal energy levels.

The $^{40}CaOH^+$ signature transition frequencies overlap in terms of frequency: instead of driving the expected J-th signature transition, the given measurement pulse $\mu_J^{\pm}$ (as defined in Figure 5.1) could drive neighbouring signature transitions. This effect would reduce the selectivity of the measurement pulse.
For $^{40}CaOH^+$, we consider a constant reduced Rabi frequency $\Omega_{\text{Raman}} = 5\,\text{kHz}$. We drive the measurement pulse for manifold J at $\Delta m = +1$, μ_J^+, and compute the excitation probabilities for the signature transitions of all manifolds, analyzing the pulse selectivity. Repeating the procedure for all measurement pulses, we report the results in the heatmap shown in Figure 5.2a. The lower-J measurement pulses off-resonantly drive neighboring transitions with significant probabilities.
To improve the selectivity, the reduced Rabi frequency should be decreased. Thus, we use a J-dependent reduced Rabi frequency defined over three intervals:

$$\Omega_{\text{Raman}}(J) = \begin{cases} \Omega_1 = 0.1\,\text{kHz}, & 1 \leq J \leq 10, \\ \Omega_2 = 1\,\text{kHz}, & 11 \leq J \leq 36, \\ \Omega_3 = 5\,\text{kHz}, & 37 \leq J \leq 50. \end{cases} \tag{5.24}$$

We then repeat the procedure to construct the excitation probability heatmap using the J-dependent reduced Rabi frequency and show the result in Figure 5.2b: the measurement pulse now only excites the desired signature transition. The $^{40}CaH^+$ molecule

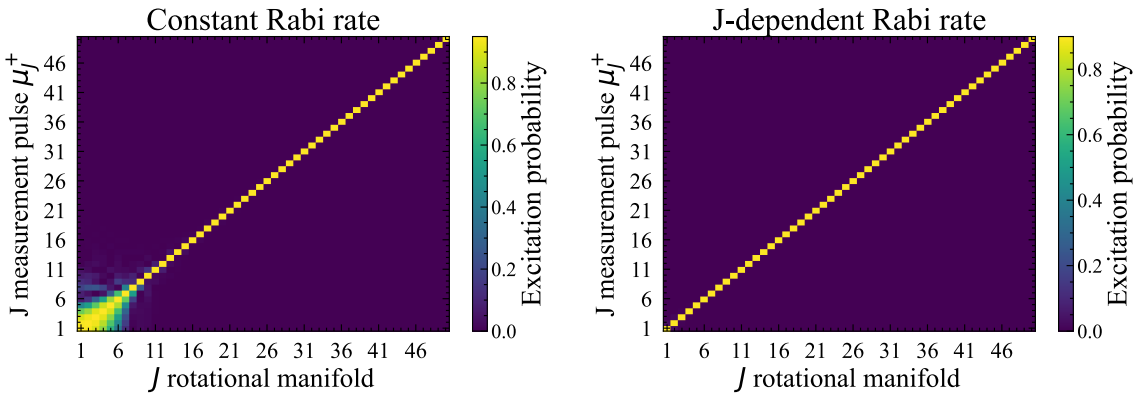

(a) Constant Ω_{Raman} **(b)** J-dependent Ω_{Raman}.

Figure 5.2: Excitation probability heatmap of the measurement pulses at $\Delta m = +1$, μ_J^+, for signature transition of different rotational manifolds J, for $^{40}CaOH^+$ with constant (left) and J-dependent (right) reduced Rabi frequencies

does not possess closely-spaced signature transition frequencies, and already with a constant reduced Rabi frequency $\Omega_{\text{Raman}} = 2\,\text{kHz}$ the measurement selectivity is satis-

fied, as shown in Figure 5.6. Furthermore, measurement pulses must be designed such

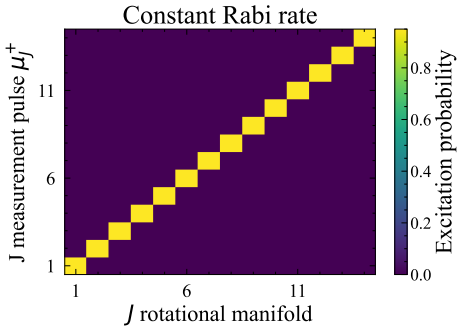

Figure 5.3: Excitation probability heatmap of the measurement pulses at $\Delta m = +1$, μ_J^+, for signature transition of different rotational manifolds J, for $^{40}CaH^+$ with $\Omega_{Raman} = 2\,kHz$.

that their durations are sufficiently short with respect to the heating rate $\Gamma_{heating} \simeq 1 phonon/s$. For this reason, the reduced Rabi frequency cannot be decreased arbitrarily, as it is inversely proportional to the π-time. With a constant reduced Rabi frequency $\Omega_{Raman} = 0.1\,kHz$ for the $^{40}CaOH^+$ molecule, the π-times range from 25 ms ($J = 1$) to 597 ms ($J = 50$). Considering the J-dependent reduced Rabi frequency of Eq. (5.24) would be beneficial since the π-times would become:

$$\begin{aligned} &\text{from } 25\,ms \text{ to } 52\,ms \quad \text{between } J = 1 - 10, \\ &\text{from } 6\,ms \text{ to } 40\,ms \quad \text{between } J = 11 - 36, \\ &\text{from } 8\,ms \text{ to } 12\,ms \quad \text{between } J = 37 - 50, \end{aligned} \tag{5.25}$$

significantly smaller than $\Gamma_{heating}$.
With a constant reduced Rabi frequency $\Omega_{Raman} = 2\,kHz$ for the $^{40}CaH^+$ molecule, the π-times range from 2.6 ms ($J = 1$) to 19 ms ($J = 14$): since only 14 rotational levels are occupied at room temperature the pulse duration requirement is already satisfied.

The reduced Rabi frequency value also influences the off-resonant coupling process. This mechanism comes from coupling a given state to a higher motional state before the motion is cooled away: the result is the $\sigma^-\pi$ Raman beams being able to drive transitions to more distant states, for example between $|J, m\rangle|n = 0\rangle \rightarrow |J, m+1\rangle|n = 1\rangle \rightarrow |J, m+2\rangle|n = 2\rangle \overset{\text{cooling}}{\longrightarrow} |J, m+2\rangle|n = 0\rangle$.
The strength of the off-resonant coupling depends on the reduced Rabi frequency: the larger Ω_{Raman} (i.e., increasing the laser power) the stronger the off-resonant coupling becomes. Indeed, increasing the Rabi frequency $\Omega_{ab} = c_{ab} \cdot \Omega_{Raman}$ with respect to the frequency detuning of the unwanted off-resonant transition reduces the effective fre-

quency discrimination between adjacent transitions.
Therefore, when designing the measurement pulses we must guarantee both the selectivity of the targeted manifold J and a negligible off-resonant coupling.
As an illustrative example, we examine the off-resonant coupling of the measurement pulses with $\Delta m = +1$, μ_J^+, initializing the molecule either in the $|\mathrm{LM}\rangle$ state or in the $|\mathrm{PU}\rangle$ state. As shown in Figure 5.4, starting from the $|\mathrm{LM}\rangle$ state allows us to analyze the population transfer of the most relevant off-resonant transition $|\mathrm{LM}\rangle = |J, -J - 1/2, -\rangle \rightarrow |J, -J + 3/2, -\rangle$; instead, preparing the system in the $|\mathrm{PU}\rangle$ state, we study the excitation of the most significant unwanted off-resonant transition $|\mathrm{PU}\rangle = |J, -J + 1/2, -\rangle \rightarrow |J, -J + 3/2, -\rangle$. Using the J-dependent reduced Rabi frequency Ω_{Raman} of Eq. (5.24) for

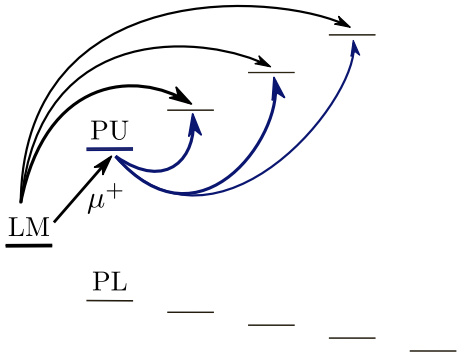

Figure 5.4: Off-resonant coupling transitions from $|\mathrm{LM}\rangle$ (black arrows) and $|\mathrm{PU}\rangle$ states (blue arrows) when driving the measurement pulses at $\Delta m = +1$, μ_J^+.

the $^{40}\mathrm{CaOH}^+$ molecule, we show the population heatmaps of the two most relevant off-resonant scenarios in Figures 5.5a and 5.5b. Conversely, using $\Omega_{\mathrm{Raman}} = 2\,\mathrm{kHz}$ for the

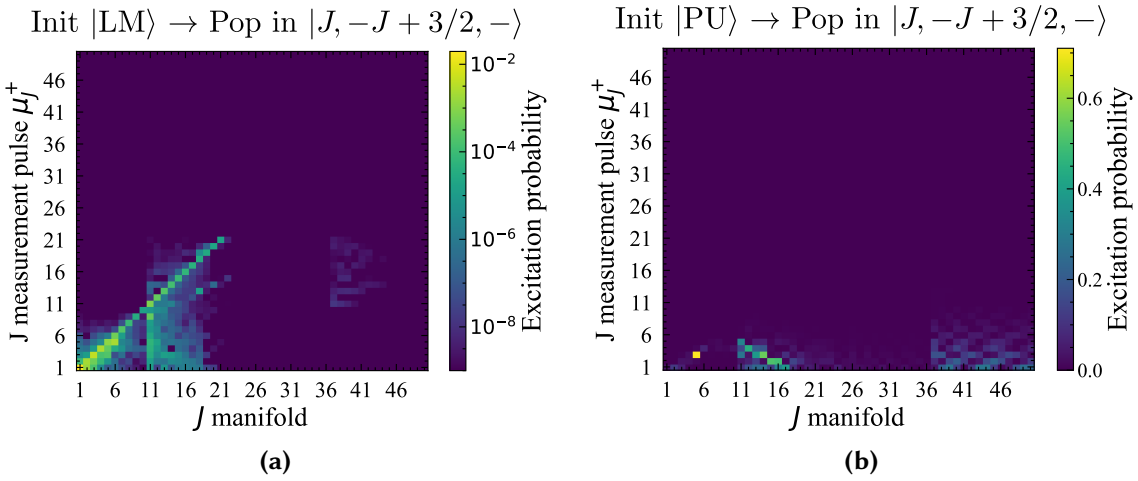

Figure 5.5: Excitation probabilities of the two most relevant off-resonant scenarios when driving the $^{40}\mathrm{CaOH}^+$ measurement pulses at $\Delta m = +1$, μ_J^+, for different manifolds J.

$^{40}CaH^+$, the correspondent results are shown in Figures 5.6a and 5.6b. In the most rele-

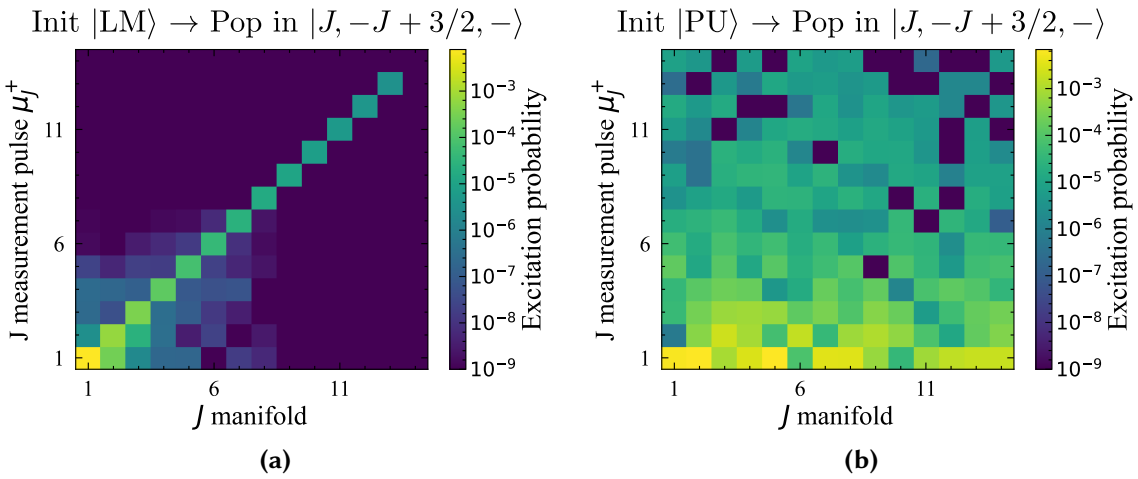

Figure 5.6: Excitation probabilities of the two most relevant off-resonant scenarios when driving the $^{40}CaH^+$ measurement pulses at $\Delta m = +1$, μ_J^+, for different manifolds J.

vant off-resonant transitions driven by the measurement pulses, the population transfer is negligible, allowing us to neglect the off-resonant coupling effect with these reduced Rabi frequency values. Other off-resonant transitions to more distant states are therefore expected to have a smaller impact than the transitions analyzed here. However, increasing Ω_{Raman} would significantly increase the excitation probabilities of many off-resonant transitions.

Following the assumptions and reasoning outlined in Chapter 3, the physics simulator is a classical probabilistic model, which simulates only populations and neglects coherences. With the aim of decreasing computational costs, we are only generating statistical mixtures of states. Additionally, using the $\sigma^-\pi$ Raman beam to drive blue-sideband transitions, we introduce directionality of the transitions to either $\Delta m = -1$ or $\Delta m = +1$.

Thus, neglecting the off-resonant coupling mechanism, each molecular state $|J, m, \pm\rangle$ can only undergo two transitions to $|J, m + \Delta m, -\rangle$ and $|J, m + \Delta m, +\rangle$ (if those final states exist). As motivated by the discussion in Chapter 3, at most one of the two transitions is in resonance, while the other one is adiabatically eliminated.

As a consequence, we can treat the direct transitions as two separated 2-level systems and individually compute their excitation probabilities, respectively $p_{i\rightarrow f_1}$ and $p_{i\rightarrow f_2}$. These two transitions represent two *mutually exclusive events*, since at most one transition can happen, thus making the probability a given state is not excited $p_{i\rightarrow i} =$

$1 - p_{i\to f_1} - p_{i\to f_2}$. Adiabatic elimination ensures that $p_{i\to i} \leq 1$.
Due to these considerations, the transition matrices and hence the likelihoods are significantly simplified. Following Eq. (5.7), each column of the T matrix only contains two off-diagonal elements and one diagonal element. Such a sparse matrix considerably reduces the computational costs associated to build the transition matrices, likelihoods, and matrix-vector multiplications.

Finally, the reduced Rabi frequency influences the impact of the experimental imperfections on the Bayesian state estimation.
Driving a measurement pulse μ_J on resonance with the signature transition of J manifold, the Raman detuning fluctuations make the pulse off-resonant by Δ. With a reduced Raman Rabi frequency $\Omega_{\text{Raman}} = 1\,\text{kHz}$, the effective Rabi frequency becomes $\Omega_{\text{ab}} = c_{\text{ab}}\Omega_{\text{Raman}} \sim 0.01 \cdot 1\,\text{kHz} = 10\,\text{Hz}$.
Since the Rabi oscillation contrast of the transition follows Eq. (2.6), even a slight detuning of $\Delta = 10\,\text{Hz}$ halves the contrast. The system is much more sensitive to the experimental imperfections as Ω_{Raman} increases. Moreover, the signature transition coupling coefficients depend on the manifold, ranging from 0.2 ($J = 1$) to 0.008 ($J = 50$) for the $^{40}\text{CaOH}^+$ molecule.
When choosing the reduced Rabi frequency values, the trade-offs associated with these variables and mechanisms must be taken into account:

- Increasing Ω_{Raman}. Pros: less sensitive to experimental imperfections. Cons: off-resonant transitions are excited; signature transition selectivity is lost as excitation can be driven from a range of neighboring manifolds.

- Decreasing Ω_{Raman}. Pros: off-resonant coupling is not driven; signature transition selectivity is satisfied. Cons: more sensitive to experimental imperfections.

These conditions also depend on the molecular species. For $^{40}\text{CaH}^+$, we can almost achieve a "free lunch" by using a constant reduced Rabi frequency of $\Omega_{\text{Raman}} = 2\,\text{kHz}$. In contrast, for $^{40}\text{CaOH}^+$ the J-dependent reduced Rabi frequency defined in Eq. (5.24) is required to optimally satisfy all constraints: some compromises are unavoidable, and still exhibit a strong sensitivity to the experimental imperfections, especially for lower-J manifolds.

5.3 Bayesian estimator and Bayesian simulator

The Bayesian state estimation model is implemented inside the so-called *inference evaluator module*. This framework contains two classes which have distinct roles and functionalities: the *Bayesian estimator* (BE) and the *Bayesian simulator* (BS). A schematic representation of how the different components interact is shown in Figure 5.7.

The BS simulates the physical world, representing the physical dynamics of the system

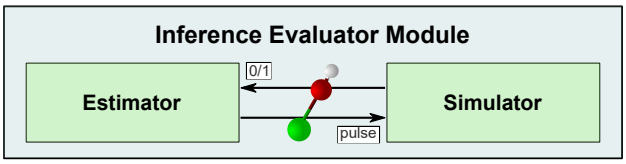

Figure 5.7: Schematic representation of the Bayesian framework in a static state estimation process.

within the approximations mentioned above. Specifically, it depicts the trapped molecular ion's state, selected from the thermal distribution at room temperature after an eventual state preparation procedure. The BS also implements transitions and, subject to the interaction with the motional-adding sideband CW Raman pulses, it follows the evolution of the molecular state, updating its own state accordingly and providing the 0/1 outcome.

Containing the realistic model of the physical system, the BS should include the experimental imperfections: it feels fluctuated Raman frequency and Rabi frequency values and switches the outcomes according to the false negative and positive rates.

On the other hand, the BE simulates the control system of the experiment which implements the Bayesian algorithm to infer the molecular state.

The BE has only limited knowledge of the system, representing the perspective of an external observer. The initial state distribution is the thermal distribution at room temperature updated with an eventual state preparation scheme. It builds the set of measurement pulses to drive and at each step updates the prior knowledge based on the provided 0/1 outcomes using the Bayes' theorem.

The BE is unaware of the precise values of the experimental imperfections, but only knows their distributions based on educated guesses. In order to make more robust estimations, it uses the three strategies previously described.

Assuming that the molecule lies in state $s_i = S_i$ at step t, the Bayesian simulator probability state distribution is a Kronecker delta peaked at s_i:

$$p^{\mathrm{BS}} = P^{(t)}(s) = \delta_{s,s_i}. \tag{5.26}$$

Conversely, the Bayesian estimator at step t computes the posterior

$$q^{\mathrm{BE}} = P^{(t)}(s|m_k^{(t)}, \xi). \tag{5.27}$$

With the aim of quantifying how close the Bayesian estimator is in correctly inferring the molecular state, we define a metric called *cross-entropy*. Cross-entropy measures the difference between two probability distributions, a true distribution and an estimated one. In our context, it is computed between the BS and BE probability distributions as:

$$H(p^{\mathrm{BS}}, q^{\mathrm{BE}}) = -\sum_j p_j^{\mathrm{BS}} \log q_j^{\mathrm{BE}} = -\log q_i^{\mathrm{BE}}. \tag{5.28}$$

This means that to compute the cross-entropy we only need the BE posterior entry corresponding to the i-th state in which the molecule lies. Hence, $H(p^{\mathrm{BS}}, q^{\mathrm{BE}})$ value is unknown to the BE, since it is unaware of molecule's state, but it can be calculated by the external inference evaluator module as an accuracy metric for the Bayesian algorithm. Note that when the true distribution is a Kronecker delta, the cross-entropy becomes equivalent to the Kullback-Leibler (KL) divergence:

$$D_{KL}(p^{\mathrm{BS}} \| q^{\mathrm{BE}}) = \sum_j p_j^{\mathrm{BS}} \log \frac{p_j^{\mathrm{BS}}}{q_j^{\mathrm{BE}}} = -\log q_i^{\mathrm{BE}} = H(p^{\mathrm{BS}}, q^{\mathrm{BE}}). \tag{5.29}$$

Low $H(p^{\mathrm{BS}}, q^{\mathrm{BE}})$ values imply high q_i^{BE} values, indicating that the posterior is more concentrated on the actually occupied states and therefore that the BE is correctly performing state estimation.
The Bayesian estimator computes the variance of the posterior distribution:

$$\sigma^2 = \mathrm{Var}_{q^{\mathrm{BE}}}[s] = \left(\sum_s s^2 \cdot q^{\mathrm{BE}}(s) \right) - \left(\sum_s s \cdot q^{\mathrm{BE}}(s) \right)^2. \tag{5.30}$$

The variance denotes how broad the probability distribution is, and therefore how well-known the inferred state is.

The Bayesian state estimation process is implemented in a dedicated algorithm, schematically described in Appendix D. The code is available in Appendix E.
At the beginning, the function `molecule_state_preparation` builds the molecular ion data, such as the `state_df` and `transition_df` dataframes that contain the

ensemble of molecular states and the possible transitions, as described in Chapter 3; moreover, the molecular probability state distibution after the state preparation stage, $P_{\text{s.p.}}(s)$, is computed, as well as the J-thermal distribution P_J. These are calculated with respect to the temperature T, magnetic field B, and the state preparation efficiencies η obtained after the analysis in Chapter 4.

A second function `BE_initialization` creates the Bayesian estimator, by setting the initial prior $P_{\text{BE}}^{(0)}(s)$ equal to the molecular state distribution after the state preparation scheme. A third function `BS_initialization` extracts the initial state for the BS, $|J, m, \xi\rangle_{\text{BS}}^{(0)}$, according to the thermally-distributed J and the corresponding ξ and m state distribution after the state preparation. Then, the ensemble of measurements is computed by the function `measurement_setting`: considering the molecular parameters and the fixed experiment design ξ (that also includes the reduced Raman Rabi frequency Ω_{Raman}), the pulse parameters are built using Eq. (5.16). The marginalization strategy can be applied with respect to the set of experimental imperfections $\epsilon = \left(p_{\text{fn}}, p_{\text{fp}}, \sigma_{\omega_{\text{Raman}}}^{\text{mis}}, \sigma_{\omega_{\text{Raman}}}^{\text{shot}}, \sigma_{\Omega_{\text{Raman}}}^{\text{mis}}, \sigma_{\Omega_{\text{Raman}}}^{\text{shot}}, \sigma_{\omega_{\text{Raman}}}^{\text{tot}}\right)$. Each measurement pulse $\mu \in \mathscr{P}$ is associated to the 0 and 1 outcome likelihoods, ${\mathscr{L}_0}^{\mu}$ and ${\mathscr{L}_1}^{\mu}$ respectively.

The core of the Bayesian model lies in the `update_distribution` function. Each step t in the update loop corresponds to a single experimental step involving the application of a Raman measurement pulse μ. The BE chooses the next measurement pulse to apply according to the a priori chosen design ξ and the type of *block*: in the context of static state estimation, we sweep the manifolds to query, and for each manifold J we apply the signature transition pulse sequence established by the block type.

At the beginning of each iteration, the BE evaluates whether to apply optical pumping according to the variance of its posterior distribution: when the knowledge of the molecular state is deemed sufficiently low by the BE, it performs optical pumping updating the BE posterior accordingly.

Subsequently, the index of the measurement pulse to apply in the current iteration is extracted, and the transition matrix T corresponding to the measurement pulse is computed following Eq. (5.7). Since the BS lies in the k-th state at step t, we extract the k-th column of the transition matrix, $T_{*,k}$, obtaining a probability distribution $\pi(s)$: the new BS state at step $t+1$ is sampled from it. The outcome is then provided taking into account the false positive and negative rates, and the BE posterior ${q^{\text{BE}}}^{(t+1)}$ is updated using Bayes' theorem.

Cross-entropy between BS and BE probability distributions is computed using Eq. (5.28). The following stopping condition is adopted: if there exists a state s such that the corresponding entry of the BE posterior ${q^{\text{BE}}}^{(t+1)}(s)$ exceeds 0.9, the algorithm stops, consid-

ering s as the inferred molecular state.
Finally, the function `Bayesian_state_estimation` implements the Monte Carlo approach. In each of the N independent simulation runs, the initial BS state is randomly sampled according to the state preparation probability distribution. Then, the function `update_distribution` is called, and the history of results is collected.

5.4 Monte Carlo simulations and results

We apply the Bayesian state estimation algorithm to the $^{40}CaH^+$ molecule at $B = 3.6\,G$ at room temperature $T = 300\,K$, after the state preparation stage explained in Chapter 4 which pumps the population of each manifold in its target state, with residual population in the leftmost (LM), penultimate upper (PU), and penultimate lower (PL) states. We consider the experimental imperfections values listed in Section 5.2.2, $N = 2000$ independent simulation runs in the Monte Carlo approach, each made of 300 steps, and reduced Rabi frequency $\Omega_{\text{Raman}} = 2\,\text{kHz}$. In this first stage, the strategies implemented to overcome the experimental imperfections are not used, and we only sweep the manifolds driving for each one the block 0 measurement pulse. The cross-entropy histories and the final cross-entropy values are shown in Figure 5.8a. Only the 59.2% of the runs successfully infer the molecular state: their final cross-entropy (once they reach the stopping condition or the final step) is below the threshold corresponding to $p = 0.9$. Most failed runs saturate the cross-entropy, inferring a "wrong" state due to the false negative and positive rates. The same algorithm without strategies to mitigate experimental imperfections is then applied to the $^{40}CaOH^+$ molecule at $B = 3.27\,G$ and $T = 300\,K$ after the state preparation stage, with Ω_{Raman} following Eq. (5.24), and $N = 2000$ runs each of 1800 steps. The cross-entropy histories and the final cross-entropy values are shown in Figure 5.8b.
In this case the success rate is lower, at 12.5%, consistent with $^{40}CaOH^+$ having a more complex structure and hence the state is more difficult to infer.

Next we apply the Bayesian state algorithm implementing the strategies to mitigate the presence of false positives and negatives, such as the *block* implementation and the computation of the likelihoods with false-rate corrections following Eq. (5.19).
Using *Block 3* as a representative example, in Figure 5.9a we show the cross-entropy histories and the final entropy values for the $^{40}CaH^+$ molecule where the success rate is about 84.6%. Additionally, the distribution of the convergence steps, the final BE pos-

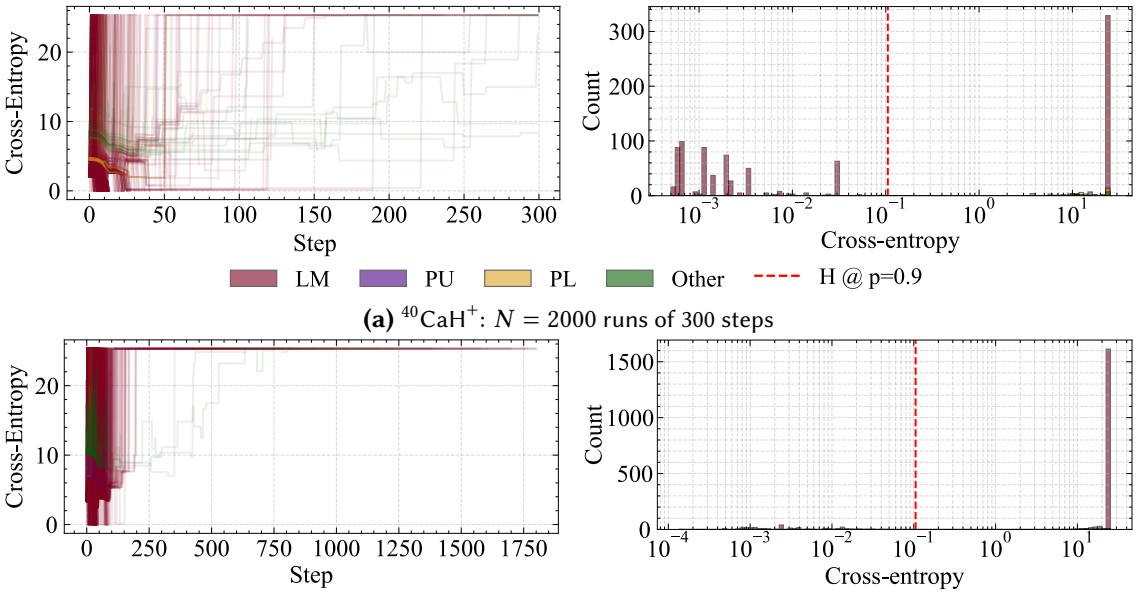

(a) $^{40}CaH^+$: $N = 2000$ runs of 300 steps

(b) $^{40}CaOH^+$: $N = 2000$ runs of 1800 steps

Figure 5.8: Bayesian state estimation results without strategies to mitigate experimental imperfections, with block 0 measurement pulse. Cross-entropy histories and final cross-entropy values are shown for $^{40}CaH^+$ and $^{40}CaOH^+$ divided between the initialization in the LM, PU, PL or other states.

terior variance, and the fluctuated Raman detunings are displayed in Figures 5.9b, 5.9c, and 5.9d, respectively.

Most successful runs have a variance below a certain threshold (~ 2500), which will be used later as a criterion to perform optical pumping. At each manifold sweep, if the posterior variance is above this threshold, the BE performs optical pumping. Furthermore, most unsuccessful runs are non-converging runs, while successful ones are located in the region where experimental fluctuations are lower.

Finally, it is possible to compare the different *blocks* in terms of success rate and convergence steps for $^{40}CaH^+$. The confidence intervals and medians are shown in Figures 5.10: the block's success rate increases to around $80 - 85\%$, showing that these techniques already produce improved results.

Analogously, it is possible to repeat the analysis for the $^{40}CaOH^+$ molecule, providing the cross-entropy histories and the final entropy values in Figure 5.11a using *Block 7* as a representative example. In this case the success rate is about 32.2% : again, with $^{40}CaOH^+$ the performances are lower. Additionally, we provide in Figure 5.11b the distributions of the BE posterior variance at convergence and the distributions of successes and failures over the deviations in the Raman detunings, respectively. The variance

threshold between success and failure estimations is $\sim 1.5 \cdot 10^5$. The efficiency comparison of the blocks for $^{40}CaOH^+$ are shown in Figure 5.12: the success rate is around $30 - 35\%$, which could be improved further.

Ultimately, we apply the strategies to overcome Raman detuning miscalibrations, thus implementing the optical pumping process when the variance exceeds the threshold, and the marginalization of the likelihoods. A preliminary analysis shows that the standard deviation of the Gaussian distribution of Raman frequencies for the marginalization of likelihoods must be slightly lower than the $\sigma^{\text{tot}}_{\omega_{\text{Raman}}}$ used by the BS. For this reason we use $\sigma = 30\,\text{Hz}$ for likelihoods marginalization.
We first apply the Bayesian algorithm in the final version to the $^{40}CaH^+$ molecule, and the block comparison is shown in Figure 5.13: the success rate increased slightly from $80 - 85\%$ to $88 - 90\%$. The algorithm efficiency is very high, due to the simpler molecular structure. One also has to consider that if the molecule lies in manifold $J = 0$, it is impossible to infer it with the σ_π Raman beam configuration, since the two states in this level are not coupled.
The $^{40}CaOH^+$ molecule results are shown in Figure 5.14. In this case, the marginalization technique provides a larger improvement in terms of the success rate, increasing from $30-35\%$ to $45-58\%$. Using *Block 7* as an example, we report the final cross-entropy values, and the distributions of the successes and failures over the deviations in Raman difference frequencies, convergence steps, and final posterior variance in Figures 5.15a, 5.15b, 5.15c and 5.15d, respectively. The successful runs are located in the region where experimental fluctuations are lower, as expected.

Most unsuccessful runs do not reach algorithm convergence, never satisfying the stopping condition. This knowledge is available to the BE: hence, we can discard all non-converging runs. It is possible to analyze the Bayesian algorithm efficiency (comparing the success rates of the blocks) when applying this filtering. For the $^{40}CaOH^+$ molecule, the results for the converging runs are shown in Figure 5.16. The success rate when post-selecting only for converging runs is around $84 - 90\%$: this allows us to claim that the Bayesian state estimation algorithm applied to $^{40}CaOH^+$ molecule converges $\sim 45 - 58\%$ of the time, and when it does, it successfully infers the state $\sim 84 - 90\%$ of the time.
This analysis is not necessary for $^{40}CaH^+$ molecule since efficiencies are already high.

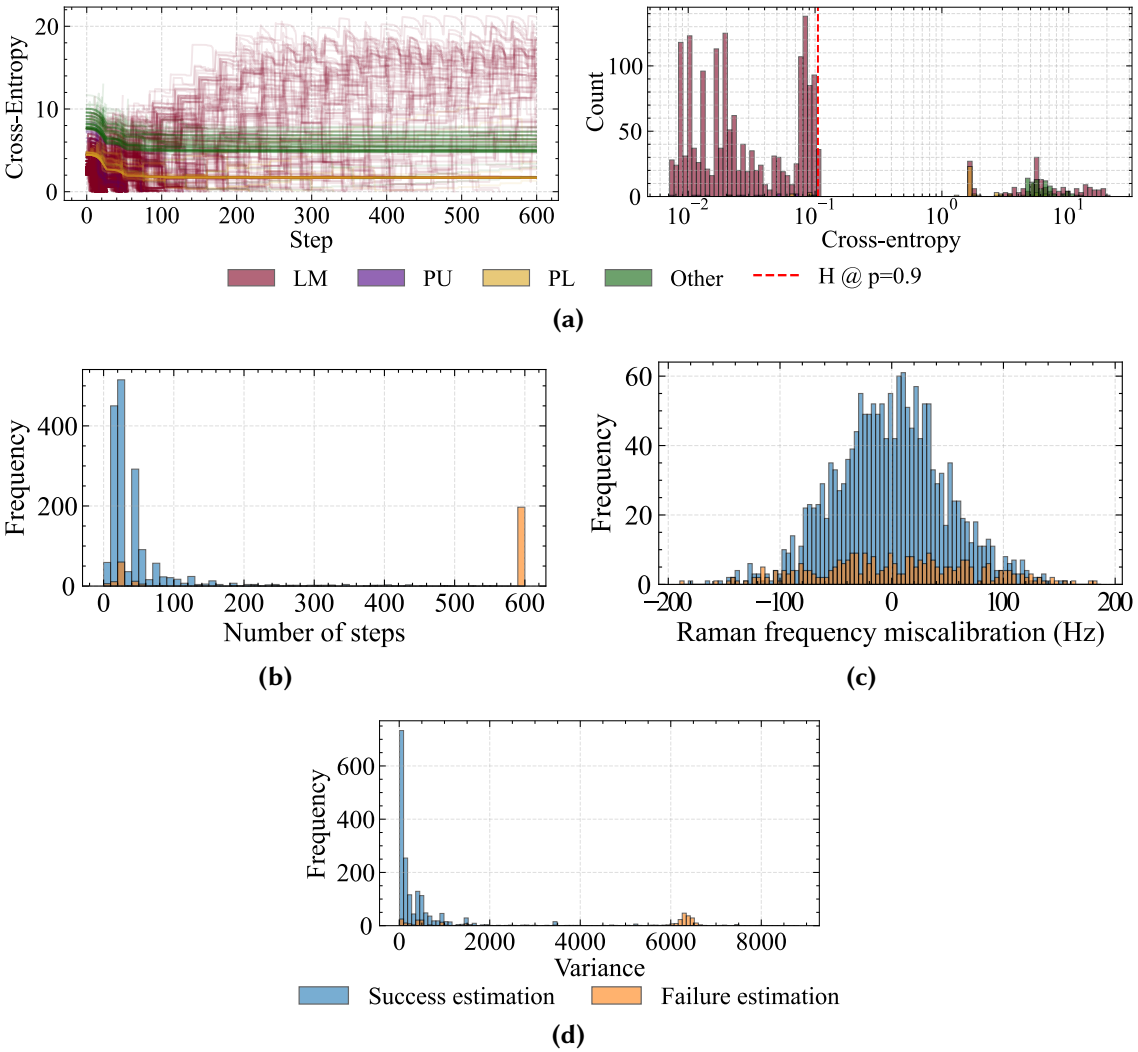

Figure 5.9: $^{40}CaH^{+}$ state estimation with block 3 implementation and false-rate correction. Cross-entropy histories (a), final cross-entropy values (b), distribution of convergence steps (c), final BE posterior variance (d) and deviations in Raman detuning (e) are shown.

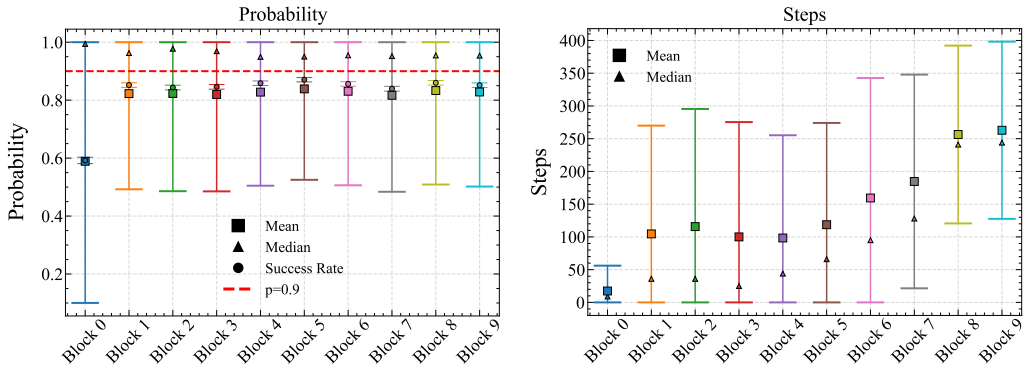

Figure 5.10: $^{40}CaH^{+}$ block comparison with *block* implementation and false-rate correction, in term of success rate and convergence step.

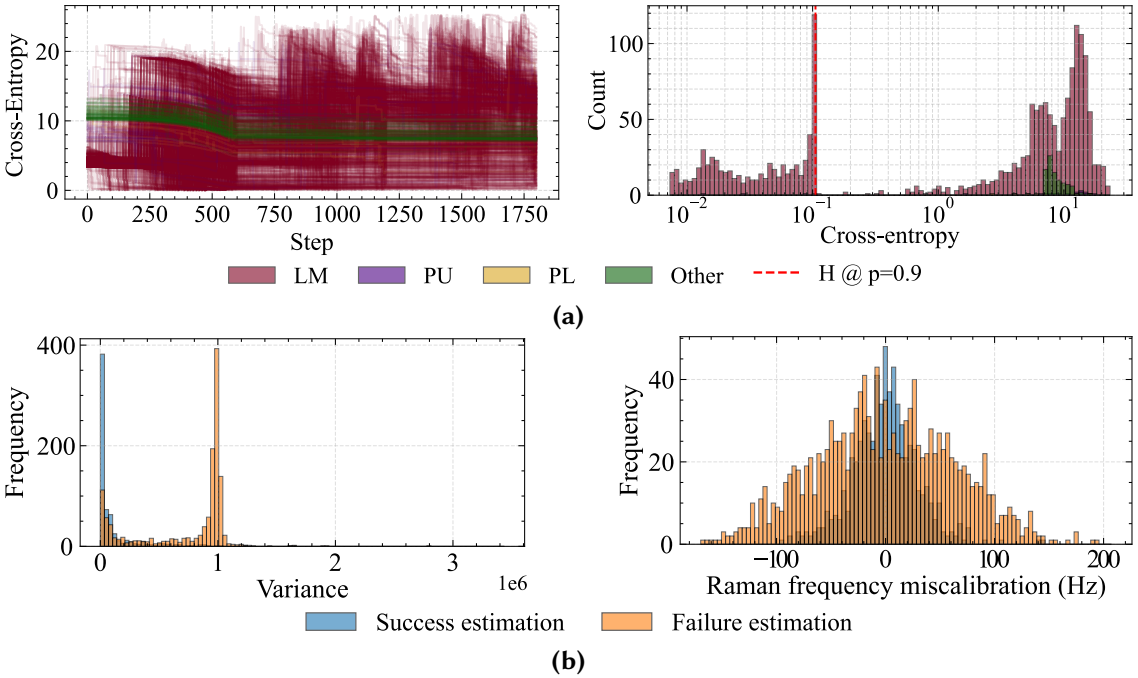

Figure 5.11: $^{40}CaOH^{+}$ state estimation with *Block 7* implementation and false-rate correction. Cross-entropy histories (a), final cross-entropy values (b), distribution of final BE posterior variance (c) and deviations in Raman detuning (d) are shown.

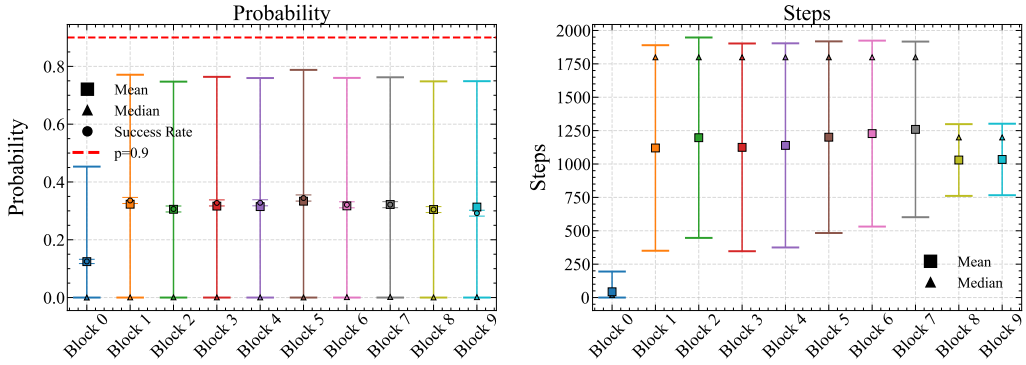

Figure 5.12: $^{40}CaOH^{+}$ block comparison with *block* implementation and false-rate correction, in term of success rate and convergence step.

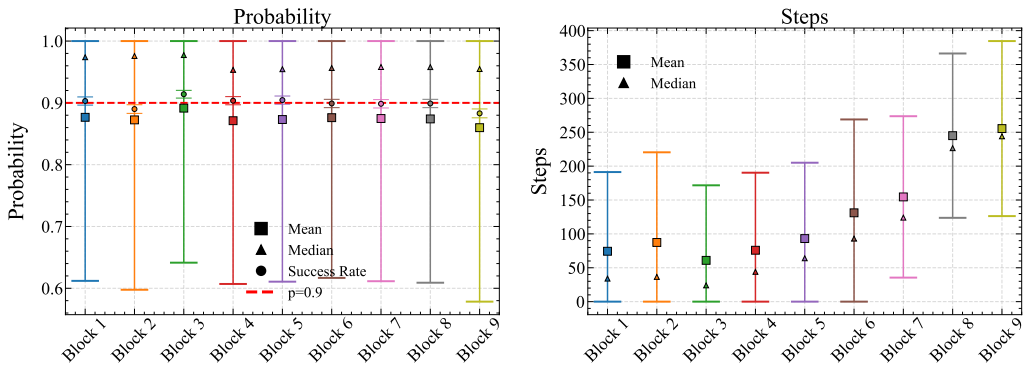

Figure 5.13: $^{40}CaH^{+}$ block comparison with implementations of *block* pulses, false-rate correction, optical pumping and marginalization, in term of success rate and convergence step.

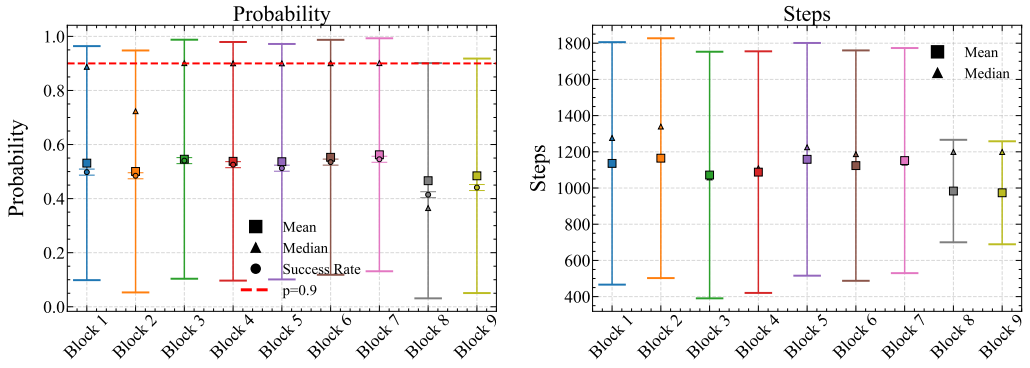

Figure 5.14: $^{40}CaOH^{+}$ block comparison with implementations of *block* pulses, false-rate correction, optical pumping and marginalization, in term of success rate and convergence step.

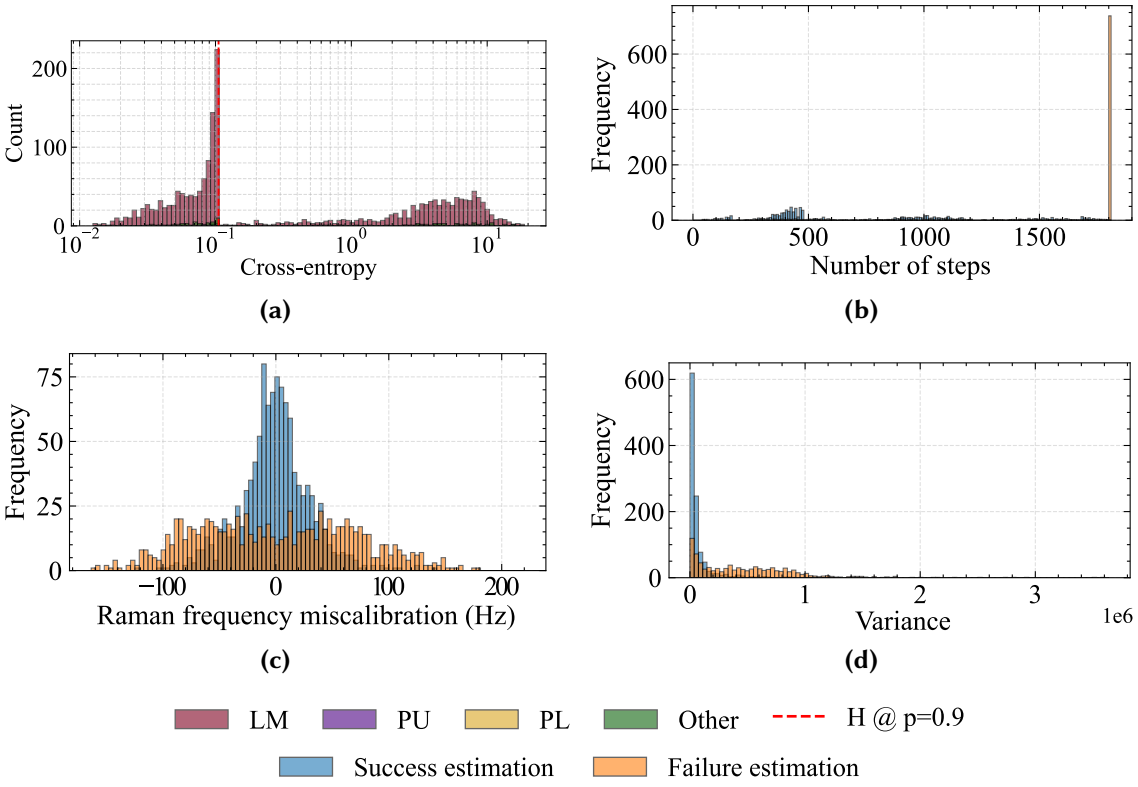

Figure 5.15: $^{40}CaOH^{+}$ state estimation with implementations of *Block 7* pulses, false-rate correction, optical pumping and marginalization. Final cross-entropy values (a), distribution of convergence steps (b), fluctuated Raman detuning (c) and final BE posterior variance (d) are shown.

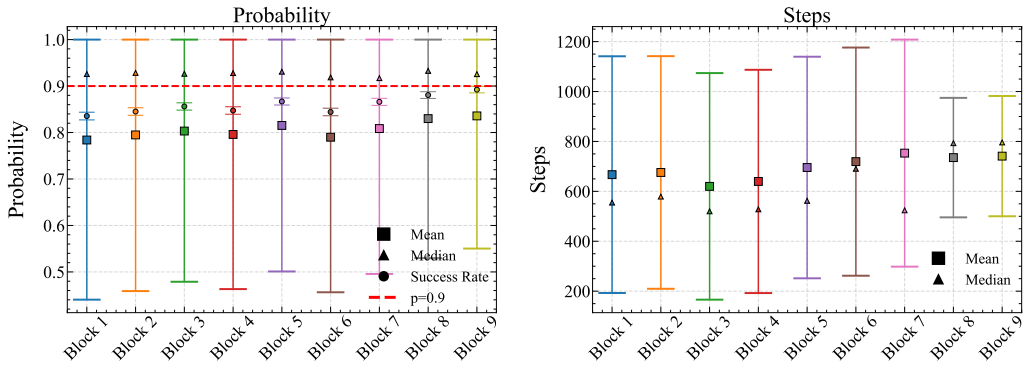

Figure 5.16: $^{40}CaOH^{+}$ block comparison with implementations of *block* pulses, false-rate correction, optical pumping and marginalization, in term of success rate and convergence step. Non-converging runs are traced out, keeping the converging ones.

6

Conclusions

This thesis has developed a comprehensive theoretical and computational framework for the spectroscopy and quantum control of $^{40}CaH^+$ and $^{40}CaOH^+$ molecular ions co-trapped with a $^{40}Ca^+$ logic ion in a linear Paul trap. The work proceeds from the simulation of hyperfine spectra to the design of state preparation protocols and, ultimately, to Bayesian inference of the molecular quantum state from binary QLS measurement outcomes.

A classical probabilistic physics simulator was developed to efficiently model the interaction of the molecular ions with Raman laser fields. The simulator operates under the assumption that the molecular state is a mixed state, due to coherence rapidly being lost due to dissipative interactions, and reduces the multi-state system to a collection of two-state transitions via adiabatic elimination of off-resonant states. The simulator was validated against the experimentally measured hyperfine Raman spectrum of $^{40}CaH^+$. This agreement supports its application to $^{40}CaOH^+$, whose hyperfine spectrum has not yet been experimentally measured. The simulated $^{40}CaOH^+$ spectrum reveals a qualitatively different structure: the two hyperfine peaks are located near zero frequency, and the signature transitions are closely spaced and partially overlapping due to the simultaneous presence of manifolds in the Zeeman, intermediate, and Paschen-Back regimes at the given magnetic field on the order of a Gauss.

A significant practical challenge for $^{40}CaOH^+$ quantum logic spectroscopy is the optical dipole force (ODF), which arises from spurious polarization components in the Raman beams and coherently displaces the motional state without driving internal transitions. Because the $^{40}CaOH^+$ hyperfine peaks lie near zero frequency, they are entirely obscured by the ODF signal under standard QLS conditions. We demonstrated through simulation that neither increasing the magnetic field to push the peaks away from zero nor improving the beam polarization purity to suppress the ODF peak is easily achievable with current experimental constraints. To circumvent this problem, we introduced a loop closing strategy: by choosing a detuning-dependent pulse duration $T = N2\pi/\delta$

and a correspondingly adjusted molecular Rabi frequency $\Omega_{\text{mol}} = \pi/T$, the motional displacement induced by the ODF completes an integer number of loops in phase space, suppressing residual motional excitation. Simulations confirm that this strategy successfully suppresses the ODF signal across the relevant frequency range, making the $^{40}CaOH^+$ hyperfine peaks experimentally accessible.

To enhance the signal-to-noise ratio of the J-dependent signature transitions and enable state identification, a two-stage state preparation protocol was designed. In the first stage, a six-step optical pumping scheme concentrates the population of each rotational manifold into the leftmost, penultimate upper, and penultimate lower states. A key innovation of this scheme is the introduction of a third Raman beam branch with σ^+ polarization, enabling $\Delta m = -2$ transitions that remove population trapped in the central dark states of each sub-manifold — a limitation of the standard two-branch $\sigma^- - \pi$ configuration. In the second stage, Raman-driven rapid adiabatic passage sideband pulses transfer the residual PU and PL population to the target state, acting simultaneously on multiple manifolds in a robust manner. After this combined protocol, the target state is populated with near-unity efficiency across the manifolds of both molecules, and the simulated pumped spectra show clearly resolved signature transition peaks with significantly improved SNR compared to the thermal spectrum.

Finally, a Bayesian inference framework was developed to identify the state of the molecular ion from sequential binary QLS measurement outcomes. The framework consists of a Bayesian estimator (BE), which maintains a probability distribution over molecular states and updates it via Bayes' theorem after each measurement, and a Bayesian simulator (BS), which models the physical dynamics of the system including experimental imperfections. Three complementary strategies were implemented to handle the imperfections: false-rate correction of the likelihoods, block-structured measurement sequences that drive signature transitions back and forth to validate outcomes, and marginalization of the likelihoods over the Raman frequency uncertainty. For $^{40}CaH^+$, the algorithm achieves success rates of 88–90% with a reduced Rabi frequency of $\Omega_{\text{Raman}} = 2\,\text{kHz}$. For $^{40}CaOH^+$, the task is considerably harder due to the overlapping signature transitions and strong sensitivity to experimental imperfections, particularly for low-J manifolds: without mitigation strategies, the success rate is only 12.5%. The introduction of block-structured measurement sequences and false-rate correction raises this to 30–35%, and the further application of likelihood marginalization over the Raman frequency uncertainty yields a final success rate of 45–58%. Among converging runs, the success rate reaches 84–90%. The results of this thesis constitute a solid computational foundation for the experimental realization of QLS-based quantum control

of $^{40}CaH^+$ and $^{40}CaOH^+$. Several directions for future work are immediately apparent. First, the simulated spectra and Bayesian inference results should be compared with experimental data as they become available, in particular for $^{40}CaOH^+$ where the hyperfine parameters c_{IJ} and g_J are currently only theoretically estimated. Once the spectrum is experimentally measured, these parameters can be precisely determined, experimentally validating the theory in the same way that was achieved for $^{40}CaH^+$. Second, the static Bayesian state estimation framework developed here could be extended to Bayesian adaptive experimental design, where the next measurement is chosen to maximize the expected information gain rather than following a fixed schedule. This approach promises significant improvements in convergence speed and estimation efficiency, particularly for the complex $^{40}CaOH^+$ level structure. Computational cost remains a challenge, but could be addressed through deep experiment design — training a neural network to simulate experimental outcomes and optimize measurement strategies in real time. Third, the general architecture of the physics simulator and Bayesian framework is not specific to $^{40}CaH^+$ and $^{40}CaOH^+$: it is designed for any nuclear spin-1/2 linear molecular ion in its $^1\Sigma$ vibronic ground state, and could be directly applied to other molecular species of experimental interest, extending the reach of QLS-based quantum control to a broader class of polyatomic molecular ions.

A

Hyperfine molecular structure

An external magnetic field is applied along a direction labeled $\tilde{z}$, which defines the quantization axis but which does not coincide with the z direction in which the two ions oscillate out of phase.
From the rotational and nuclear spin angular momenta J, I and their projection m_J, m_I (eigenvalues of $\hat{J}_{\tilde{z}}$ and $\hat{I}_{\tilde{z}}$ respectively) it is possible to introduce the total angular momentum $\vec{F} = \vec{I} + \vec{J}$ and its projection $m_F = m_J + m_I$ (eigenvalue of $\hat{J}_{\tilde{z}} + \hat{I}_{\tilde{z}}$).
Using the ladder operator formalism, the hyperfine Hamiltonian of Eq. (2.22) can be rewritten as [9, 10]

$$\hat{H}_{hyp} = -\frac{g_J \mu_N}{\hbar} \hat{J}_{\tilde{z}} B - \frac{g_I \mu_N}{\hbar} \hat{I}_{\tilde{z}} B - \frac{2\pi c_{IJ}}{\hbar} \left[\hat{J}_{\tilde{z}} \hat{I}_{\tilde{z}} + \frac{\hat{J}_+ \hat{J}_- + \hat{J}_- \hat{J}_+}{2} \right] \tag{A.1}$$

since $\hat{J}_{\tilde{x}} \hat{I}_{\tilde{x}} + \hat{J}_{\tilde{y}} \hat{I}_{\tilde{y}} = (\hat{J}_+ \hat{J}_- + \hat{J}_- \hat{J}_+)/2$, where $\hat{J}_\pm |J, m_J\rangle = \hbar \sqrt{(J \mp m_J)(J \pm m_J + 1)} \, |J, m_J \pm 1\rangle$ is valid under the constraint $|m_J| < J$ while in the extreme cases the ladder operators return $\hat{J}_\pm |J, \pm J\rangle = 0$ (same for $\hat{I}_\pm$).
In the non-extreme cases, Equation (A.1) clearly shows that m_F is a *good* quantum number because it is a conserved quantity in the Hamiltonian. Indeed, the Zeeman terms commute with $\hat{J}_{\tilde{z}}$ and $\hat{I}_{\tilde{z}}$, thus they are diagonal in m_J and m_I, and so also for m_F. Considering the less obvious internal coupling part, the term $\hat{J}_{\tilde{z}} \hat{I}_{\tilde{z}}$ is diagonal in m_F for the same above mentioned reason. On the other hand, the term $\hat{J}_+ \hat{J}_- + \hat{J}_- \hat{J}_+$ does not preserve m_I or m_J singularly, but their sum: while the projection of one angular momentum is increased by 1, the other one is decreased by 1, leaving m_F unchanged under the effect $(m_J, m_I) \to (m_J \pm 1, m_I \mp 1)$.
The conservation of m_F and the presence of countersymmetric rotational and nuclear spin ladder operator allows us to write the Hamiltonian in block form (with blocks having dimensions 2x2) for non-stretched states ($|m_F| < J + 1/2$) [9, 10]:

$$\hat{H}_{J,m_F} = \begin{pmatrix} -\left[g_J\left(m_F-\frac{1}{2}\right)+\frac{g_I}{2}\right]\mu_N B & -\frac{hc_{IJ}}{2}\left(J+m_F+\frac{1}{2}\right)^{1/2} \\ -\frac{hc_{IJ}}{2}\left(m_F-\frac{1}{2}\right) & \cdot\left(J-m_F+\frac{1}{2}\right)^{1/2} \\ -\frac{hc_{IJ}}{2}\left(J+m_F+\frac{1}{2}\right)^{1/2} & -\left[g_J\left(m_F+\frac{1}{2}\right)-\frac{g_I}{2}\right]\mu_N B \\ \cdot\left(J-m_F+\frac{1}{2}\right)^{1/2} & +\frac{hc_{IJ}}{2}\left(m_F+\frac{1}{2}\right) \end{pmatrix} \tag{A.2}$$

using the basis:

$$\begin{cases} \hat{e}_0 = \left|J, m_F-\frac{1}{2}\right\rangle\left|\frac{1}{2},\frac{1}{2}\right\rangle \\ \hat{e}_1 = \left|J, m_F+\frac{1}{2}\right\rangle\left|\frac{1}{2},-\frac{1}{2}\right\rangle. \end{cases} \tag{A.3}$$

In order to simplify the notation, we define the following variables:

$$\begin{aligned} X_{J,m_F} &= \frac{1}{2}\sqrt{h^2c_{IJ}^2\left[(J+1/2)^2-m_F^2\right]+\left[hc_{IJ}m_F-(g_J-g_I)\mu_N B\right]^2} \\ Y_{J,m_F} &= \frac{hc_{IJ}m_F}{2}-\frac{(g_J-g_I)\mu_N B}{2} \\ Z_{J,m_F} &= \frac{hc_{IJ}}{4}-g_J\mu_N B m_F \end{aligned} \tag{A.4}$$

in such a way that the Hamiltonian in Eq. (A.2) can be easily rewritten as:

$$\hat{H} = \begin{pmatrix} Z_{J,m_F}-Y_{J,m_F} & -\sqrt{X_{J,m_F}^2-Y_{J,m_F}^2} \\ -\sqrt{X_{J,m_F}^2-Y_{J,m_F}^2} & Z_{J,m_F}+Y_{J,m_F} \end{pmatrix}. \tag{A.5}$$

The diagonalization of this Hamiltonian provides the non-stretched eigenstates and the corresponding eigenvalues provided in Eqs. (2.23) and (2.24).
In the case of the extreme values of $|m_F| > J$, referred to as stretched states, only rotation-nuclear spin product states can exist because $\hat{J}_\pm |J, \pm J\rangle = 0$ and $\hat{I}_\pm |I, \pm I\rangle = 0$. Thus, the stretched states are never hybridized and, together with their corresponding eigenvectors, are given by Eqs. (2.26) and (2.27).

B

Adiabatic elimination

The three-level system in the Vee pattern, as shown in Figure 3.7, is described by the following Hamiltonian in the rotating wave approximation (RWA), in frequency units:

$$H_{\mathrm{RWA}} = \begin{pmatrix} 0 & \frac{\Omega_{\mathrm{ab}}}{2} & \frac{\Omega_{\mathrm{ac}}}{2} \\ \frac{\Omega_{\mathrm{ab}}}{2} & \Delta_{\mathrm{ab}} & 0 \\ \frac{\Omega_{\mathrm{ac}}}{2} & 0 & \Delta_{\mathrm{ac}} \end{pmatrix}. \tag{B.1}$$

The state vector for a general three-level system is the following [54, 55]:

$$\psi(t) = C_a(t)\psi'_a(t) + C_b(t)\psi'_b(t) + C_c(t)\psi'_c(t) \tag{B.2}$$

where,

$$\begin{cases} \psi'_a(t) = e^{-i\left(\frac{E_a}{\hbar}\right)t}\psi_a \\ \psi'_b(t) = e^{-i\left(\frac{E_a}{\hbar}+\omega_{ab}\right)t}\psi_b \\ \psi'_c(t) = e^{-i\left(\frac{E_a}{\hbar}+\omega_{ac}\right)t}\psi_c \end{cases} \tag{B.3}$$

with $\omega_{ab} = \frac{E_b - E_a}{\hbar}$ and $\omega_{ac} = \frac{E_c - E_a}{\hbar}$ the energy differences between the levels and E_a the reference energy. The detunings are defined with respect to the same Raman difference frequency: $\Delta_{\mathrm{ab}} = \omega_{ab} - \omega_{\mathrm{Raman}}$ and $\Delta_{\mathrm{ac}} = \omega_{ac} - \omega_{\mathrm{Raman}}$.
Rewriting the Schrödinger equation as a set of ordinary differential equations for the RWA amplitudes $C_n(t)$ yields the following matrix equation [56]:

$$\frac{d}{dt}\vec{C}(t) = -iH_{\mathrm{RWA}}\vec{C}(t) \tag{B.4}$$

and plugging in the Hamiltonian of Eq. (B.1) one gets:

$$\begin{cases} \frac{d}{dt}C_a = -i\frac{\Omega_{\text{ab}}}{2}C_b - i\frac{\Omega_{\text{ac}}}{2}C_c \\ \frac{d}{dt}C_b = -i\Delta_{\text{ab}}C_b - i\frac{\Omega_{\text{ab}}}{2}C_a \\ \frac{d}{dt}C_c = -i\frac{\Omega_{\text{ac}}}{2}C_a - i\Delta_{\text{ac}}C_c. \end{cases} \tag{B.5}$$

This set of differential equations allows us to simulate the population dynamics of a three-level system in a Vee pattern configuration, whose evolution depends on the Rabi frequency and the Raman detuning between the states.

C

Effective Raman Rabi rate

The effective Raman Rabi rate derivation presented in this Appendix closely follows Ref. [9]. We consider a three-level Vee system as shown in Figure 2.4. We consider the initial state $|a\rangle = |J, m_{Fa}, \xi_a\rangle$ and final state $|b\rangle = |J, m_{Fb}, \xi_b\rangle$ belonging to the same manifold, while the intermediate state $|e\rangle$ is the electronic first excited state: they respectively have energy eigenvalue E_a, E_b and E_e. We call the ground state frequency difference $\omega_0 = (E_b - E_a)/\hbar$, and the electronic exciting transition frequency difference $\omega_{ae} = (E_e - E_a)/\hbar$.
A Raman transition is implemented with two laser beams with π and σ^- polarizations, respectively, with $q_a = q_0^{(1)} = 0$ and $q_b = q_{-1}^{(2)} = -1$. These laser beams have frequency $\omega_1 = \omega_\pi$ and $\omega_2 = \omega_{\sigma^-}$ and electric field amplitude $|\vec{E_1}|$ and $|\vec{E_2}|$, and they are far off-resonant with respect to the electronic transition.
Supposing the Raman detuning $\Delta\omega = \omega_2 - \omega_1$ is close to the transition frequency ω_0, the effective Raman Rabi rate can be expressed using perturbation theory as [9]:

$$\Omega_{ab} = \frac{1}{4\hbar^2} \sum_e \frac{\langle b| e\vec{r} \cdot \vec{E}_2 |e\rangle \langle e| e\vec{r} \cdot \vec{E}_1 |a\rangle}{\omega_{ae} - \omega_1} + \frac{\langle b| e\vec{r} \cdot \vec{E}_1 |e\rangle \langle e| e\vec{r} \cdot \vec{E}_2 |a\rangle}{\omega_{ae} + \omega_2}, \tag{C.1}$$

where e is the charge of the electron and $\vec{r}$ its position. The equation sums the contributions from all possible intermediate excited states. The first term in the sum refers to the so-called counter-rotating stimulated Raman terms, rotating at $\omega_{ae} - \omega_1$: the photon is first absorbed with the first Raman field, and then stimulated with the second Raman field. Conversely, the second term in the sum refers to the so-called co-rotating terms, rotating at $\omega_{ae} + \omega_2$: the photon is first stimulated with the second Raman field, and then absorbed with the first one. This process is described in Chapter 2 and shown in Figure 2.4.
In this context, the laser fields are far-detuned, making the ratio $\frac{\omega_{ae}-\omega_1}{\omega_{ae}+\omega_2}$ around $1 : 2.22$ for $^{40}CaH^+$ and $1 : 1.70$ for $^{40}CaOH^+$. For this reason we cannot apply rotating wave

approximation to faster rotating terms: co-rotating contributions are not negligible and need to be considered.

Within the Born-Oppenheimer approximation, the molecular wavefunction factorizes into electronic, vibrational, and rotational components. With $s = \{a, b\}$, the dipole matrix element can then be separated into radial and angular parts using the Wigner-Eckart theorem:

$$\langle e|e\vec{r}\cdot\vec{E}|s\rangle = e|\vec{E}|\langle\psi_{e,v}|r|1^1\Sigma, v=0\rangle\langle\Phi_e(\theta,\phi)|\hat{r}\cdot\hat{\vec{q}}|\Phi_s(\theta,\phi)\rangle \tag{C.2}$$

where $\vec{r} = \hat{r}r$. The radial part of the wavefunction depends on the v quantum number and the internuclear distance, while the angular part on the two angle coordinates θ and ϕ.

The initial and final states lie in the ground electronic $|1^1\Sigma\rangle$ and ground vibrational $v = 0$ states, while being in given a rotational manifold J. We then consider the transition only to the lowest excited electronic state $|2^1\Sigma\rangle$, neglecting in ω_{ab} all contributions due to vibrational and rotational states: $\omega_{ab} \simeq (E_{2^1\Sigma} - E_{1^1\Sigma})/\hbar = \bar{\omega}$. Thus, we can express the effective Rabi rate as [9]:

$$\Omega_{ab} = \mathscr{E}(S_- + S_+), \quad \text{with} \quad \begin{cases} \mathscr{E} = \dfrac{e^2|\vec{E}_1||\vec{E}_2|}{4\hbar^2(\bar{\omega}-\omega_1)}\displaystyle\sum_{v'}\left|\langle\Psi_{2^1\Sigma,v'}|r|\Psi_{1^1\Sigma,v=0}\rangle\right|^2 \\ S_- = \displaystyle\sum_f \langle\Phi_b|\hat{r}\cdot\hat{\vec{q}}^{(2)}|\Phi_e\rangle\langle\Phi_e|\hat{r}\cdot\hat{\vec{q}}^{(1)}|\Phi_a\rangle \\ S_+ = \dfrac{\bar{\omega}-\omega_1}{\bar{\omega}+\omega_1}\displaystyle\sum_f \langle\Phi_b|\hat{r}\cdot\hat{\vec{q}}^{(1)}|\Phi_e\rangle\langle\Phi_e|\hat{r}\cdot\hat{\vec{q}}^{(2)}|\Phi_a\rangle \end{cases} \tag{C.3}$$

where S_- is related to the counter-rotating terms, S_+ to the co-rotating terms, and $\mathscr{E}$ is a prefactor equal for all the considered transitions.

The position operator only affects the rotational angular momentum eigenstates $|J, m_J\rangle$, without impacting the nuclear spin eigenstates $|I, m_I\rangle$: Thus we can write S_- as

$$S_- = \sum_{J,m_J,m_I} \langle\Phi_b|\hat{r}\cdot\hat{\vec{q}}^{(2)}|J,m_J\rangle|I,m_I\rangle\langle J,m_J|\langle I,m_I|\hat{r}\cdot\hat{\vec{q}}^{(1)}|\Phi_a\rangle, \tag{C.4}$$

and since $m_F = m_I + m_J$ is preserved as a good quantum number, the eigenstates become:

$$|\Phi_s\rangle = \sum_{m_I} c_{m_I}^{(s)}|J_s, m_{Fs} - m_I, 1/2, m_I\rangle, \tag{C.5}$$

where $c_{m_I}^{(s)}$ are the coefficients computed in Eq. 2.24. Then, we can re-write the matrix element for photon absorption by expressing $\hat{r}$ in the spherical basis and using the Wigner-Eckart theorem:

$$\langle J, m_J|\hat{r}\cdot\hat{\vec{q}}|J', m'\rangle = \sqrt{\max(J, J')}(J - J')\sum_{k=-1}^{1}\hat{q}_k(-1)^{J+k-m}\begin{pmatrix} J & 1 & J' \\ -m & k & m' \end{pmatrix}, \tag{C.6}$$

where the 2×3 array is the Wigner $3J$ symbol, which determines the dipole selection rules, filtering over the possible excited states to couple. In this way, S_- becomes [9]:

$$\begin{aligned} S_- = \sum_{m_I=-1/2}^{1/2}\sum_{k_1,k_2=-1}^{1} c_{m_I}^{(b)}c_{m_I}^{(a)}\Big[&\langle J_a - 1, m_{J_a} + k_1|\hat{r}_{k_2}\hat{q}_{k_2}^{(2)}|J_b, m_{J_a} + k_1 - k_2\rangle \\ &\times\langle J_a - 1, m_{J_a} + k_1|\hat{r}_{k_1}\hat{q}_{k_1}^{(1)}|J_a, m_{J_a}\rangle \\ &+\langle J_a + 1, m_{J_a} + k_1|\hat{r}_{k_2}\hat{q}_{k_2}^{(2)}|J_b, m_{J_a} + k_1 - k_2\rangle \\ &\times\langle J_a + 1, m_{J_a} + k_1|\hat{r}_{k_1}\hat{q}_{k_1}^{(1)}|J_a, m_{J_a}\rangle\Big] \end{aligned} \tag{C.7}$$

The S_+ co-rotating term is analogously computed.
For both S_- and S_+ terms, all possible combinations of spin-up ($c^{\uparrow}_{J,m_F,\pm}$) and spin-down ($c^{\downarrow}_{J,m_F,\pm}$) components between the initial and final states must be taken into account. However, transitions involving a change of the nuclear spin projection m_I (i.e. mixed combinations such as initial $m_I = +1/2$ and final $m_I = -1/2$, or vice versa) are excluded, since m_I is conserved.

D

Bayesian state estimation algorithm

Function 1: `molecule_state_prep`

Input: $B, T, J_{\max}, \eta$

`molecule` = `create_molecule_data`$(B, T, J_{\max})$;

P_J = `J_dist`$(B, T, J_{\max})$ $\quad$ $P_{\text{s.p.}}(s|J)$ = `pumping_RAP`$(P_J, B, T, J_{\max}, \eta)$;

$P_{\text{s.p.}}(s) = \{P_{\text{s.p.}}(s|J) | J = 1, ..., J_{\max}\}$;

return $P_J, P_{\text{s.p.}}(s|J), P_{\text{s.p.}}(s)$, `molecule`

Function 2: `BE_initialization`

Input: $P_{\text{s.p.}}(s)$, `molecule`

`model` = `molecule` $\quad$ $P_{\text{BE}}^{(0)}(s) = P_{\text{s.p.}}(s)$;

return $P_{\text{BE}}^{(0)}(s)$, `model`

Function 3: `BS_initialization`

Input: P_J, $P_{\text{s.p.}}(s|J)$

$J^{(0)} \sim P_J$ $\quad$ $|J, m, \xi\rangle_{\text{BS}}^{(0)} = s_{\text{BS}}^{(0)} \sim P_{\text{s.p.}}(s|J^{(0)})$;

return $|J, m, \xi\rangle_{\text{BS}}^{(0)}$

Function 4: `measurement_setting`

Input: ϵ, $J_{\max}$, `model`, ξ

$c_J^{\mathrm{ST}}, \omega_{\mathrm{mol}} =$ `model.transition_df` $\qquad \mathscr{P} = \{\mu = (\omega_{\mathrm{mol}}, t, \Omega_{\mathrm{Raman}})\}$. ;

if `marginalization` **then**

  for $\mu = (\omega_{mol}, t, \Omega_{Raman}) \in \mathscr{P}$ **do**

    $\omega_{\mathrm{Raman}} = \omega_{\mathrm{mol}} \qquad P(\omega_{\mathrm{Raman}}) = \mathcal{N}(\omega_{\mathrm{Raman}}, \sigma^{\mathrm{tot}}_{\omega_{\mathrm{Raman}}})$

    $\mathscr{L}_0^{\mu} = P(m_k = 0|s, \xi) = \sum_{\omega_{\mathrm{Raman}}} \mathscr{L}_0(\omega_{\mathrm{Raman}}) P(\omega_{\mathrm{Raman}})$

    $\mathscr{L}_1^{\mu} = P(m_k = 1|s, \xi) = \sum_{\omega_{\mathrm{Raman}}} \mathscr{L}_1(\omega_{\mathrm{Raman}}) P(\omega_{\mathrm{Raman}})$

  end

else

  for $\mu = (\omega_{mol}, t, \Omega_{Raman}) \in \mathscr{P}$ **do**

    $\omega_{\mathrm{Raman}} = \omega_{\mathrm{mol}}$

    $\mathscr{L}_0^{\mu} = P(m_k = 0|s, \xi) = \mathscr{L}_0(\omega_{\mathrm{Raman}})$

    $\mathscr{L}_0^{\mu} = P(m_k = 0|s, \xi) = \mathscr{L}_0(\omega_{\mathrm{Raman}})$

  end

end

return $\mathscr{P}, \{\mathscr{L}_0^{\mu}\}, \{\mathscr{L}_1^{\mu}\}$

Function 5: `update_distribution`

Input: $P_{\mathrm{BE}}^{(0)}(s)$, $|J, m, \xi\rangle_{\mathrm{BS}}^{(0)}$, ϵ, ξ, $\mathscr{P}$, $\{\mathscr{L}_0{}^{\mu}\}$, $\{\mathscr{L}_1{}^{\mu}\}$, `num_updates`, `block_type`, `block_size`

$\omega_{\mathrm{Raman}}^{\mathrm{mis}} \sim \mathcal{N}(\omega_{\mathrm{Raman}}, \sigma_{\omega_{\mathrm{Raman}}}^{\mathrm{mis}})$ $\quad$ $\Omega_{\mathrm{Raman}}^{\mathrm{mis}} \sim \mathcal{N}(\Omega_{\mathrm{Raman}}, \sigma_{\Omega_{\mathrm{Raman}}}^{\mathrm{mis}})$

for `j in range(num_updates)` **do**

  if `apply_pumping` **then**

    $P_{\mathrm{BE}}^{(t)}(s, \xi) = P_{\mathrm{s.p.}}(s)$ $\quad$ $s_{\mathrm{BS}}^{(t)} \sim P_{\mathrm{s.p.}}(s)$

  end

  for `i in range(block_size)` **do**

    `idx = get_next_setting(j, i, block_type, ξ)`

    $\mu = \mu_{\mathrm{idx}}$, $\quad$ $\mathscr{L}_0^{\mu} = \mathscr{L}_{0\,\mathrm{idx}}^{\mu}$, $\quad$ $\mathscr{L}_1^{\mu} = \mathscr{L}_{1\mathrm{idx}}^{\mu}$

    $\omega_{\mathrm{Raman}}^{\mathrm{shot}} \sim \mathcal{N}(\omega_{\mathrm{Raman}}^{\mathrm{mis}}, \sigma_{\omega_{\mathrm{Raman}}}^{\mathrm{shot}})$ $\quad$ $\Omega_{\mathrm{Raman}}^{\mathrm{shot}} \sim \mathcal{N}(\Omega_{\mathrm{Raman}}^{\mathrm{mis}}, \sigma_{\Omega_{\mathrm{Raman}}}^{\mathrm{shot}})$

    $\mu^{\mathrm{shot}} = (\omega_{\mathrm{Raman}}^{\mathrm{shot}}, t, \Omega_{\mathrm{Raman}}^{\mathrm{shot}})$ $\quad$ $k = \mathtt{index}(s_{\mathrm{BS}}^{(t)})$

    $\pi(s) = T_{*,k} = \mathtt{transition\_matrix}(\mu^{\mathrm{shot}})_{*,k}$

    $s_{\mathrm{BS}}^{(t+1)} = |J, m, \xi\rangle_{\mathrm{BS}}^{(t+1)} \sim \pi(s)$

    if $s_{BS}^{(t+1)} = s_{BS}^{(t)}$ **then**

      `outcome = 0`

      if $p \sim \mathcal{N}(0,1) < f_{pr}$ **then**

        `outcome = 1`

      end

      $\mathscr{L} = f_{\mathrm{nr}}\mathscr{L}_0^{\mu} + (1 - f_{\mathrm{pr}})\mathscr{L}_1^{\mu}$

    else

      if $p \sim \mathcal{N}(0,1) < f_{nr}$ **then**

        `outcome = 0`

      end

      $\mathscr{L} = f_{\mathrm{nr}}\mathscr{L}_0^{\mu} + (1 - f_{\mathrm{pr}})\mathscr{L}_1^{\mu}$

    end

    $q^{\mathrm{BE}(t+1)} = P_{\mathrm{BE}}^{(t+1)}(s|m_k^{(t+1)}, \xi) = \frac{\mathscr{L}P_{\mathrm{BE}}^{(t)}(s|m_k^{(t)}, \xi)}{\sum_s \mathscr{L}P_{\mathrm{BE}}^{(t)}(s|m_k^{(t)}, \xi)}$

    $p^{\mathrm{BS}(t+1)} = P(s^{(t+1)}) = \delta_{s^{(t)}, s_{\mathrm{BS}}^{(t+1)}}$

    `cross_entropy` $= H(q^{\mathrm{BE}(t+1)}, p^{\mathrm{BS}(t+1)})$ $\qquad$ `variance` $= \mathrm{Var}_{q^{\mathrm{BE}(t+1)}}[s]$

    if $\exists s / q^{BE(t+1)}(s) > 0.9$ **then**

      `stop_flag = True`

      break

    end

  end

  if `stop_flag` **then**

    break

  end

end

Function 6: `Bayesian_state_estimation`

Input: $N, \epsilon, \xi, B, T, J_{\max}, \eta$, `num_updates`, `block_type`, `block_size`

$P_J, P_{\text{s.p.}}(s|J), P_{\text{s.p.}}(s)$, `molecule` = `molecule_state_preparation`$(B, T, J_{\max}, \eta)$

$P_{\text{BE}}^{(0)}(s)$, `model` = `BE_initialization`$(P_{\text{s.p.}}(s)$, `molecule`$)$

$\mathscr{P}, \{\mathscr{L}_0{}^{\mu}\}, \{\mathscr{L}_1{}^{\mu}\}$ = `measurement_setting`$(\epsilon, J_{\max}$, `model`$, \xi)$

for `run in N` **do**

  $|J, m, \xi\rangle_{\text{BS}}^{(0)}$ = `BS_initialization`$(P_J, P_{\text{s.p.}}(s|J))$

  `update_distribution`$(P_{\text{BE}}^{(0)}(s), |J, m, \xi\rangle_{\text{BS}}^{(0)}, \epsilon, \xi,$
  $\mathscr{P}, \{\mathscr{L}_0{}^{\mu}\}, \{\mathscr{L}_1{}^{\mu}\}$, `num_updates`, `block_type`, `block_size`$)$

  $t = 0, \quad P_{\text{BE}}^{(0)}(s) = P_{\text{s.p.}}(s)$

end

E

Code availability

The simulations presented in this thesis have been implemented in Python and organized in a publicly available release on GitHub [57] , which provides a stable and citable snapshot of the code. The repository includes all source code, example notebooks, and scripts used to perform the analyses described in this work.

Bibliography

[1] C. Cohen-Tannoudji, G. Grynberg, and J. Dupont-Roc, *Atom-Photon Interactions: Basic Processes and Applications*. New York: Wiley, 1992.

[2] M. O. Scully and M. S. Zubairy, *Quantum optics*. Cambridge: Cambridge University Press, 1997. [Online]. Available: http://ebooks.cambridge.org/ref/id/CBO9780511813993

[3] M. A. Nielsen and I. L. Chuang, *Quantum Computation and Quantum Information*. Cambridge University Press, 2000.

[4] H. Moya-Cessa, F. Soto-Eguibar, J. M. Vargas-Martínez, R. Juárez-Amaro, and A. Zúñiga-Segundo, "Ion–laser interactions: The most complete solution," *Physics Reports*, vol. 513, no. 5, pp. 229–261, 2012, ion-laser interactions: the most complete solution. [Online]. Available: https://www.sciencedirect.com/science/article/pii/S0370157312000117

[5] R. J. Glauber, "Coherent and incoherent states of the radiation field," *Phys. Rev.*, vol. 131, pp. 2766–2788, Sep 1963. [Online]. Available: https://link.aps.org/doi/10.1103/PhysRev.131.2766

[6] C. Hempel and U. of Innsbruck (Austria), "Digital quantum simulation, schrödinger cat state spectroscopy and setting up a linear ion trap," 2014.

[7] G. Morigi, J. Eschner, and C. H. Keitel, "Ground state laser cooling using electromagnetically induced transparency," *Phys. Rev. Lett.*, vol. 85, pp. 4458–4461, Nov 2000. [Online]. Available: https://link.aps.org/doi/10.1103/PhysRevLett.85.4458

[8] J. I. Cirac, R. Blatt, P. Zoller, and W. D. Phillips, "Laser cooling of trapped ions in a standing wave," *Phys. Rev. A*, vol. 46, pp. 2668–2681, Sep 1992. [Online]. Available: https://link.aps.org/doi/10.1103/PhysRevA.46.2668

[9] C.-w. Chou, C. Kurz, D. B. Hume, P. N. Plessow, D. R. Leibrandt, and D. Leibfried, "Preparation and coherent manipulation of pure quantum states of a single molecular ion," *Nature*, vol. 545, no. 7653, p. 203–207, May 2017. [Online]. Available: http://dx.doi.org/10.1038/nature22338

[10] B. Furey, "Nuclear spin one-half electronic one-sigma linear molecular ions," 2025.

[11] B. J. Furey, Z. Wu, M. Isaza-Monsalve, S. Walser, E. Mattivi, R. Nardi, and P. Schindler, "Strategies for implementing quantum error correction in molecular rotation," *Quantum*, vol. 8, p. 1578, Dec. 2024. [Online]. Available: http://dx.doi.org/10.22331/q-2024-12-27-1578

[12] D. DeMille, "Quantum computation with trapped polar molecules," *Phys. Rev. Lett.*, vol. 88, p. 067901, Jan 2002. [Online]. Available: https://link.aps.org/doi/10.1103/PhysRevLett.88.067901

[13] K. Mølmer, Y. Castin, and J. Dalibard, "Monte carlo wave-function method in quantum optics," *J. Opt. Soc. Am. B*, vol. 10, no. 3, pp. 524–538, Mar 1993. [Online]. Available: https://opg.optica.org/josab/abstract.cfm?URI=josab-10-3-524

[14] P. Rabl, D. DeMille, J. M. Doyle, M. D. Lukin, R. J. Schoelkopf, and P. Zoller, "Hybrid quantum processors: Molecular ensembles as quantum memory for solid state circuits," *Phys. Rev. Lett.*, vol. 97, p. 033003, Jul 2006. [Online]. Available: https://link.aps.org/doi/10.1103/PhysRevLett.97.033003

[15] D. Leibfried, B. DeMarco, V. Meyer, D. Lucas, M. Barrett, J. Britton, W. Itano, B. Jelenkovic, C. Langer, T. Rosenband, and D. Wineland, "Experimental demonstration of a robust, high-fidelity geometric two ion-qubit phase gate," *Nature*, vol. 422, pp. 412–5, 04 2003.

[16] D. Leibfried, R. Blatt, C. Monroe, and D. Wineland, "Quantum dynamics of single trapped ions," *Rev. Mod. Phys.*, vol. 75, pp. 281–324, 2003.

[17] D. J. Wineland, C. Monroe, W. M. Itano, D. Leibfried, B. E. King, and D. M. Meekhof, "Experimental issues in coherent quantum-state manipulation of trapped atomic ions," 1998. [Online]. Available: https://arxiv.org/abs/quant-ph/9710025

[18] D. Leibfried, R. Blatt, C. Monroe, and D. Wineland, "Quantum dynamics of single trapped ions," *Rev. Mod. Phys.*, vol. 75, pp. 281–324, Mar 2003. [Online]. Available: https://link.aps.org/doi/10.1103/RevModPhys.75.281

[19] C. Roos, T. Zeiger, H. Rohde, H. C. Nägerl, J. Eschner, D. Leibfried, F. Schmidt-Kaler, and R. Blatt, "Quantum state engineering on an optical transition and decoherence in a paul trap," *Phys. Rev. Lett.*, vol. 83, pp. 4713–4716, Dec 1999. [Online]. Available: https://link.aps.org/doi/10.1103/PhysRevLett.83.4713

[20] C. W. Chou, A. L. Collopy, C. Kurz, Y. Lin, M. E. Harding, P. N. Plessow, T. Fortier, S. Diddams, D. Leibfried, and D. R. Leibrandt, "Frequency-comb spectroscopy on pure quantum states of a single molecular ion," *Science*, vol. 367, no. 6485, pp. 1458–1461, 2020.

[21] D. B. Hume, C. W. Chou, D. R. Leibrandt, M. J. Thorpe, D. J. Wineland, and T. Rosenband, "Trapped-ion state detection through coherent motion," *Phys. Rev. Lett.*, vol. 107, p. 243902, Dec 2011. [Online]. Available: https://link.aps.org/doi/10.1103/PhysRevLett.107.243902

[22] M. Affolter, K. A. Gilmore, J. E. Jordan, and J. J. Bollinger, "Phase-coherent sensing of the center-of-mass motion of trapped-ion crystals," *Physical Review A*, vol. 102, no. 5, Nov. 2020. [Online]. Available: http://dx.doi.org/10.1103/PhysRevA.102.052609

[23] P. Staanum, M. Drewsen, and K. Mølmer, "Geometric quantum gate for trapped ions based on optical dipole forces induced by gaussian laser beams," *Physical Review A*, vol. 70, no. 5, Nov. 2004. [Online]. Available: http://dx.doi.org/10.1103/PhysRevA.70.052327

[24] S. Blanes, F. Casas, J. Oteo, and J. Ros, "The magnus expansion and some of its applications," *Physics Reports*, vol. 470, no. 5–6, p. 151–238, Jan. 2009. [Online]. Available: http://dx.doi.org/10.1016/j.physrep.2008.11.001

[25] J. J. García-Ripoll, P. Zoller, and J. I. Cirac, "Speed optimized two-qubit gates with laser coherent control techniques for ion trap quantum computing," *Phys. Rev. Lett.*, vol. 91, p. 157901, Oct 2003. [Online]. Available: https://link.aps.org/doi/10.1103/PhysRevLett.91.157901

[26] A. Sørensen and K. Mølmer, "Entanglement and quantum computation with ions in thermal motion," *Physical Review A*, vol. 62, no. 2, Jul. 2000. [Online]. Available: http://dx.doi.org/10.1103/PhysRevA.62.022311

[27] C. Monroe, D. M. Meekhof, B. E. King, S. R. Jefferts, W. M. Itano, D. J. Wineland, and P. Gould, "Resolved-sideband raman cooling of a bound atom to the 3d zero-point energy," *Phys. Rev. Lett.*, vol. 75, pp. 4011–4014, Nov 1995. [Online]. Available: https://link.aps.org/doi/10.1103/PhysRevLett.75.4011

[28] K. Bergmann, H. Theuer, and B. W. Shore, "Coherent population transfer among quantum states of atoms and molecules," *Reviews of Modern Physics*, vol. 70, pp. 1003–1025, 1998.

[29] N. V. Vitanov and B. M. Garraway, "Landau-zener model: Effects of finite coupling duration," *Phys. Rev. A*, vol. 53, pp. 4288–4304, Jun 1996. [Online]. Available: https://link.aps.org/doi/10.1103/PhysRevA.53.4288

[30] T. Watanabe, S. Nomura, K. Toyoda, and S. Urabe, "Sideband excitation of trapped ions by rapid adiabatic passage for manipulation of motional states," *Phys. Rev. A*, vol. 84, p. 033412, Sep 2011. [Online]. Available: https://link.aps.org/doi/10.1103/PhysRevA.84.033412

[31] E. Treacy, "Adiabatic inversion with light pulses," *Physics Letters A*, vol. 27, no. 7, pp. 421–422, 1968. [Online]. Available: https://www.sciencedirect.com/science/article/pii/0375960168908347

[32] K. Mølhave and M. Drewsen, "Formation of translationally cold mgh^+ and mgd^+ molecules in an ion trap," *Phys. Rev. A*, vol. 62, p. 011401, Jun 2000. [Online]. Available: https://link.aps.org/doi/10.1103/PhysRevA.62.011401

[33] R. Rugango, J. E. Goeders, T. H. Dixon, J. M. Gray, N. B. Khanyile, G. Shu, R. J. Clark, and K. R. Brown, "Sympathetic cooling of molecular ion motion to the ground state," *New Journal of Physics*, vol. 17, no. 3, p. 035009, mar 2015. [Online]. Available: https://dx.doi.org/10.1088/1367-2630/17/3/035009

[34] Y. Wan, F. Gebert, F. Wolf, and P. O. Schmidt, "Efficient sympathetic motional-ground-state cooling of a molecular ion," *Phys. Rev. A*, vol. 91, p. 043425, Apr 2015. [Online]. Available: https://link.aps.org/doi/10.1103/PhysRevA.91.043425

[35] R. Rugango, A. T. Calvin, S. Janardan, G. Shu, and K. R. Brown, "Vibronic spectroscopy of sympathetically cooled cah+," *ChemPhysChem*, vol. 17, no. 22, p. 3764–3768, Aug. 2016. [Online]. Available: http://dx.doi.org/10.1002/cphc.201600645

[36] M. Abe, Y. Moriwaki, M. Hada, and M. Kajita, "Ab initio study on potential energy curves of electronic ground and excited states of (cah+)-ca-40 molecule," *Chemical Physics Letters*, vol. 521, p. 31–35, 01 2012.

[37] R. A. VanGundy, J. H. Bartlett, and M. C. Heaven, "Spectroscopy of the low-lying states of cao+," *Journal of Molecular Spectroscopy*, vol. 344, pp. 17–20, 2018. [Online]. Available: https://www.sciencedirect.com/science/article/pii/S0022285217303776

[38] L. Qi, E. C. Reed, and K. R. Brown, "Adiabatically controlled motional states of a cao^+ and ca^+ trapped-ion chain cooled to the ground state," *Phys. Rev. A*, vol. 108, p. 013108, Jul 2023. [Online]. Available: https://link.aps.org/doi/10.1103/PhysRevA.108.013108

[39] Z. Wu, S. Walser, V. Podlesnic, M. Isaza-Monsalve, E. Mattivi, G. Mu, R. Nardi, P. Gniewek, M. Tomza, B. J. Furey, and P. Schindler, "Photodissociation spectra of single trapped caoh+ molecular ions," *The Journal of Chemical Physics*, vol. 161, no. 4, Jul. 2024. [Online]. Available: http://dx.doi.org/10.1063/5.0217685

[40] K. Okada, M. Wada, L. Boesten, T. Nakamura, I. Katayama, and S. Ohtani, "Acceleration of the chemical reaction of trapped ca+ ions with h2o molecules by laser excitation," *Journal of Physics B: Atomic, Molecular and Optical Physics*, vol. 36, no. 1, p. 33, dec 2002. [Online]. Available: https://dx.doi.org/10.1088/0953-4075/36/1/304

[41] F. Wolf, Y. Wan, J. C. Heip, F. Gebert, C. Shi, and P. O. Schmidt, "Non-destructive state detection for quantum logic spectroscopy of molecular ions," *Nature*, vol. 530, no. 7591, p. 457–460, Feb. 2016. [Online]. Available: http://dx.doi.org/10.1038/nature16513

[42] A. K. Hansen, M. A. Sørensen, P. F. Staanum, and M. Drewsen, "Single-ion recycling reactions," *Angewandte Chemie International Edition*, vol. 51, no. 32, pp. 7960–7962, 2012. [Online]. Available: https://onlinelibrary.wiley.com/doi/abs/10.1002/anie.201203550

[43] NIST Chemistry WebBook. (2025) Nist computational chemistry comparison and benchmark database (cccbdb) - dipole moments. Accessed: 2025-08-09. [Online]. Available: https://cccbdb.nist.gov/dipole2x.asp

[44] National Institute of Standards and Technology}. (2024) Codata recommended values of the fundamental physical constants. Accessed: 2025-08-09. [Online]. Available: https://physics.nist.gov/cgi-bin/cuu/Value?k

[45] National Institute of Standards and Technology. (2022) Codata value: Nuclear magneton. Accessed: 2025-08-09. [Online]. Available: https://physics.nist.gov/cgi-bin/cuu/Value?mun

[46] National Institute of Standards and Technology. (2024) Codata recommended values of the fundamental physical constants. Accessed: 2025-08-09. [Online]. Available: https://physics.nist.gov/cgi-bin/cuu/Value?gp

[47] M. Gronowski and M. Tomza, "Caoh+ nmr parameters," 2024, technical note, Faculty of Physics, University of Warsaw.

[48] N. Lambert, E. Giguère, P. Menczel, B. Li, P. Hopf, G. Suárez, M. Gali, J. Lishman, R. Gadhvi, R. Agarwal, A. Galicia, N. Shammah, P. Nation, J. R. Johansson, S. Ahmed, S. Cross, A. Pitchford, and F. Nori, "Qutip 5: The quantum toolbox in python," 2024. [Online]. Available: https://arxiv.org/abs/2412.04705

[49] P. M. Lee, *Bayesian statistics : an introduction / Peter M. Lee.*, 4th ed. Chichester, West Sussex ;: Wiley, 2012.

[50] L. Gerster, F. Martínez-García, P. Hrmo, M. W. van Mourik, B. Wilhelm, D. Vodola, M. Müller, R. Blatt, P. Schindler, and T. Monz, "Experimental bayesian calibration of trapped-ion entangling operations," *PRX Quantum*, vol. 3, p. 020350, Jun 2022. [Online]. Available: https://link.aps.org/doi/10.1103/PRXQuantum.3.020350

[51] T. Rainforth, A. Foster, D. R. Ivanova, and F. B. Smith, "Modern bayesian experimental design," 2023. [Online]. Available: https://arxiv.org/abs/2302.14545

[52] S. S. Qian, C. A. Stow, and M. E. Borsuk, "On monte carlo methods for bayesian inference," *Ecological Modelling*, vol. 159, no. 2, pp. 269–277, 2003. [Online]. Available: https://www.sciencedirect.com/science/article/pii/S0304380002002995

[53] D. J. Warne, T. P. Prescott, R. E. Baker, and M. J. Simpson, "Multifidelity multilevel monte carlo to accelerate approximate bayesian parameter inference for partially observed stochastic processes," *Journal of Computational Physics*, vol. 469, p. 111543, Nov. 2022. [Online]. Available: http://dx.doi.org/10.1016/j.jcp.2022.111543

[54] R. M. Whitley and C. R. Stroud, "Double optical resonance," *Phys. Rev. A*, vol. 14, pp. 1498–1513, Oct 1976. [Online]. Available: https://link.aps.org/doi/10.1103/PhysRevA.14.1498

[55] C. E. Carroll and F. T. Hioe, "Three-state model driven by two laser beams," *Phys. Rev. A*, vol. 36, pp. 724–729, Jul 1987. [Online]. Available: https://link.aps.org/doi/10.1103/PhysRevA.36.724

[56] B. W. Shore, "Coherent manipulations of atoms using laser light," *Acta Physica Slovaca*, vol. 58, no. 3, pp. 243–486, Jun. 2008.

[57] A. Turci, "Bayesian inference for molecular quantum logic spectroscopy." [Online]. Available: https://doi.org/10.5281/zenodo.18961430

Acknowledgments

Completing this work would not have been possible without the enormous help and the wonderful welcome of the people I had the fortune to meet and the pleasure to collaborate with: in particular Brandon Furey, Philipp Schindler, and the entire QCosmo group at the University of Innsbruck.
I am infinitely grateful to have shared my journey in Padova and Innsbruck, of which this thesis only closes the circle, with wonderful people, whom I deeply respect and who have contributed to enriching me. It is especially thanks to you that I am proud of the person I have become.
In particular, I would like to thank my whole family for the support and affection that I have always carried with me; my friends from Modena, including Dario, Vigno, Pit, Leo, Fede, Pisto, and Lucio (the most intelligent group), for the laughter and the memories of our never-ending friendship; my friends in Padova and Innsbruck for making me feel at home wherever I was. Finally Migo, for the incredible moments of sharing, joy, and lightheartedness we spent together.

Terminare questo lavoro non sarebbe stato possibile senza l'enorme aiuto e la fantastica accoglienza delle persone che ho avuto la fortuna di conoscere e il piacere di collaborare: in particolare Brandon Furey e Philipp Schindler e tutto il gruppo QCosmo dell'Universita di Innsbruck.
Sono infinitamente grato di aver condiviso il mio percorso a Padova e a Innsbruck, di cui questa tesi ne chiude solo il cerchio, con persone stupende, che stimo molto e che hanno contribuito ad arricchirmi. E' specialmente grazie a voi se sono fiero della persona che sono diventato.
In particolare ci tengo a ringraziare tutta la mia famiglia per il supporto e l'affetto che ho portato sempre dentro di me; gli amici di Modena, tra cui, Dario, Vigno, Pit, Leo, Fede, Pisto, Lucio e Corra (il gruppo piu intelligente) per le risoate e i ricordi della nostra interminabile amicizia; gli amici di Padova e di Innsbruck per avermi fatto sentire a casa ovunque mi trovassi. Infine Migo, per gli incredibili momenti di condivisione, gioia e spensieratezza passati assieme.